universität wien

MASTERARBEIT

Titel der Masterarbeit

"Synthesis of Supported Intermetallic ZnPd/Al_2O_3 Catalysts"

verfasst von

Patrick Wibner, BSc.

angestrebter akademischer Grad

Master of Science (MSc.)

Wien, 2014

Studienkennzahl lt. Studienblatt:	A 066 862
Studienrichtung lt. Studienblatt:	Masterstudium Chemie
Betreut von:	ao. Univ.-Prof. Mag. Dr. Klaus Richter

No one should approach the temple of science with the soul of a money changer.

-Thomas Browne

If you're not part of the solution, you're part of the precipitate.

-Henry J. Tillman

Preface

This work was conducted from March 2014 to September 2014 in the working group of Ao. Univ. -Prof. Mag. Dr. Klaus Richter at the department of Inorganic Chemistry (Materials Chemistry).

I want to thank Prof. Richter for giving me the opportunity to do my master thesis on such an interesting and important topic since it combines material chemistry and the topic renewable energy production, which is a very important issue in today's society. Working on a topic with such relevance and promising future was very interesting and I couldn´t have made such a fast progress without the guidance and counselling of Prof. Richter.

Especially, I want to thank Dr. Marc Armbrüster and M.Sc. René Kriegel at the Max-Planck-Institute for Chemical Physics of Solids in Dresden for their cooperation and concession during my stay at the MPI where I performed the catalytic measurements. The cooperation showed me that the phrase "That is not possible" is simply not existence in their vocabulary.

Also I want to thank Prof. Mag. Dr. Thomas Waitz for conducting the TEM measurements and helping me to interpret the resulting TEM patterns.

Furthermore, I want to thank all my colleagues in the whole department for their everlasting support, especially Alexander Beutl MSc. and Matthias Stacher MSc., who never turned me down whenever I needed a helping hand.

Moreover, I am deeply grateful to Sarah Theiner and Matthias Klose for conducting the ICP-MS measurements.

Table of Contents

1. Introduction

Why is catalysis so important in today's society?

The energy demand of all countries, especially developing countries, continues to rise while the available resources are shrinking. About 80% of the current energy demand are covered by oil, gas or coal power plants. Extrapolation of the current trend of growth in global energy demand shows an almost linear increase (Figure 1).

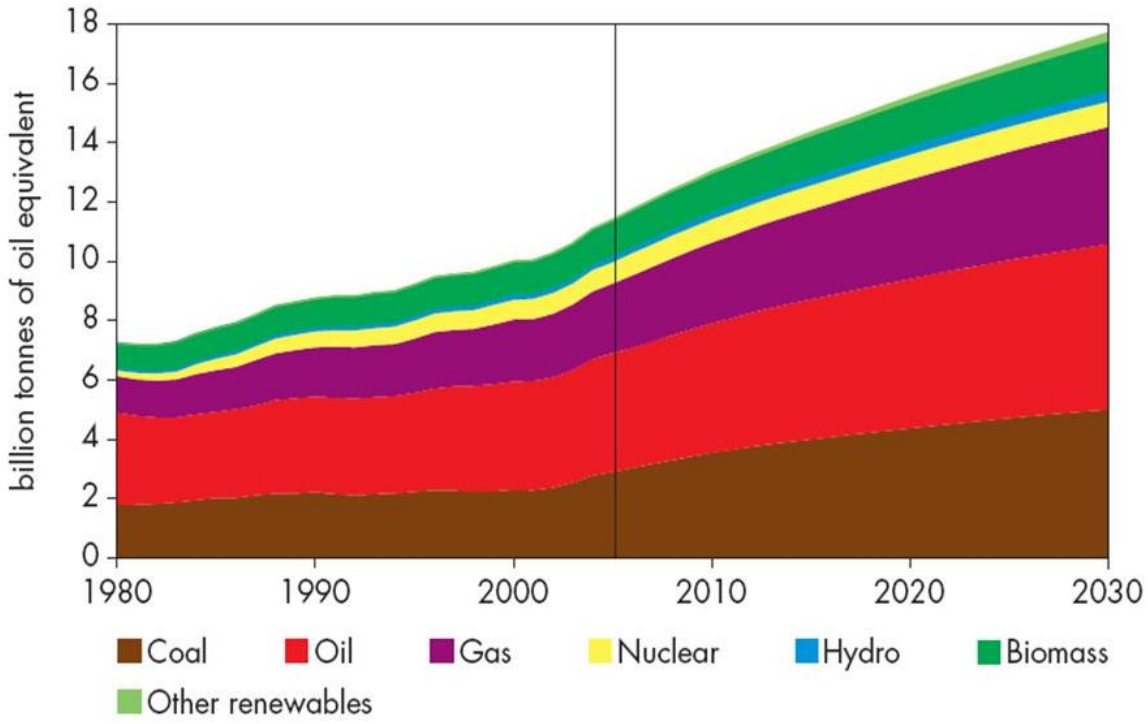

Figure 1 Projected growth in Global-Energy-Demand [1]

It might be possible to produce the energy required in 2030 by fossil fuels but it is not clear if energy cooperations would be able to supply oil, gas or coal in such large volumes. The increase in fossil fuels will also lead to an increase in emission of CO_2 which is a key contributor to global warming. Primary Energy sources can be divided in two main categories, renewable and nonrenewable sources. Nonrenewable energy sources can either be oil, natural gas, coal or nuclear fuels. Renewable energy sources can usually be summarized in solar and geothermal energy. Solar energy is the major category and includes energy from wind, photovoltaics, hydro power and biomass power plants. When talking about energy consumption the end-use of each energy source has to be considered. For example, about 90% of coal is used for energy production while most of the oil is used for transportation. If cars would be powered by electrical energy instead of oil, the demand for oil would be reduced while the demand for coal would rise. It becomes clear that reducing

the demand for oil alone is not sufficient. Finding new sources for energy production, which are independent of daytime or climate, would be most desirable. Only 17% of our total energy use is covered by non-fossil fuels [2]. The total energy that can be produced by the primary sources is distributed to five main fields shown in Figure 2. The rejected energy shown in Figure 2 stands for wasted energy that is lost due to low temperature streams. More than half of the available total energy is lost in form of wasted energy. For a green future it is therefore not only necessary to increase the amount of renewable energy but also to reduce the amount of wasted energy [3]

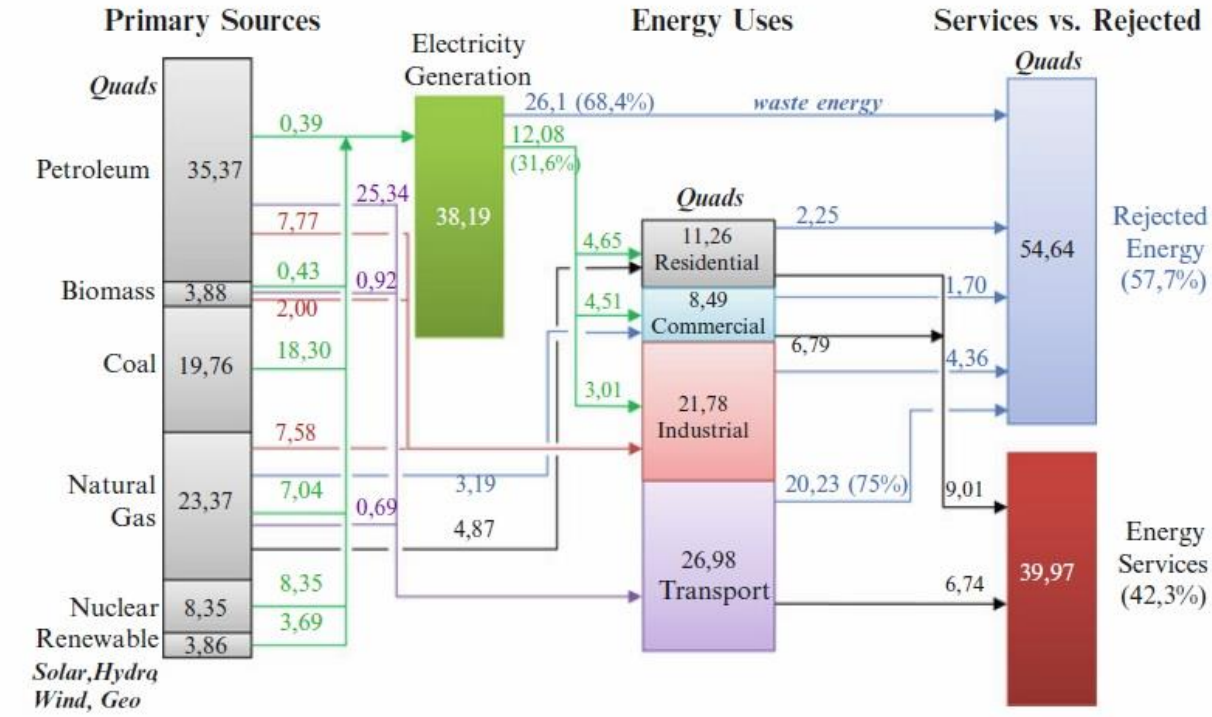

*Figure 2 Main energy fluxes (quads in 1.055*10[18]J) [3]*

Recently a lot of research has been conducted on energy saving in energy consuming industries. The results of this research showed that a large amount of wasted energy can be saved using innovative recovery cycles to recover wasted heat by installing heat exchangers or changing existing processing routes. Improving processing efficiency and conservation of energy by new technologies is a prime objective for many researchers. A problem for research and development of new technologies is the funding and the available time. Many research projects are limited to a few years and should provide results after a set time. Researchers would need more time to provide improved results [2]. Changing a processing route usually requires the use of new catalysts to improve the efficiency of a process. Developing new catalysts and controlling their nanostructure are the basis for developing

new materials for energy applications. Catalysts could be used in cars to reduce the oil consumption of a car, in lithium-ion-batteries to improve the life-time and capacity or in material development to produce new materials for different applications. The main fields of application of new material catalysts are energy conversion, storage, transport and efficiency [3].

Moving from fossil fuels to renewable energy requires new energy carriers. The characteristics of a good energy carrier are high energy density by volume and weight, easy storage at room temperature without the requirement of high pressure, low toxicity, safe in handling, environmentally friendly combustions products and good applicability in already existing energy infrastructure [3]. Hydrogen, ethanol, methanol and biodiesel are said to be the most favorable energy suppliers for the future. The disadvantage of this "new" type of fuels is the difference in energy per volume between those new fuels and oil. Hydrogen has the lowest energy per volume but it still received much attention because it can be "burned" CO_2 free. It is usually "burned" in fuel cells where it generates electricity via a controlled Knallgas reaction with oxygen. The efficiency of a fuel cell is about 40-60% while a combustion engine has an efficiency of 25%. Another advantage of a fuel cell is that the only reaction product is water. Despite its low energy density, hydrogen fuel cells face another disadvantage. Hydrogen is a gas and therefore its volumetric energy density can be either increased by pressuring it to higher pressures, or by producing hydrogen in-situ in the fuel cell. Transporting and storing a pressurized gas can be very challenging, because vessels that can stand a high pressure are usually constructed from heavy steal which makes it impossible for the application in cars. The next question would be the durability of such vessels and the stability of the connections and vents. Since hydrogen is the smallest existing gas molecule, it leaks about 2.8 times faster than other gases. Even small holes or cracks can lead to a quick spilling of the gas, which is very dangerous in closed spaces since hydrogen is flammable. Because of these drawbacks in storing of pure hydrogen other ways of hydrogen storage have been extensively researched. Hydrogen can be stored in a chemical form as a metal hydride, for example $NaBH_4$. The release of hydrogen can be triggered by applying an elevated temperature to the metal hydride or by mixing them with water. Newly developed materials are able to uptake hydrogen by cooling the material while exposing it to a hydrogen gas flow. These materials are often complicated zeolite structures or carbon nanotubes. The energy to weight ratio of these materials is still very poor and they can store

around 7% of hydrogen by weight. Because of this limitation metal hydrides can only be used in stationary applications [2].

An alternative is storing hydrogen in chemical form as methanol. The major advantage of methanol as a storage medium is than it can be synthesized from CO_2 by hydrogenation. Methanol can store two hydrogen molecules per methanol molecule, yielding a ratio of 1:2 and no C-C bonds need to be broken during the release of hydrogen. The side product of the release of hydrogen from methanol is CO_2. Combining a catalyzed release and storage of hydrogen would allow for a CO_2-neutral energy generation.

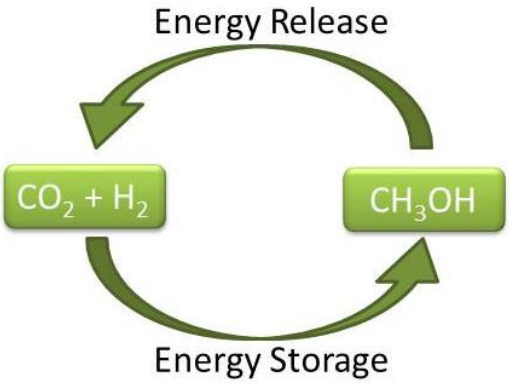

Figure 3 CO_2-neutral energy balance

Under standard conditions methanol is a liquid, which is a major advantage compared to the physical storage of hydrogen. An on-board catalyst, which catalysis the reaction of methanol to hydrogen, would allow methanol to be used as a fuel for fuel-cell cars. This type of fuel cell is called *Direct-methanol-fuel-cell* (DMFC). The release of hydrogen from methanol is named "Methanol-Steam-Reforming" (MSR). For this purpose the catalysts $Cu/ZnO/Al_2O_3$ and derivatives have been investigated. Because of the poor CO_2 selectivity of these copper based catalysts, a new model catalyst was needed. Promising nobel metal catalysts are Pd/ZnO and the intermetallic phase PdZn. Carbon monoxide is an undesirable side product of the MSR process. Possible side reactions of the MSR reaction are summarized in Figure 4. In addition to the two catalysts for hydrogen storage and release a third catalyst is needed for hydrogen production. A renewable and environmentally friendly

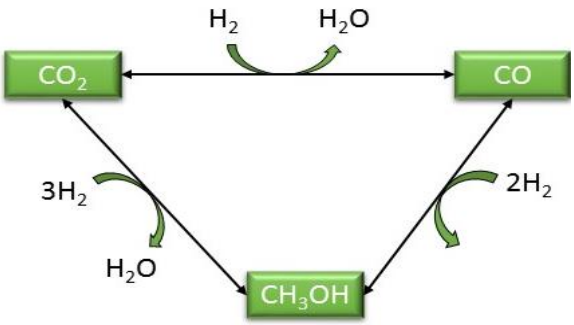

Figure 4 Carbon dioxide hydrogenation to methanol and side reactions

energy production needs a way to produce hydrogen, in large quantities without relying on fossil fuels as an energy source for its production. In 1972, Fujishima [4] investigated the electrochemical photolysis of water at a semiconductor electrode. Fujishima found that TiO_2 showed promising results for hydrogen production. In the following years, many photo catalysts like TiO_2, CdS and SiC were investigated. Many researchers focused on modifying these catalysts by noble metal loading, dye sensitization and doping to improve their catalytic activity. The large amount of available literature on this topic shows how important and promising the developing of a functioning photo catalyst can be. [5] A summed up reaction scheme of the whole energy storage and generation process is given in Figure 5.

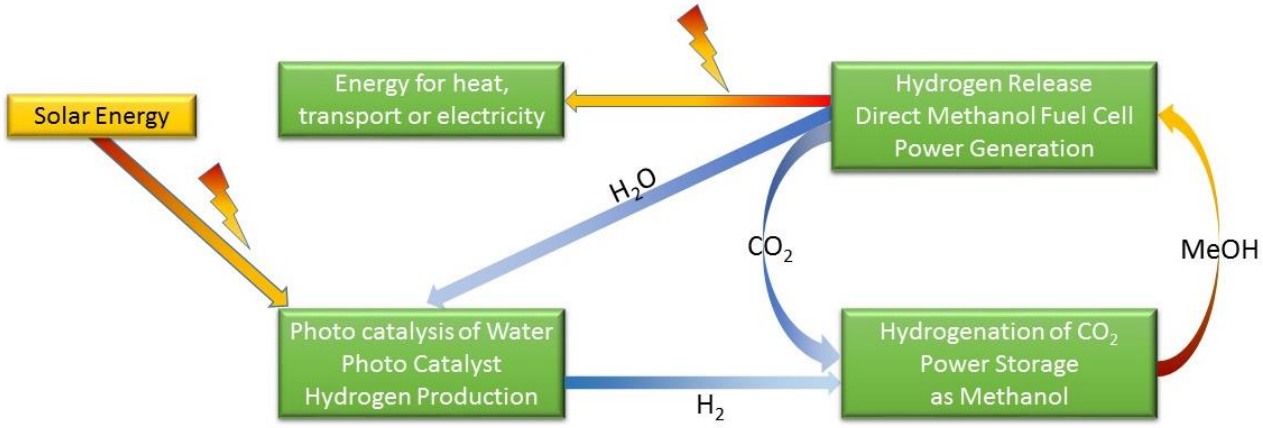

Figure 5 Basis concept of a CO_2-neutral renewable energy generation using methanol as an energy storage

This concept relies completely on the sun as an energy source and the storage of this energy in a closed cycle with no side products other than energy.

2. Literature Review

2.1. The binary System Palladium-Zinc

During investigating the magnetic properties of different intermetallic systems in 1950 Nowotny and Bittner [6] found the intermetallic compound PdZn (1:1 phase). In samples annealed at 650°C. The phase PdZn showed a maximum concentration of 52 atomic percent zinc at 650°C. The structure was reported to be a tetragonal CuAu-type comparable to the NiZn phase.

Nowotny et al [7] published the first description of the palladium-zinc phase diagram in 1951. The composition was verified by susceptibility measurements. No samples were annealed above 900°C, so the phase boundaries drawn above this temperature are estimated (Fig 6). For sample preparation, Nowotny et al used a custom build pressure furnace. A large solubility of zinc in alpha-palladium was observed. The phases β and β_1 were reported as body-centred cubic with an almost identical lattice parameter. This fact lead to the assumption, that β and β_1 undergo a phase transition at higher temperatures in such a way, that the cooling of this higher temperature phase will lead to the formation of the δ-phase (PdZn). For β and β_1, room temperature phases (ξ and ξ_1 in the phase diagram) of lower symmetry than their corresponding high temperature phases were found. Since Nowotny et al couldn`t obtain a homogeneous sample of either room temperature phase, their crystal structure remained unclear. The phase's γ and γ_1 were found to be related Hume-Rothery-phases, similar to the system palladium-cadmium. Since exact composition of γ and γ_1 could not be determined, their estimated phase boundaries were drawn in dotted lines. Around 92.5 at.% zinc the phase η was found. Between pure zinc and η-phase lies the binary phasefield η+Zn-MK (solid solution of zinc and η). The peritectic reaction of L+γ=η and L+η=Zn-MK were both found to be at 420°C since the DTA didn´t allow for a better resolution. For a better understanding of the phase-diagram, these two reactions were mapped at slightly different temperatures.

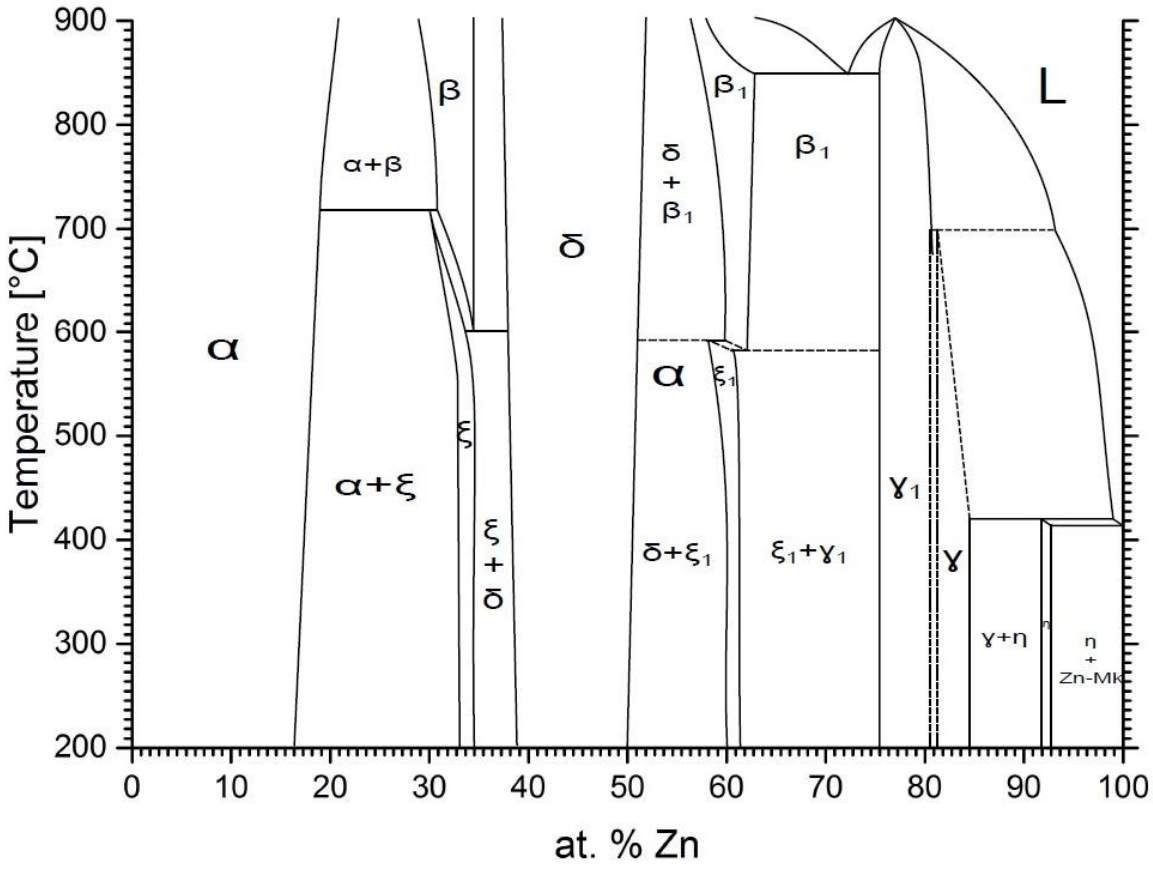

Figure 6 Pd-Zn phase diagram according to Nowotny in 1950

Köster and Zwicker [8] investigated the palladium-zinc system at higher temperatures to clarify a possible transition between the β and β_1 above 900°C. For that purpose they focused mainly on texture analysis and differential thermo analysis (DTA). Because of the low thermo voltage of the Pt/Pt-Rh thermoelements and the high heat dissipation of the used quarz ampullas, the measured thermal effects above 1000°C were prone to errors. A problem with high melting samples is that they often show a poor homogeneity when tempered at lower temperatures. So when preparing samples with a palladium content higher than 30 atomic percent palladium, Köster and Zwicker first prepared samples with 25.6 at. % palladium and sealed it together with the missing palladium, in small pieces, in quartz ampullas. The alloy will melt at around 860°C and react slowly with the small palladium pieces. This technique made it possible to produce homogeneous samples of higher melting alloys. Köster and Zwicker found that a melt of 27.3 at.% zinc decomposes in a eutectic reaction, at 1350°C to the palladium solid solution phase (α-palladium) with a composition of 21 at. % zinc and the β-phase with a composition of 30.5 at. % zinc. The existence of a η-phase around 92.5 at. % zinc was not confirmed by Köster and Zwicker. The ξ_1-phase, as a corresponding room temperature phase of the β_1 phase, at 62 at. % zinc

couldn`t be observed. The phases γ and γ_1 were in good agreement with the already published literature. In contrast to Nowotny, Köster and Zwicker found a small binary phase field between the δ and β phase as well as the δ and β_1 phase, by analysing the texture of samples in this composition region (Fig 7).

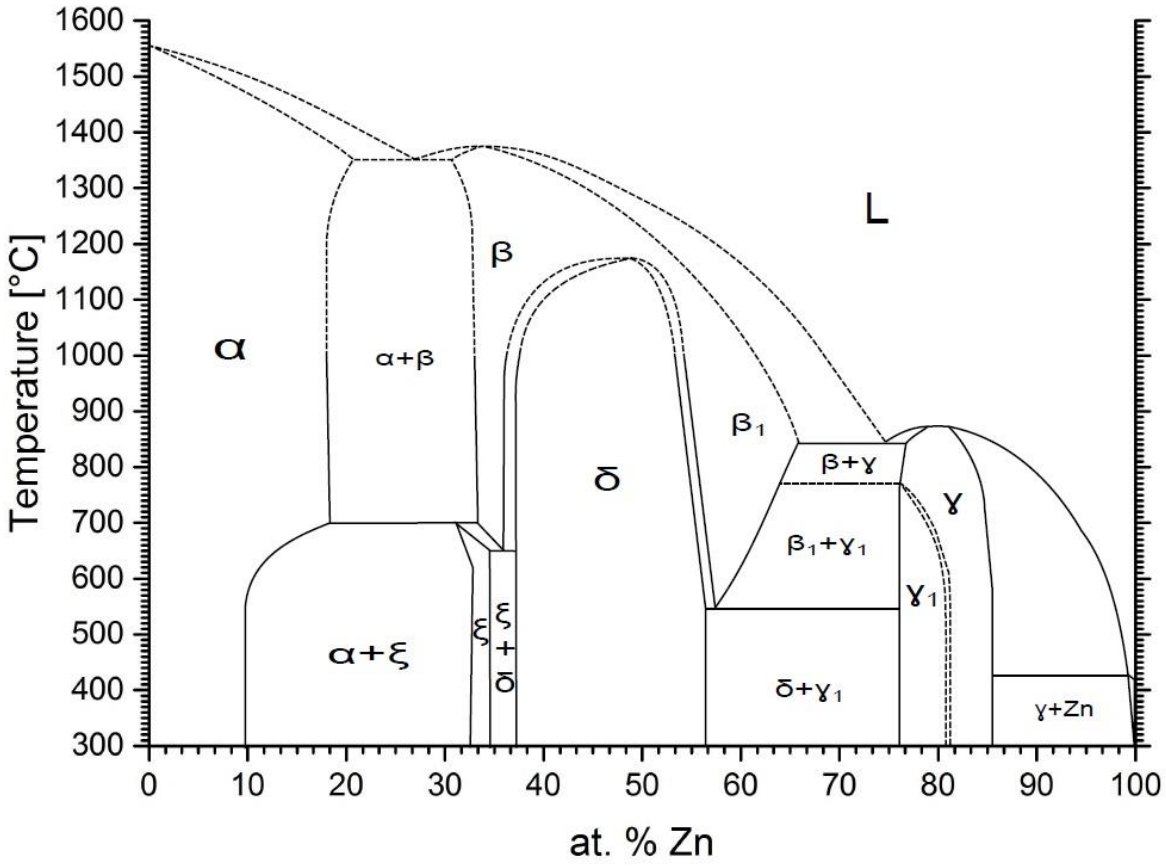

Figure 7 Phase diagram of the palladium-zinc system according to Köster and Zwicker

The phase boundaries of the δ-phase are almost vertical up to 1000°C. Above 1000°C, the phase boundaries begin to merge in a critical point. Thermal effects confirmed a reaction of β_1, δ and the liquid but they were contradicted by texture analysis. Two possible reactions can lead to the closing of the δ-phase field (Fig. 8).

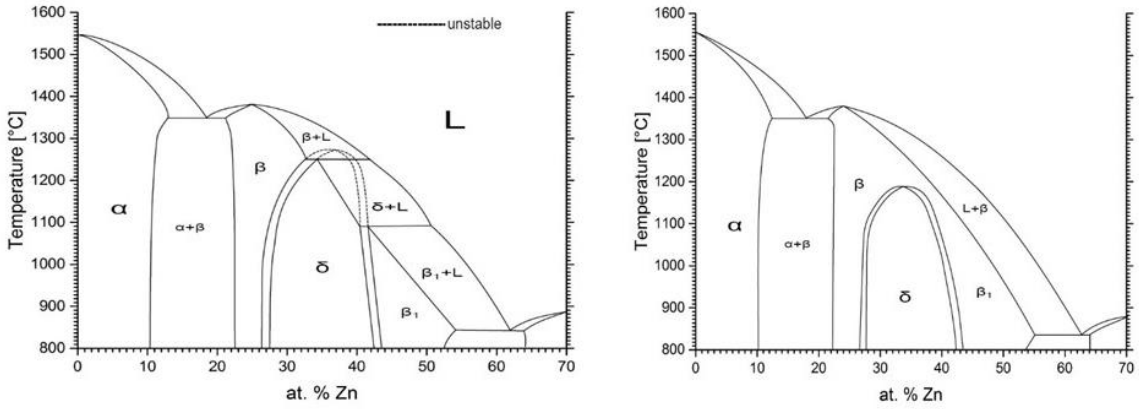

Figure 8 Figure On the left side the β and $β_1$ phase are separated by the δ-phase and three binary phase fields between liquid and the respective solid phase. On the right side the β and $β_1$ become a single phase at higher temperatures.

A first approach to obtain thermodynamic data of the palladium-zinc system, especially from the δ-phase, was made by Kou and Chang in 1975 [9]. The resulting activities lead to the conclusion that the palladium-rich phase boundary of the β_1-Phase has to be changed to 53.5 at. % zinc.

Chiang, Ipser and Chang [10] and investigated the thermodynamic properties of palladium-zinc alloys in 1977. They focussed on measuring the activities of zinc in the palladium-zinc compounds but this will be discussed in section 2.2. . In this section, I will focus primarily on the information on the phase diagram that can be obtained from the measured activities. Chiang, Ipser and Chang verified the existence of the γ and γ_1 and their corresponding phase boundaries. In addition Neumann, Ipser and Chang investigated the structural stability of the B2 and L_{1o} phases in the Pd-Zn system[11]. In contrast to Nowotny et al [7], they found no proof of the existence of a ξ_1-phase since almost no change in activity between δ and γ_1 was observed. If the activities between two compounds are constant, one may assume that a binary phase field exists between those two. In addition, the XRD results showed no evidence of the existence of a ξ_1-phase. The estimated phase boundary of the δ-phase, based on the measured activities, was in good agreement with the phase boundary published by Nowotny et al [7]. The measured activities also allowed for an estimation of the binary phase-field between α and β. Köster and Zwicker[8] reported the phase boundary to range from 18 to 33 at. % zinc at , while the activities suggest a phase boundary from 25.5 to

30.5 at. % zinc. This result was not really contradicting, since Köster and Zwicker [8] reported that their obtained phase diagram might be error-prone above 1000°C.

In 1978 the existence of a ξ_1-phase and the extended solubility range of the β_1-phase were investigated by Alasafi et al [12]. Samples in the composition region between 50 and 82 at.% zinc and the temperature range from 300 to 1000°C were prepared and investigated. The β_1-phase (referred as Pd_2Zn_3) was reported to have a CsCl-structure, which was in good agreement with previous literature. In contrast to Nowotny et al [7], Alasafi et al found the ξ_1-phase and reported it to have a composition of 66 at. % zinc and therefore he referred to it as the $PdZn_2$-phase. The structure of $PdZn_2$ was reported to be an orthorhombic copper-type substructure. Since the structure is similar to γ_1 it could have been easily missed by former authors. The composition of Pd_2Zn_3 was not fully clarified because it was not possible to obtain a homogeneous sample. Based on these samples, Alasafi et al [12] constructed a new segment of the palladium-zinc phase diagram (Fig 9).

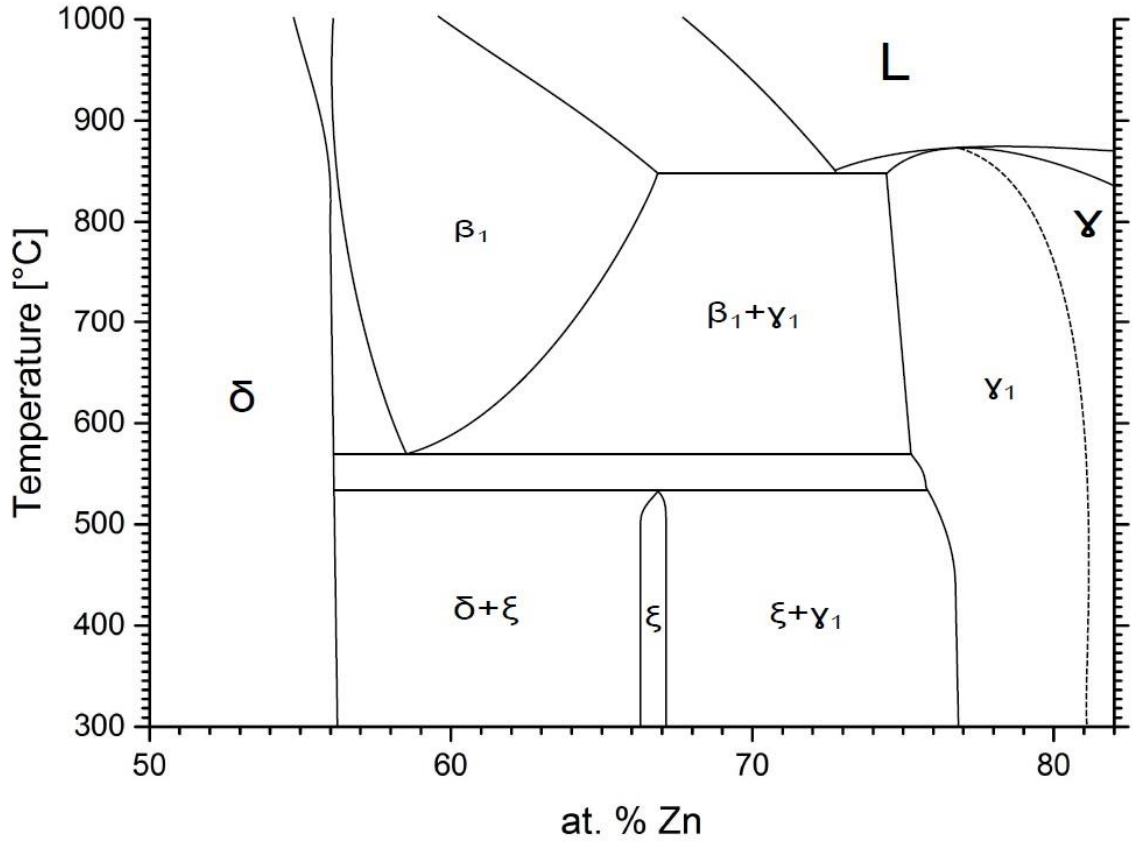

Figure 9 Phase diagram published by Alasafi et al in 1978

Armbrüster [13] researched the structure and properties of the Hume-Rothery-Phases $Pd_{15}Zn_{54}$ and $(Pd_xPt_{1-x})_{2.4}Zn_{10.6}$ in more detail during the course of his master thesis but no complete phase diagram could be concluded from his investigations.

In 2005, Gourdon et al [14] investigated the intergrowth of the γ and γ_1 phase. Several investigations and calculations were made by Gourdon et al [14-16] that dealt exclusively with the γ- and γ_1-phase of the Pd-Zn phase diagram. Through precise single-crystal measurements of six samples in the range of $Zn_{1-x}Pd_x$ (x=0.15-0.25), the homogeneity range of each brass-structure was cleared. Samples below 80 at. % zinc exhibited an orthorhombic structure which could be either F- or C-centred. Above 80 at. % zinc, all samples showed a cubic γ-brass structure with the space group $I\bar{4}3m$. The binary phase field between γ and γ_1 was reported to have a range from 77 to 81 at. % zinc, while the whole γ-brass region said to have a limiting range from 75.7 to 81.9at. % zinc (Fig. 9).These phases can be compared to the Pt-Zn phase diagram reported by Habrecht et al [17].

In 2006 Vizdal et al [18] calculated the palladium-zinc phase diagram via CALPHAD method. The primary dataset for these calculations can be divided into thermodynamic quantities and experimental phase diagram determination. At the time of this work, the Pd-Zn phase diagram was published in two different versions. One version with and one without the η-phase. For a clear assessment, more experimental data concerning the η-phase was needed. For this purpose, the authors prepared samples, which lied in the η + Zn and η + γ two-phase field. Temperatures of 300°C and 400°C were chosen as annealing temperatures. Because of these low temperatures, the annealing time was set to 25 days. X-ray analysis of the samples showed clear evidence of the existence of a hexagonal η-phase. Vizdal et al performed DTA measurements to determine the temperature of the investigated invariant reactions. The two reactions are shown in Table 1. Only the temperatures from the heating curve, measured by an extrapolated peak on-set were taken into consideration. These extrapolated values are afflicted with an error of ±2°C.

Table 1 Temperatures of measured invariant reactions

Reaction	Temperature [°C]
Liq + γ→η	434
Liq →η + Zn	417

In 1993 Iwasa et al [19] tested several supported palladium catalysts (Pd/SiO_2, Pd/Al_2O_3, Pd/ZrO_2, Pd/ZnO) for methanol-steam-reforming (MSR).The catalyst Pd/ZnO showed the promising results with selectivity for MSR of 97%. This report has raised the question if an intermetallic phase of palladium-zinc would also be catalytically active since zinc oxide could be formed during the reaction. Since phase PdZn was reported with a broad homogeneity range, the question was if a correlation between different zinc concentrations of the PdZn (1:1) phase and its catalytic activity existed. Problems were the missing information of the phase diagram at higher temperatures.

In 2010 Friedrich [20] investigated the PdZn-Phase at a temperature above of 900°C and a composition range from 46 to 64 atomic percent. In contrast to previous works Friedrich developed a new method for sample preparation. Pure components zinc and palladium, in form of a powder, were filled in quartz tubes and slowly heated to the melting point of zinc (419°C). After reaching the melting point of zinc the temperature was raised again, but this time with a faster heating rate, to 900°C and annealed for 6 days. This method was used to avoid the evaporation of zinc during the reaction. Friedrich found that the tetragonal PdZn phase has a homogeneity range of 13.8 at. % at 900°C and no transformation of the tetragonal (δ) to the cubic phase (β and β_1) at higher temperature could be observed.
Friedrich [20] investigated the phase diagram further and his results were published in 2013 in his dissertation. The high melting temperature of the cubic phase and the high vapour pressure of zinc made investigations of the melting point very difficult in previous works. In Friedrichs work, a sample of pure PdZn (1:1 Phase, AuCu-type) was quickly heated, quenched at different temperatures and the progress of melting was observed. The sample began to melt at 1458°C instead of 1240°C as suggested by previous literature. Differential thermo-analysis showed no phase transition between tetragonal and cubic structure and only one endothermic effect at 1458°C was observed. X-ray analysis of phase pure samples of PdZn (CuAu-type), which were annealed at 1230°C, exhibited exclusively the tetragonal structure. The results suggested that the previously reported transformation of the tetragonal structure to the cubic structure at 1175°C and melting of this cubic structure at 1240°C is wrong. A new phase diagram (Fig. 10) was drawn according to this new information. Note that the η-phase is not included in this work. The symbols in this phase diagram assessment represent data from following literature: △ Nowotny [7]; □ Chiang [10]; ○ Köster and

Zwicker [8]; ◇ Friedrich [20]; ▽ Alasafi [12]; ● Armbrüster [13]; ▲ Gourdon [14-16]. Köster and Zwicker had already drawn a hint, of how the tetragonal PdZn phase might close at higher temperatures (Fig. 8). By simply extending the melting point of the tetragonal PdZn-phase to 1460°C, the new phase diagram could be obtained.

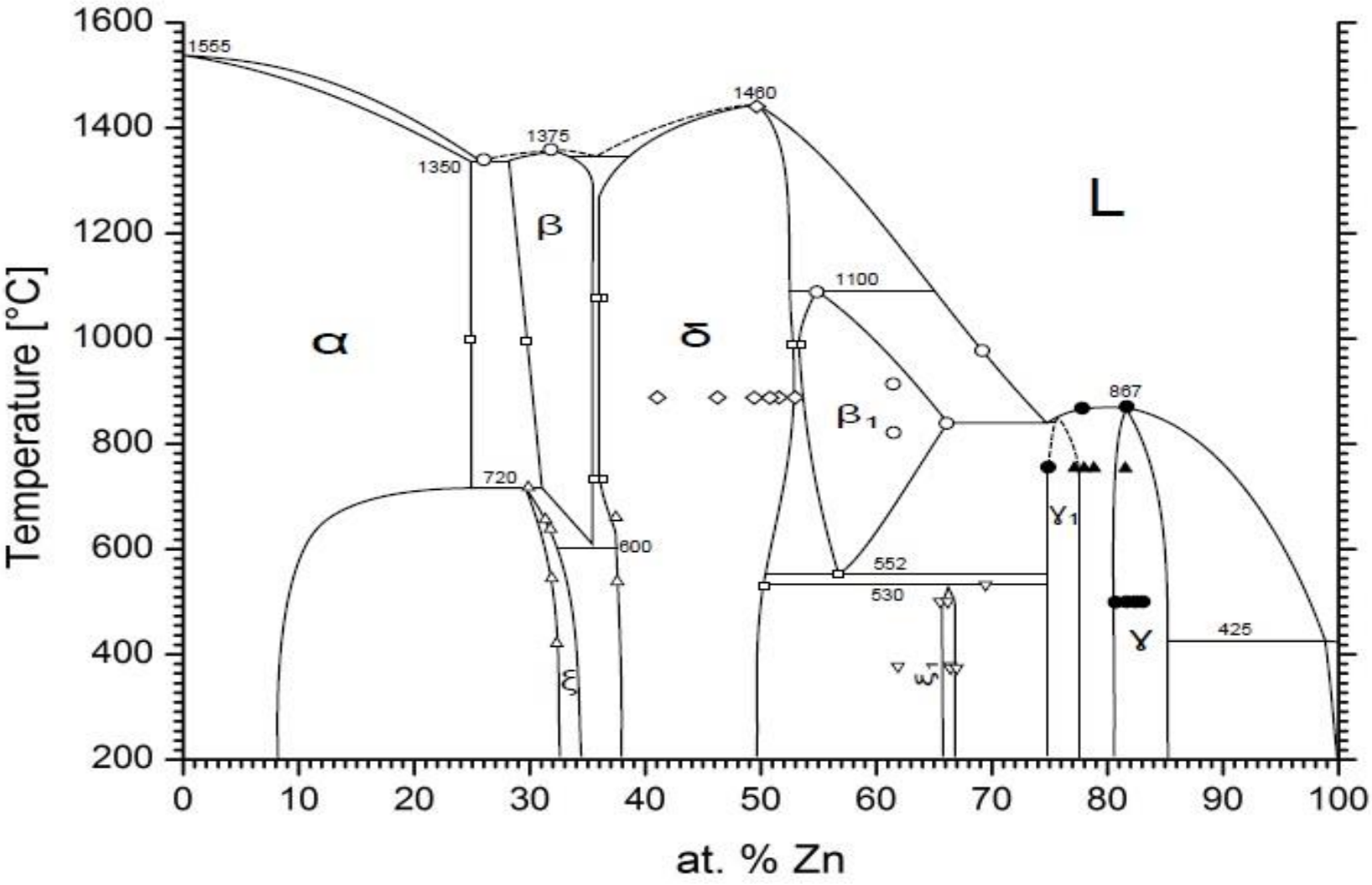

Figure 10 Phase diagram of palladium-zinc system without a high-temperature cubic PdZn phase

Including the work of Vizdal [18] into the published phase diagram by Friedrich [20] lead to the phase diagram that was used for experiments and calculations in this work. On the first look it might seem that the η-phase might not play a large role in the thermodynamic calculations of the palladium-zinc phase diagram but its existence drastically influences the equilibrium. Since the η-phase is in equilibrium with the γ-phase. In this regard, the existence of the η-phase influences the calculations of the phase boundary of the γ-phase and therefore the solution parameters of the γ-phase or to put it differently, it influences the width of the γ-Gibbs energy curve. Changing the Gibbs energy curve of the γ-phase will influence its neighbouring phase γ_1 and so on. Adding a phase or changing the Gibbs energy of one phase in equilibrium, usually requires a change of all neighbouring phases as well. The resulting phase diagram is given in Figure11.

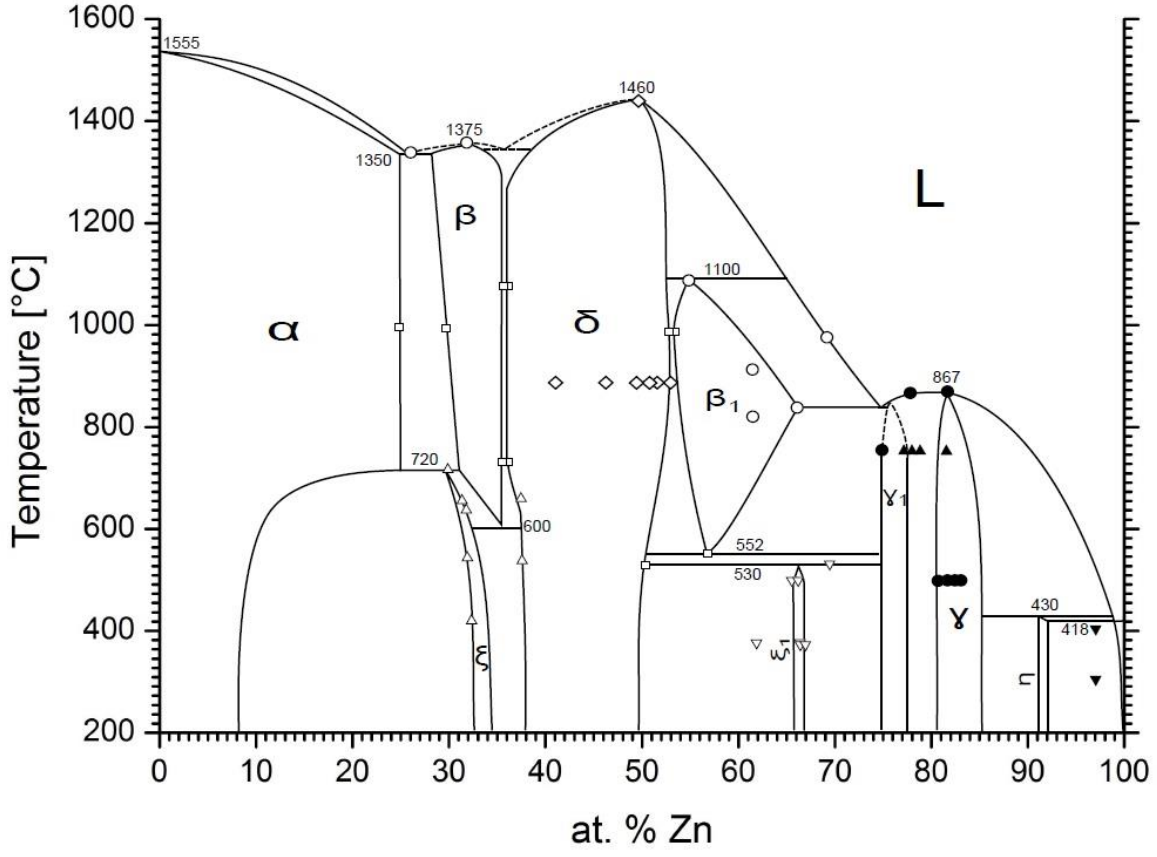

Figure 11 Phase diagram assessment used in this work

△ Nowotny [7]; □ Chiang [10]; ○ Köster & Zwicker [8]; ◇ Friedrich [20]; ▽ Alasafi [12]; ● Armbrüster [13]; ▲ Gourdon [14-16], ▼ Vizdal [17]

2.2 Thermodynamic Data

In 1975 Kou and Chang [9] investigated the thermodynamic properties of the ordered PdZn-phase (δ-phase). A non-isothermal isopiestic method was used to determine activities at a source temperature of 1273°C but different sink temperatures. From these obtained activities, the partial molar Gibbs free energy of zinc was derived. They noticed a major change in activity of zinc over a composition range of two atomic percent. This suggested a high negative Gibbs free energy of formation for the stoichiometric compound. This work was continued in 1977 by Chiang, Ipser and Chang [10], with more samples and several "runs" over a larger temperature range. All runs showed comparable results with the previous study. Again, a drastic change in activity at the composition $Pd_{50}Zn_{50}$ was observed. Plotting activities against the composition indicated a small two-phase field between δ and β of 36 to 36.5 at.% zinc from 1000°C to 1300°C. One run focussed exclusively at the palladium α-phase and the binary phase field between α and β. The activities suggested a phase boundary between 35.7 and 36.5 at. % zinc at 1000°C. The partial molar Gibbs energy and enthalpy of formation of the δ-phase were calculated by a theoretical approach provided Kou and Chang [9].

Taking the mentioned thermodynamic data and phase diagram information as a basis, Vizdal [18] calculated the palladium-zinc phase diagram via CALPHAD method in 2006. Since no other thermodynamic data was available at that time, Vizdal focussed exclusively on the data obtained by Chiang, Ipser and Chang [10]. The latest version of the SGTE Unary database (Version 4.4) was used as a description of the elements palladium and zinc.

In 2008 Amore et al [21] measured enthalpies of formation of the γ and γ_1 phase in the composition region between 77-80 at. % zinc of the palladium zinc system. The heat of formation was obtained by high temperature drop calorimetry and extrapolated to 300K. These values were not included in this work

2.3. Catalytical Data

The catalytic investigations of the supported $Pd_{1-x}Zn_x/Al_2O_3$ samples are compared to intermetallic bulk $Pd_{1-x}Zn_x$ samples investigated by Friedrich [20]. The identical experimental set-up, allows for a good comparison between the bulk material and the supported nanoparticles. Friedrich [20] used graphite as a filling material, which was tested in course of a catalytically preliminary assessments. For that purpose, different amounts of graphite were mixed with the same amount of a reference catalyst ($Cu/ZnO/Al_2O_3$). The results showed that the CO_2-selectivity is independent from the amount of added graphite and that graphite showed no activity in MSR or WGS. Additionally the catalytic activity of powdered elemental palladium (commercially available) was investigated. The CO_2-selectivity of powdered elemental palladium (Chempur, 99.9%, 20-32 µm) is comparable to the CO_2-selectivity of supported palladium (eg. Pd/Al_2O_3 or Pd/SiO_2) as shown in Figure 12. For a comparison between powdered elemental palladium and the intermetallic compounds $Pd_{1-x}Zn_x$, the temperature dependence of catalytic activity (Fig. 13) and CO_2-selectivity (Fig. 14) of these compounds was measured. Note that during all catalytic measurements, the samples were pre-treated with H_2 at 200°C for one hour. Zinc-rich samples showed an increased CO_2-selectivity and activity over a large temperature range. All catalysts exhibited a deactivation (decrease in activity) after 20 hours of testing. Comparing the CO_2-selectivity of zinc-rich samples with samples of supported PdZn/ZnO showed that zinc or zinc oxide, which was formed during the reaction, has a direct influence on the selectivity. Formed zinc oxide was confirmed by in-situ XPS measurements. In contrast to the zinc rich samples, samples with higher palladium content are comparable to elemental powdered palladium.

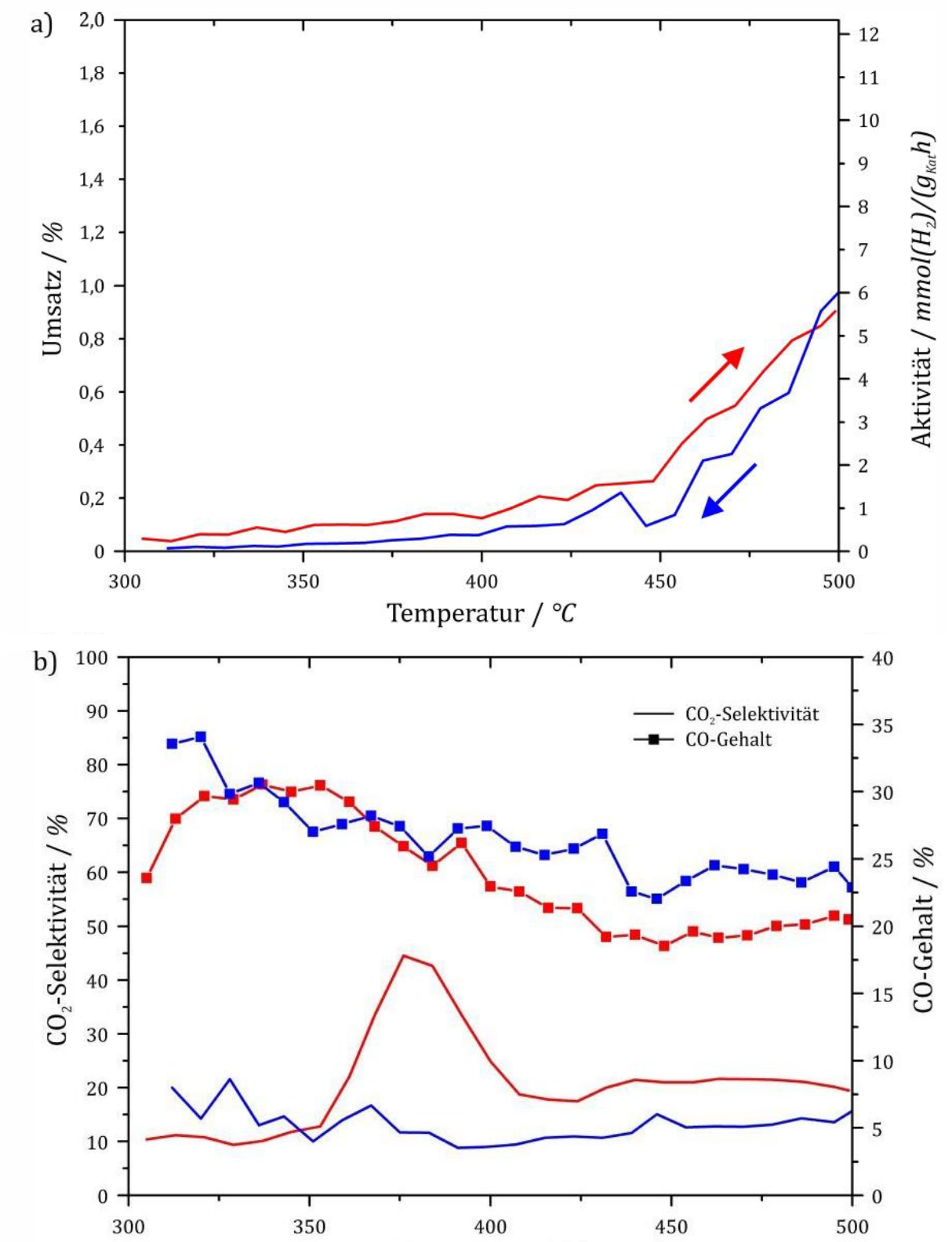

Figure 12 a) Conversion and activity of elemental powdered palladium during heating (red) and cooling (blue). b) CO_2-selectivity and CO production during heating (red) and colling (blue) [20]

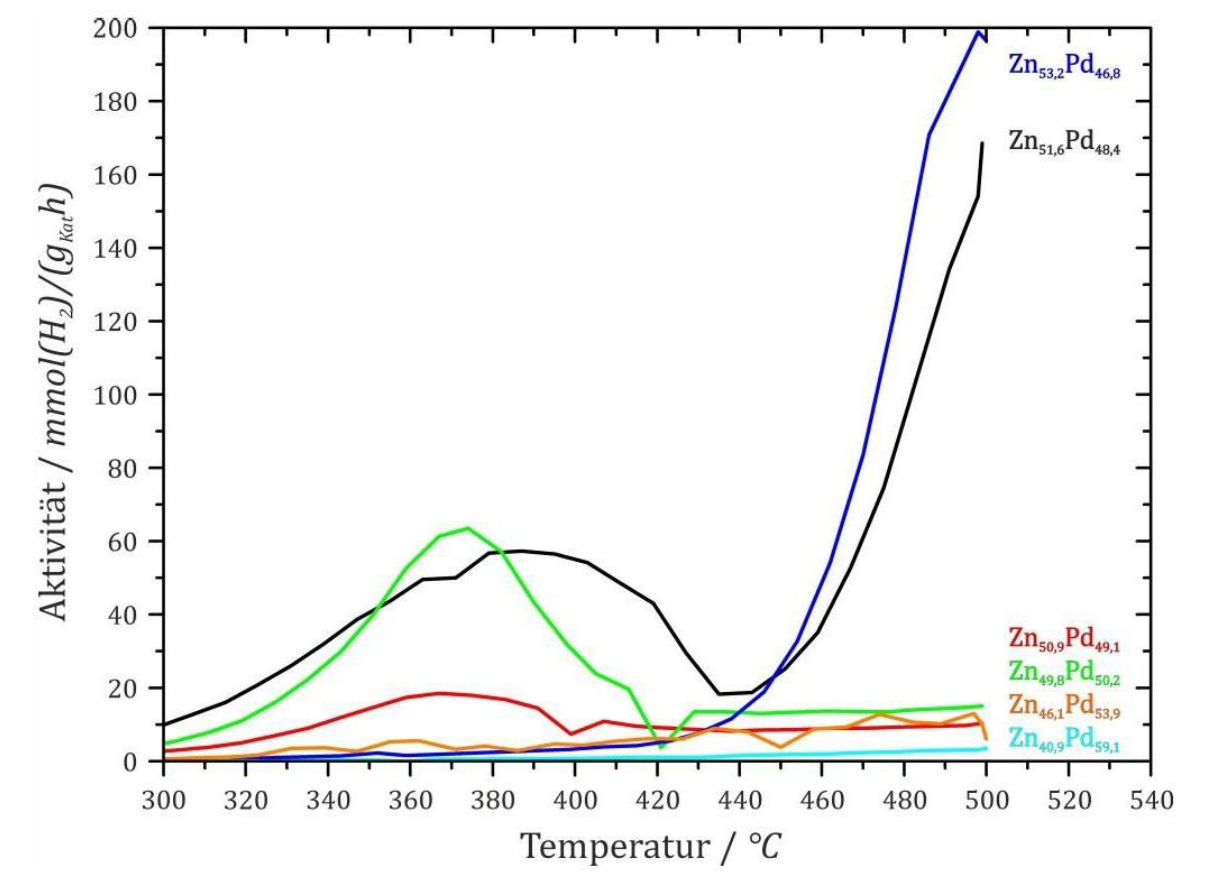

Figure 13 Temperature dependence of the activity of $Pd_{1-x}Zn_x$ bulk samples under MSR-conditions (MeOH:H_2O = 1:1) [20]

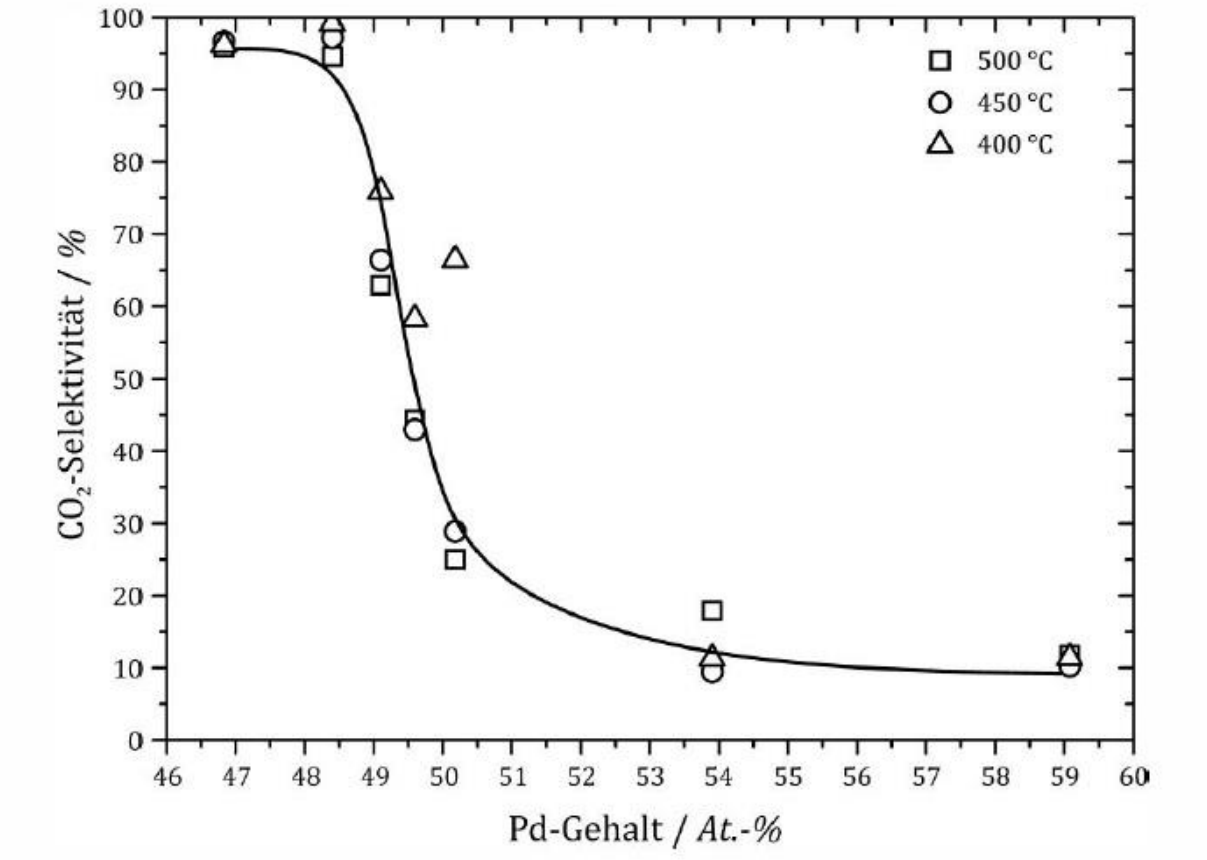

Figure 14 CO_2-selectivity at different compositions and temperatures under MSR-conditions (MeOH:H_2O = 1:1) [20]

The high CO_2-selectivity of PdZn/ZnO was investigated by Friedrich et al in 2013 [22]. Friedrich et al investigated ZnO-supported PdZn particles and their synergy in terms of CO_2-selectivity during methanol steam reforming. They used high-resolution transmission electron microscopy (HRTEM) for imaging the catalyst material before and after catalytic testing. The catalyst (ZnO/PdZn) showed low CO_2-selectivity at the beginning of the MSR (<40%) which increased up to 97% during 2 hours, at a constant temperature of 523K. Since the catalyst showed a very poor CO_2-selectivity at the beginning of the MSR experiment, it was assumed that the catalyst material changes during the reaction. In order to verify the synergy between ZnO and intermetallic PdZn the catalyst material was investigated after the reaction in HRTEM and HAADF (High Angular Annular Dark Field). HRTEM imaging revealed that small ZnO particles were formed on top of the PdZn-particles during the MSR experiment. It was therefore proofed partially oxidising PdZn to ZnO leads to a larger interface between PdZn and ZnO. This interface influenced the activity of water and therefore also the CO_2-selectivity.

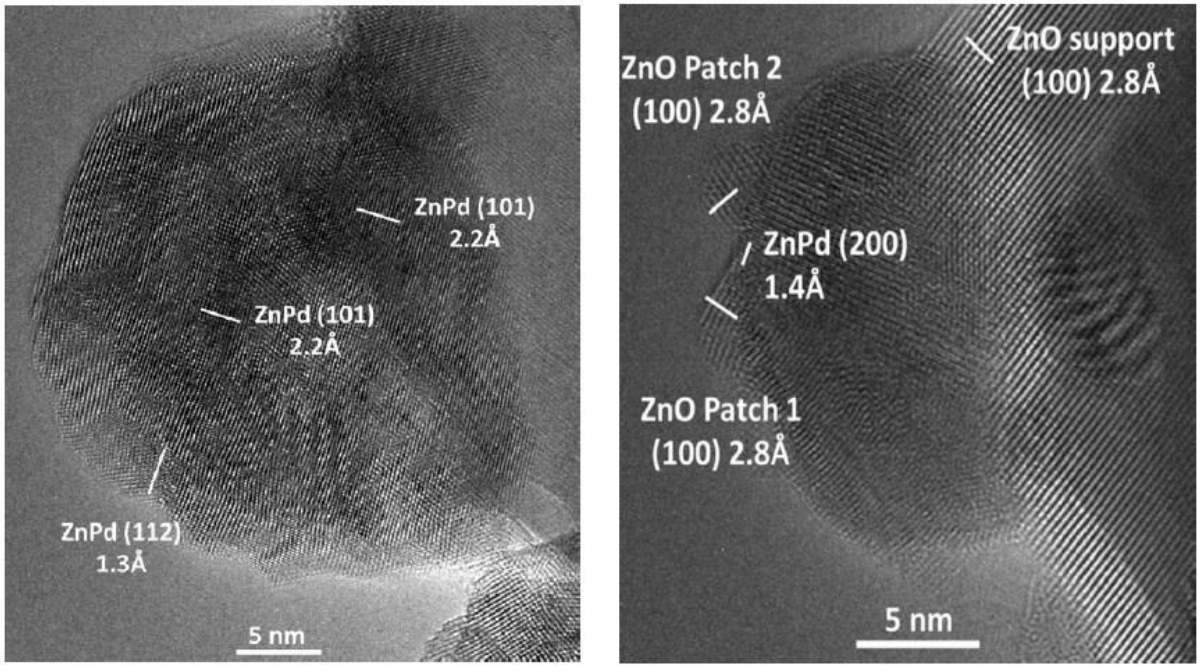

Figure 15 HRTEM imaging of single polycrystalline PdZn paticle before the reaction (left) and after the reaction (right) with two additional ZnO patches [22]

3. Sample preparation

3.1. General procedure

The aluminium oxide powder, 5wt. % loaded with palladium, was bought from Sigma-Aldrich. The loading was confirmed by ICP-OES measurements. The analysis was performed by the Max-Planck Institute for chemical physics of solids (MPI) in Dresden. The loading was reported to be 4.77 wt. % palladium which was taken into account when calculating a desired sample composition of palladium and zinc.

The ordered powder was already partially oxidized to palladium oxide and showed a black colour while the non-oxidized powder exhibited a brownish colour. To reduce the formed palladium oxide, the powder was reduced in a 5% Hydrogen in Argon atmosphere. The reduction was first carried out by the MPI in Dresden and the reduced powder was sent to Vienna. For the reduction, a reactor was used, which will be described in more detail in the section 4.8. . A reduction temperature of 400°C and a constant gas flow, which was hold for two hours, were chosen as reaction conditions for the reduction. Later on, the reduction was performed in Vienna using a much simpler approach. The powder was put on a small quartz glass shuttle, which was transferred in custom-built quartz tube (Fig. 16).

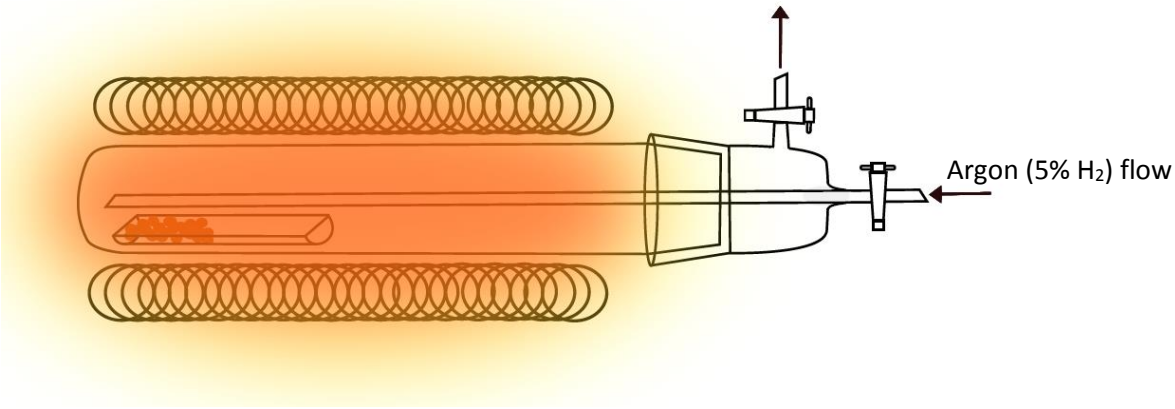

Figure 16 Custom-built reduction equipment

For the reduction process, the reaction conditions reported by the MPI were used but the gas flow could only be roughly regulated by a reduction vent. During and after the reduction the powder was exclusively handled in argon to avoid any possible oxidation of the powder. After reduction, the quartz tube was kept under argon and transferred into the glovebox where the powder was stored in gas impervious vessels. A direct use of the powder as described above was not possible, because it still showed residual water. The first series of samples resulted in complete oxidation of the zinc-mirror in the quartz glass tube during the

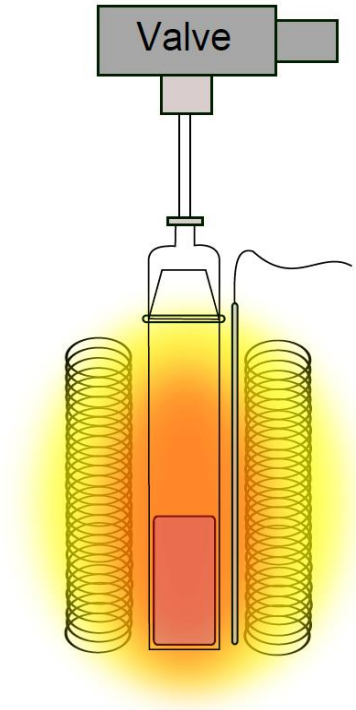

Figure 17 Experimental set-up for removing residual water and gases from the powder

heat treatment. Therefore no reaction of zinc with the nano-powder occurred. The tubes were then opened and the unreacted nano-powders were re-used for another reaction. In a next step, it was decided to heat the sample powders for several hours to remove any remaining adsorbed water or hydrogen, which could have diffused into the palladium during the reduction. Therefore, the powder was placed into a graphite tube (diameter 30mm) which was then transferred into a larger quartz glass tube. The experimental set-up was evacuated and heated under dynamic vacuum. The temperature was controlled by an external thermo element, which was placed next to the sample (Fig 17). The pressure started to rise at 200°C (Fig. 18) and remained high for 2-3 hours, depending on the amount of nano-powder. Upon reaching around 480°C the pressure dropped very quickly to its initial value and the release of water, hydrogen or other gases was considered to be finished. After the heat treatment, which was performed under dynamic vacuum, the powder was transferred into the glovebox, while still being under vacuum, and transferred into a gas impervious vessel. This procedure was chosen to prevent any contact of the nano powder with oxygen or water. Sample masses around 3-4 grams were used for the heat treatment.

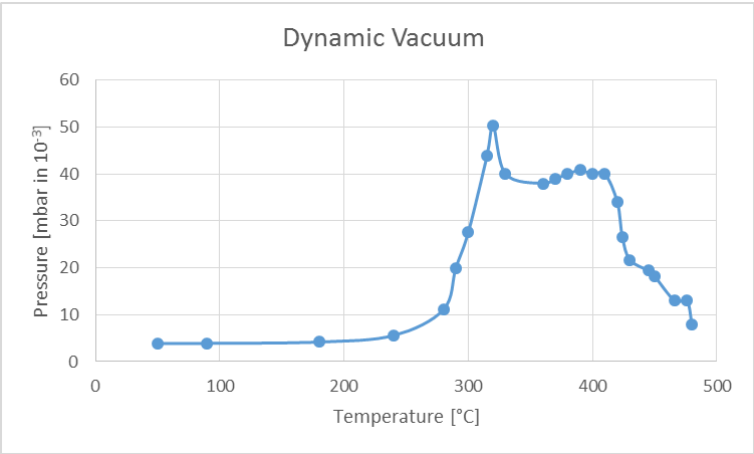

Figure 18 Pressure/Temperature curve of the heating process

The element zinc was bought from Alfa Aesar (zinc shot, 1-5mm, 99.999%). Since zinc oxidizes slowly at air, it needed to be cleaned from possible zinc oxides. Therefore, small pieces of zinc (5g-7g) were sealed under vacuum of about 5-6*10^{-3} mbar into a quartz glass tube and transferred into a two-zone furnace at the temperatures of 500°C (hot side) and 300°C (cold side). In contrast to zinc oxide, zinc has a very high vapour pressure, so it can be easily purified via distillation. The time, needed for this distillation depended mainly on the temperature gradient and the amount of zinc. Pure zinc will deposit on the "cold side" while zinc oxide will remain on the "hot" side.

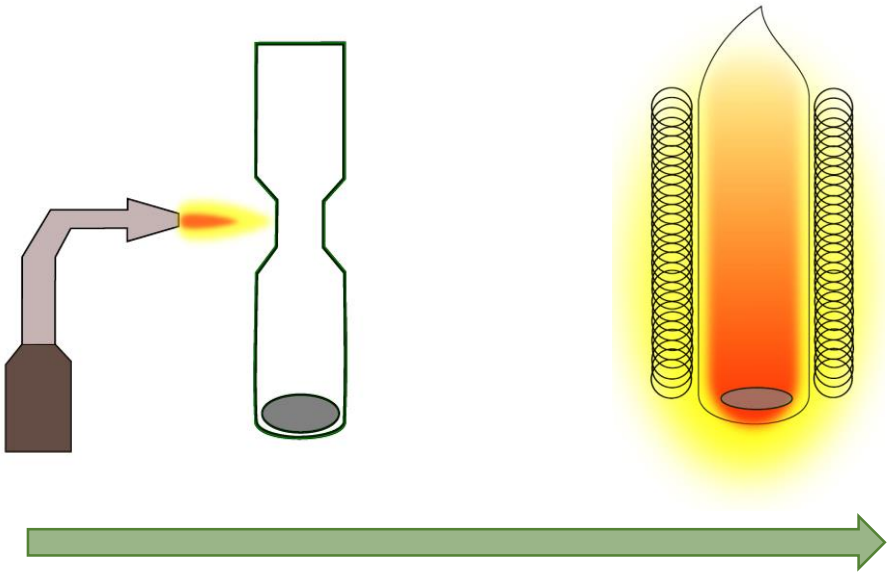

Figure 19 Purification of Zinc via distillation

For the samples, purified zinc was weighed on a balance with an accuracy of ±0.1mg and transferred into a custom-built quartz glass tube (Fig. 19). Then a vacuum of 5-6*10^{-3} was applied to the tube and a "cooler" flame was used to clean the tube from residual water. After cleaning the tube from water, zinc was evaporated by heating the solid zinc with a H_2/O_2 torch. The evaporated zinc, deposited on the colder part of the quartz glass tube creating a zinc-mirror. This "zinc-mirror" was needed to avoid any direct contact between zinc and the palladium aluminium oxide powder (Pd/Alox powder). Then the valve connecting quartz glass tube and vacuum line was closed, keeping the zinc-mirror under vacuum, and transferred into the glovebox with the valve still connected to the quartz glass tube. This was a very important step because after evaporation, zinc exhibits a very large surface, making it more reactive towards oxygen.

The amount of nano-powder, which was needed for the desired composition, was calculated according to the amount of used zinc. It was assumed that the nano-powder was loaded with 4.77 wt.% palladium. One should note that a weighing error of ±10mg Pd/Al_2O_3 powder, when the total amount is 650mg, results in an error of 0.35 at. % in composition. Therefore losing a small amount of powder, when transferring it from the vessel into the quartz glass tube, has only little effect. To avoid any contact between the nano-powder and the zinc-mirror a long cone was used to fill the powder intro the quartz glass tube. Working with this nano-powder proofed to be extremely challenging since it adhered to all used glass parts. To clean the cone from residual powder a pipe cleaner was attached to a wire and used to clean the cone. After cleaning the cone, a small quartz glass tube piece was placed into the tube (Fig. 20), which should provide additional support during melting of the quartz glass. The tube was reattached to the vacuum valve and sealed. This experimental set-up was then transferred outside the glovebox and mounted on the vacuum-line. Before opening the valve connecting the vacuum-line and the quartz glass tube, the vacuum line was evacuated and filled with argon 3 times, to make sure no oxygen or water could diffuse into the quartz glass tube.

After evacuating and purging with argon (Argon 5.0 >99.999%) the glass tube was evacuated again below $5*10^{-3}$ mbar and then sealed. Due to the high vapour pressure of zinc, sealing the quartz glass tube had to be done very careful, to avoid evaporation of zinc. If zinc accidentally evaporated and condensed on the upper part of the silica tube, it was possible to bring back the zinc by heating the upper part of the silica tube. For this procedure the dynamic vacuum needed to be switched of. Otherwise the zinc vapour would flow towards the vacuum-line and not in the direction of the zinc-mirror.

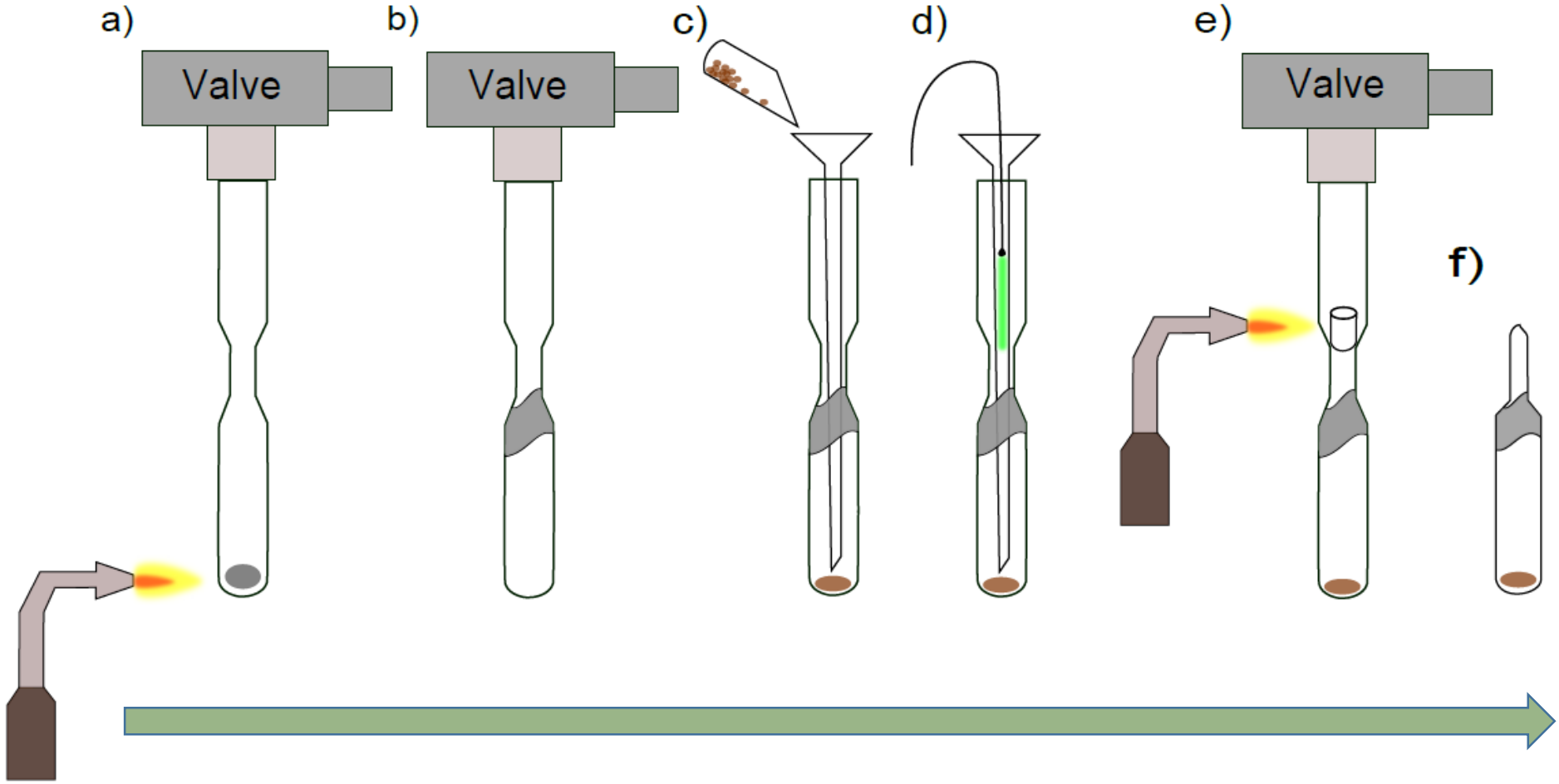

Figure 20 Sample preparation procedure. a) evaporation of zinc by heating it with a H_2/O_2 torch, b) resulting zinc mirror, c) filling in the powder via a cone, d) using a pipe cleaner to remove residual particles from the cone and transferring them into the quartz glass, e) sealing of the glass vessel, f) sealed sample for temperature treatment

All samples were prepared as described before. Since only a single sample could fit into the two-zone furnace, they were individually prepared and then transferred into a 2-zone furnace with an exact temperature gradient. The temperature was measured with a type K thermo element, before placing the sample into the furnace, and the temperature profile was recorded. The profile was needed to determine the exact temperature between the "hot" and the "cold" side of the sample. The "hot" side is the so-called reaction-side, where the reaction between the palladium, which is sitting on top of the alumina oxide and the zinc vapour, takes place. Figure 21 shows an example of a temperature profile of a conventional two-zone furnace. The samples were not equally long and therefore the temperature was adjusted in such a way that the "hot" side would be at exactly 30cm and the "cold" side was calculated with the help of a polynomial, obtained from the temperature profile.

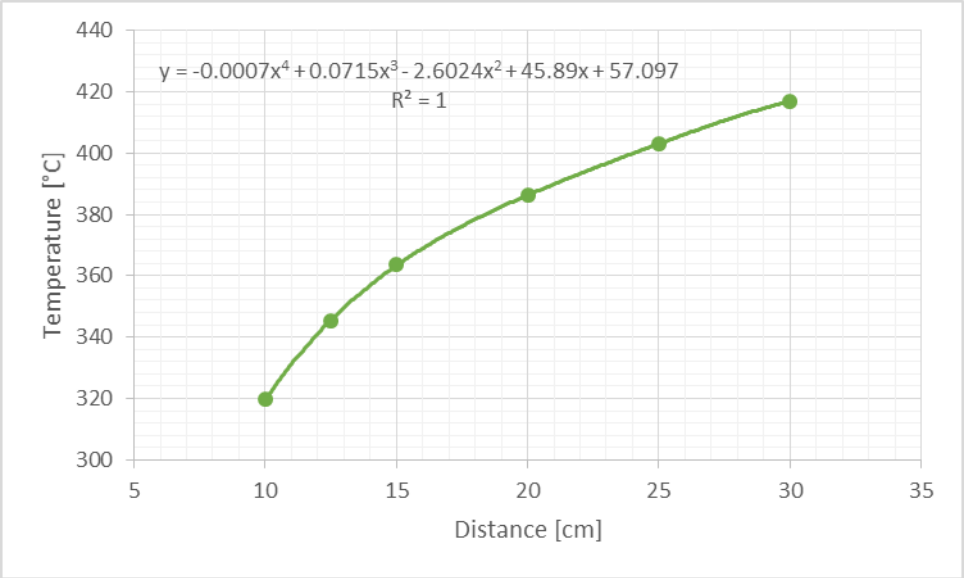

Figure 21 Temperature profile of a two-zone furnace

Measuring the "reaction-length" inside the sample instead of the total length was crucial for an exact calculation of the temperature gradient. The thickness of the glass also needed to be taken into account. Figure 22 shows a comparison of sample length (blue) and reaction length (red). Since the powder is not localised in one point but covers a length of roughly 0.5 to 0.8 cm in the sample crucible an uncertainty in temperature has to be expected.

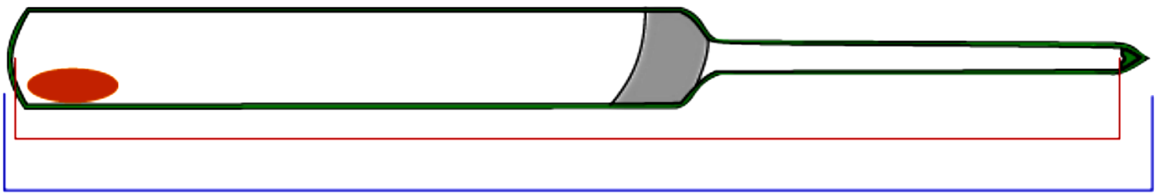

Figure 22 Total length of the sample (blue) and real sample length (red)

The minimum temperature of the cold side, where zinc still showed a reasonable fast transportation time were determined by using samples without the nano-powder. The temperature of the "hot"-side in these trial experiments will therefore be the "cold"-side in experiments with "real" samples. The trial experiments showed that 310°C was a reasonable temperature for starting a reaction. A lower temperature was needed in order to slow down the reaction of zinc vapour with elemental palladium, which should result in a more homogenous reaction product. If the reaction would happen too fast, it might be possible that preferable the upper layers of the sample powder will react with the zinc vapour, resulting in a higher zinc concentration in those nano particles but a lower zinc concentration in the other nano-particles. This would influence the catalytic activity of the nano-powder as well as the X-ray diagrams.

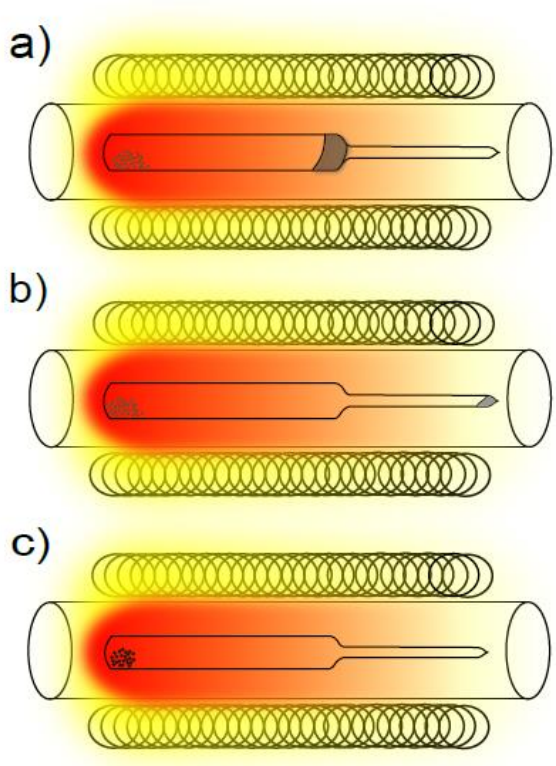

Figure 23 a) beginning of the reaction, b) after a day zinc condensed on the sink side, c) fully reacted sample

After 1 day of reaction time, the samples were taken out and shaken, to mix the nano-powder. The reaction was considered to be finished, when no zinc residue was visible inside the reaction vessel. It was observed that samples with higher zinc concentration needed a longer time to fully react. If the reaction was not finished after 4 days, the temperature on both sides was raised. The 3 different states of samples are shown in Figure 23. It was observed that when a sample reached the state b (Fig. 23) the reaction slowed down. The reason might be that zinc was deposited in the corners of the

quartz glass where it formed small crystals. To speed up the reaction, the sample was removed from the furnace and quenched in water. The zinc was removed from the corners by heating the zinc part of the sample with a H_2/O_2 torch. The heating was continued till the residual amount of zinc formed a zinc-mirror at the same position as at the beginning before the reaction. After this short heat-treatment the sample was put back into the furnace.

After the reaction was complete, the sample was quenched and transferred into the glovebox. The vessel was opened with a glass cutter and the nano-powder, now containing $Al_2O_3/Pd_{1-x}Zn_x$, was filled into gas impermeable bottles. Some powder always remained on the walls of the reaction vessel, so it was not possible to measure the weight gain of the powder. Sample compositions are shown in Table 12. A question that remained was, if the distribution of zinc after the reaction was homogenous or inhomogeneous. It was assumed that, if the distribution of zinc was inhomogeneous, an additional isothermal heat treatment of the powder after synthesis could improve the distribution of zinc. For this purpose, small amounts of sample PaWi015, were sealed in a quartz tube, as described above and heated in an isothermal furnace for 2 weeks at 416°C.

3.2. Samples for ICP-MS

For ICP-MS (**I**nductively-**C**oupled-**P**lasma – **M**ass **S**pectroscopy) analysis, the samples needed to be digested in order to analyse their palladium and zinc content. Approximately 1 to 2mg of each sample was weighed and transferred into a plastic vile. The accuracy of the scale was ±0.05mg. The viles were filed with 5 millilitres nitric acid (20%), closed and put into an automatic microwave digestion system. The samples were heated up to 200°C degrees with a ramp time of 4 minutes and were hold at this temperature for 6 minutes. The power of the microwave was set to 300 watt. After cooling down, the samples were taken out of the microwave and the solution, now containing palladium and zinc, was transferred into another vile for further dilution. A problem of this digesting technique was the remaining alumina oxide which couldn`t be dissolved in 20% nitric acid. The remaining precipitate was washed with deionized water, centrifuged and the resulting washing solution was combined with the sample solution. This washing process was repeated 3 to 4 times. The resulting solution was diluted with deionized water until their weight was close to 10 gram. The samples were diluted with 1% nitric acid in the ratio 1:1000.

Standard dilution series for calibrating the ICP-MS for palladium and zinc were prepared separately to exclude a possible interaction between zinc and palladium. The standard solutions of zinc had a concentration of 10.000±30µg/mL in 4% nitric acid (CPI-International, 99.999%) and the palladium standard solution had a starting concentration of 1000±0.3µg/mL in 4% nitric acid (CPI-International, 99.999%).

The standards were diluted with 1% nitric acid and the concentrations of the standards were determined gravimetrically, using a balance with an accuracy of ±0.05mg. The resulting concentrations of these dilution series is shown in section 9.2. . Additional to the standard dilution series, two blanks of the dilution solution were produced. One was made before preparing the dilution series and the other one after, to exclude possible changes in the dilution solution. For analysis the isotopes of zinc and palladium, which showed the smallest deviation from the calibration curve, were selected. The isotope ^{68}Zn was selected for calculating the zinc content and for palladium, the deviation from the calibration curve was similar for many isotopes so the mean value of those isotopes (^{104}Pd/ ^{105}Pd/ ^{106}Pd/ ^{108}Pd and ^{110}Pd) was derived and used for calculating the palladium content. Knowing the concentration of palladium, zinc and the sample mass allowed a calculation of the weight percentages of palladium and zinc. From these weight percentages, the composition of the palladium-zinc nanoparticles could be derived. The results showed that almost all samples contained lesser amount of zinc than the nominal composition (Section 9.2).

A setback of this technique is that only an overall composition of the nanoparticles can be determined. It could be possible that some nanoparticles have a higher and some a lower concentration of zinc.

3.3. Samples for TEM

For **T**ransmission-**E**lectroscope-**M**icroscopy (TEM) measurements, the samples needed to be deposited on a sample carrier. For this purpose, a suspension of a sample was produced. It should be noted that during all TEM-measurement the samples were exposed to air. For the suspension, about 1mg of the examined sample was transferred into an Eppendorf vessel and suspended in 1mL cyclohexane. After shaking, the Eppendorf vessel was put into an ultra-sonic bath for 5 minutes. Now the sample carrier was immersed into the suspension. The sample carrier consists of a fine copper grid on a very thin carbon film. After immersing the sample carrier into the suspension, it was dried with a red light. The first measurement revealed that the particles agglomerated. For the next measurements, the Eppendorf vessel

was put into the ultra-sonic bath for 1 hour and the sample carrier was immersed and dried several times to increase the concentration of the nanoparticles. This change in preparation of the samples showed a good particle concentration and almost no visible agglomeration.

3.4. Sample for AFM

For AFM (**A**tomic-**F**orce-**M**icroscopy) measurements, a series of suspensions of the unreacted Pd/Alox powder was prepared. The concentration range of these suspensions was between 1mg/mL to 10mg/mL. For a sample carrier, a slide of a light microscope was cut in such a way that the resulting piece had the dimensions of roughly one square centimetre. This piece was than cleaned by putting it into beaker filled with ethanol, which was put into an ultra-sonic bath. After 15 minutes, the carrier was taken out and dried at air. For the suspension, 1-10 milligram of the Pd/Alox powder was weighed, transferred into an Eppendorf vessel and filled with one millilitre of cyclohexane. Similar to the TEM preparation, the Eppendorf vessels where put into an ultra-sonic bath for one hour. Two millilitres of this suspension where applied on the sample carriers and dried on air. Since all sample carriers dried and were transported on air, oxidation of the palladium could be possible.

3.5. Samples for SEM

Scanning-**E**lectron-**M**icroscopy (SEM) was used to determine the seize distribution of the alumina oxide particles. The preparation of the sample was similar to the preparation of the AFM-sample but instead of glass, a single crystalline silicon waver was used as a carrier.

3.6. Samples for “catalytic activity”

The activity of the investigated $Pd_{1-x}Zn_x$/Alox nanoparticles was measured in a “plug-flow” type reactor, which is explained in detail, in the chapter for experimental methods. During synthesis, all nanoparticles were kept either under vacuum or argon. Therefore, the preparation of the samples for catalytic measurements was also performed inside the glovebox. 20 milligram of the nanopowder was mixed with 200mg of graphite, to dilute the catalyst bed. The Reactor tube was transferred into the glovebox, filled with the mixture, sealed, then transferred outside the glovebox and mounted in the reactor.

4. Experimental Methods

4.1. Inductive-Coupled-Plasma Mass Spectrometry

Inductive-**C**oupled-**P**lasma **M**ass-**S**pectrometry (ICP-MS) was developed in 1971 at the University of Surrey, UK. Geological scientists wanted a new analytical mass spectrometer to characterize their samples, which should be able to analyse 4 to 6 samples per hour and detect all metallic elements between lithium and uranium. The main advantage of ICP-MS in contrast to the more conventional **I**nductive-**C**oupled-**P**lasma **O**ptical-**E**mission-**S**pectrometry (ICP-OES) or graphite furnace atomic absorbtion (GFAA) is its detection limit. A very high sensitivity, up to sub 1ppb (µg/kg), and online sample introduction are the advantages of the ICP-MS method. [23]

An ICP-MS system consists of the introduction system, the ionisation source, the interface region, a system for focussing, the mass separator and the detector illustrated in Figure 24.

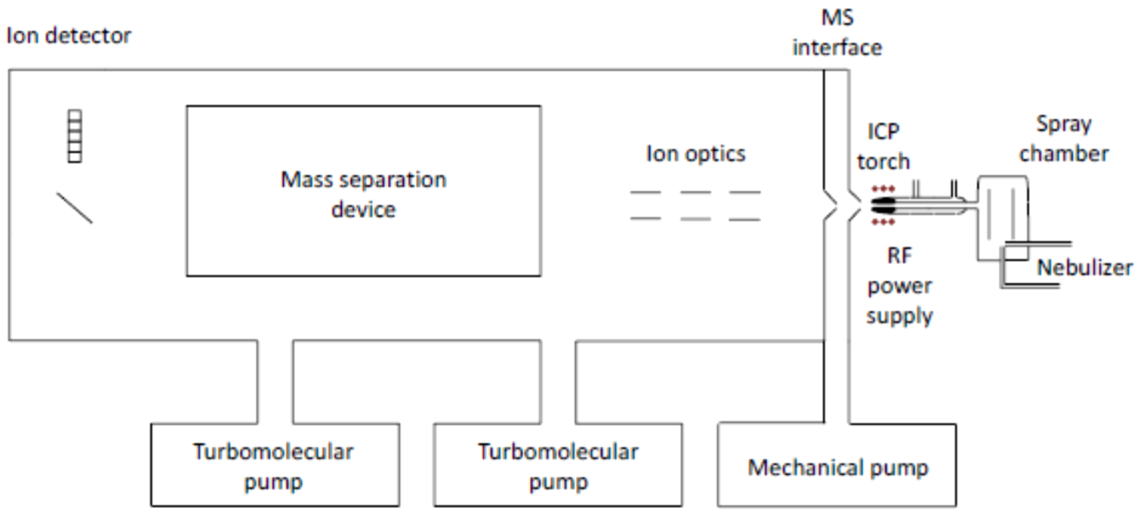

Figure 24 Schematic of an ICP-MS system

In most cases, samples are introduced as a liquid solution and pumped into the sample introduction system. If the samples are crystalline, they need to be digested, which is usually done in an automatic microwave and if necessary diluted. If the concentration is too high (>1000 ppm), physical properties like density, viscosity and surface tension will influence the droplet seize distribution and therefore ICP-MS-peaks will be broadened.

The sample introduction system is composed of two parts. The first part is for aerosol generation and the second part manages the droplet selection. Peristaltic pumps are pumping the liquid sample, normally at ~1ml/min, into the nebulizer. In the nebulizer system, the liquid is pumped directly into a constant argon gas flow, which breaks up the

liquid into small droplets (Fig. 25). This mechanism is comparable to the mechanism of a conventional hair-spray can.

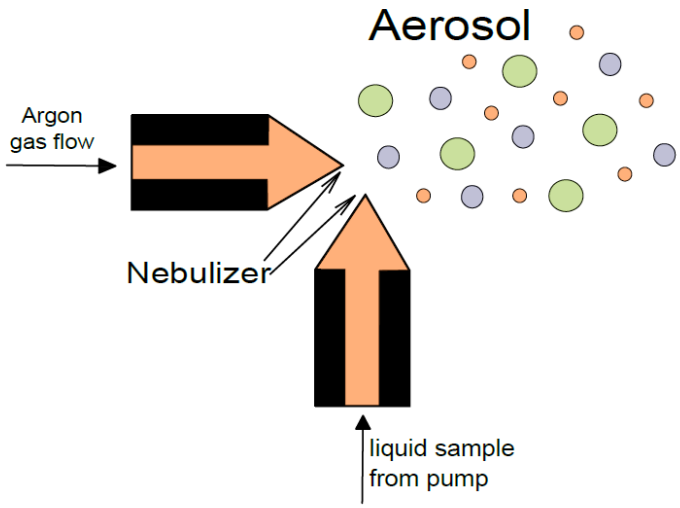

Figure 25 Aerosol generation in an ICP-MS spray-chamber

Figure 25 shows a good example of the droplet seize distribution. The difference in size between the large droplets (>10µm in diameter) and the small droplets (~5-10µm in diameter) can be quite large. Small droplets have faster desolvation and vaporization than larger droplets. Droplets larger than ~8µm give no signal and therefore, the droplets need to be separated. The separation happens inside the spray chamber. The droplets are separated, by gravity and only small droplets are allowed to enter the plasma. [24]

As sketched in Figure 24, the next part of the ICP-MS system is the ionization source. The ionization source consists of a radio frequency coil and three tubes, the outer tube, the inner tube and the sample injector tube. The inner tube delivers the gas (usually argon), needed for the plasma generation (flow rate of 12-17L/min) while the outer tube supplies an auxiliary gas (flow rate of ~1L/min), which helps to modify the position of the plasma, relative to the injector. The sample injector tube carries the sample aerosol at a flow rate around 1L/min.

The radio frequency coils are generating an oscillating electromagnetic field by oscillating an alternating current inside the coil. A Tesla coil is used to produce a spark, which will ionize a few argon atoms. These electrons and ions are accelerated by the oscillating electro-magnetic field causing them to collide with other argon atoms. If the acceleration is fast enough, the collision will lead to ionization of the colliding argon atoms. The resulting ions

and electrons will again be accelerated causing further collisions and ionisations of argon atoms resulting in a bright, tear dropped shape plasma. Since the acceleration of the electrons and ions is caused by an electro-magnetic field, the process is called “inductively coupled plasma generation” (ICP). The plasma has a temperature up to 10000K. The droplets are first dried and vaporized before being atomized and ionized by the plasma. After ionization, the sample now consists of singly positively charged ions.

The next and part is the interface region. This region separates the mass-spectrometer, which works at a high vacuum (10^{-6}mbar) and the plasma torch which works at atmospheric pressure. The interface-region consists of merely two metallic cones (nickel or platinum) and a mechanical pump which is keeping the pressure between those cones at roughly 1 mb. After passing the interface region, Ions enter the fourth part, the so-called ion-focussing-system. The main function of the system is to focus the investigated ions to the mass analyser while discriminating other present species such as neutral elements, small particles and photons. After passing through the interface region the ion-beam will experience a sudden change in pressure (from 1mbar to 10^{-6}mbar), which will broaden the beam. Additionally the positively charged ions will interact and repel each other, resulting in an additional broadening of the beam. The smaller ions will be pushed outwards while the larger ions will remain in the beam centre. These two phenomena for beam broadening are compensated by the ion-focussing-system. The electro-magnetic-lenses of the focussing system are positively charged, so that the smaller ions at the edge of the beam will be pushed back into the inner part of the beam. Neutral particles or electrons will not be focussed and simple crash into the outer encasement of the focusing-system (Fig. 26).[23]

After being focussed, the ions will reach the mass-analyser where they are selected according to their mass-to-charge-ratio (m/z ratio). Which type of mass analyser is used differs from each ICP-MS device. The three main mass analysers are “time of flight” (TOF), “double-focusing magnetic-sector field” and quadrupole. Literature reports show that about 90% ICP-MS system are equipped with a quadrupole mass analyser. The difference between these anaylizer is mainly their resolution. While a Magnetic Sector Mass Spectrometers offers the highest resolution and quantitative performance, its running costs exceeds those of a conventional quadrupole mass analyser. TOF mass analyser can be used for simultaneous detection of elements, providing a full mass spectra in a short time but it requires a pulsed ion beam or pulsed ionization.[25]

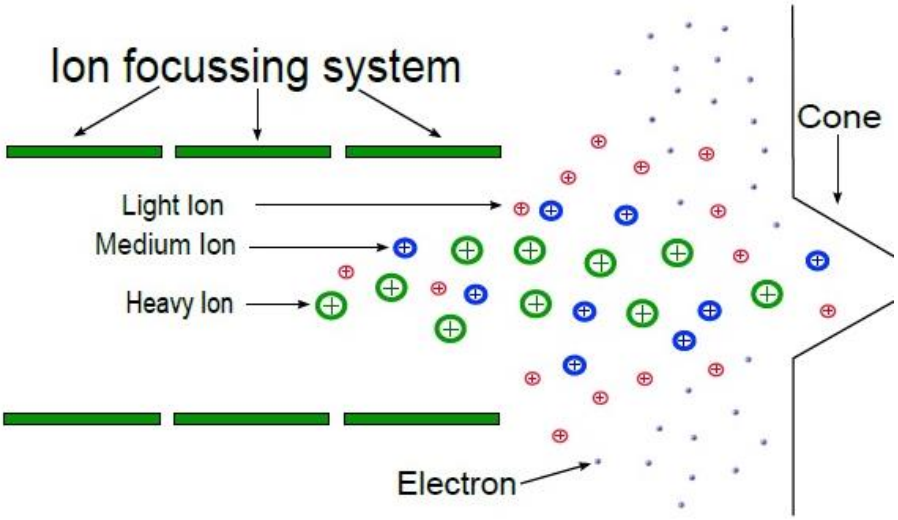

Figure 26 Ion focussing system

After mass-selection the ions will reach the detector, which is usually a channel electron multiplier. The selected ions are colliding with a semiconductor type material causing secondary emission of an electron. This electron is then multiplied by a dynode resulting in a signal in form of a voltage.

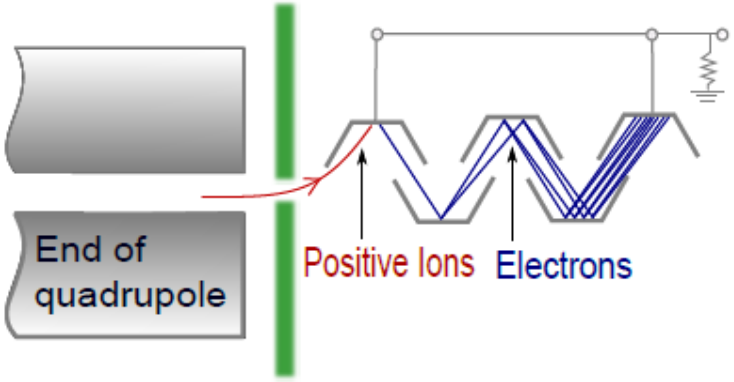

Figure 27 Schematic of an ion-analyser

One of the main challenges of mass spectroscopy is the so-called mass interference. If more than one ion species is present, there can be interferences between atomic or polyatomic species, which have the same mass to charge ratio (m/z). This interference can be avoided by using a magnetic-sector-field-high-resolution ICP-MS where species with the same m/z-ratio can be separated.Certain elements like calcium and iron can form argides (MAr+) which can cause additional interference.If the cones in the interface region are made of nickel, traces of up to 5ppt nickel can be found. Using platinum as cone-material will prevent the forming of these orifice ions. [26]

4.2. Isopiestic

4.2.1. The Isopiestic Method

The isopiestic method was first used for the determination of vapour pressures of aqueous solutions. To understand this method, a very simple example where two tanks A and B, both containing aqueous solution of two salts x and y, are in contact via the gas phase is used.

Transfer of solvent water between these two tanks can only occur through the gas phase. After some time (minutes up to a few hours) equilibrium is reached and no change in mass between these two containers can be measured. Thermodynamic theory states that, if two liquids, which are in contact via the Gas phase, in equilibrium the chemical potential of water in those two containers is equal.

$$\mu_x^{eq}(cont.A,T,p) = \mu_y^{eq}(cont.B,T,p) \quad (1)$$

Since the masses of salts used to prepare the solutions are already known, the mass of the containers in equilibrium yields the equilibrium molalities. [27]

Assuming one of the containers, in this example container A, contains a standard KCl solution. For this standard Solution, the dependence of osmotic coefficient on molality is known from other experiments (eg. Pfeffersche Zelle). If one of the two solutions is already known, the equation 2 can be rewritten to:

$$[\mu_1^* - \varphi_x \cdot R \cdot T \cdot V_x \cdot m_x] = [\mu_1^* - \varphi_y \cdot R \cdot T \cdot V_y \cdot m_y] \quad (2)$$

Here m_x and m_y are equilibrium molalities, V_x and V_y are equilibrium Volumes and φx and φy are the respective osmotic coefficients. The Gibbs-Duhem equation states that the chemical Potential of two mixed substances are linked by the following equation:

$$n_x \cdot \left(\frac{d\mu_x}{dn_y}\right) + n_y \cdot \left(\frac{d\mu_y}{dn_y}\right) = 0 \quad (3)$$

This equation can be changed for a solution with the molality mx and a molar mass M_x.

$$\left(\frac{1}{M_x}\right) \cdot \left(\frac{d\mu_x}{dm_y}\right) + m_y \cdot \left(\frac{d\mu_y}{dm_y}\right) = 0 \quad (4)$$

Now another assumption can be made to make the equation more understandable. Since the whole System is pressure dependent, we assume that the pressure is equal to the standard pressure. With this assumption equation 4 simplifies to

$$\left(\frac{1}{M_x}\right) \cdot \frac{d[\mu_x^* - \varphi_x \cdot R \cdot T \cdot M_x \cdot m_y]}{dm_y} + \frac{\left[\mu_y^0 + R \cdot T \cdot \ln\left(m_y \cdot \frac{\gamma_j}{m^0}\right)\right]}{dm_y} = 0 \quad (5)$$

Equation 5 can be further reduced to:

$$\left(\frac{\varphi}{m_y}\right) - \frac{d\varphi}{dm_y} + \left(\frac{1}{m_j}\right) + \frac{dln(\gamma_j)}{dm_j} = 0 \quad (6)$$

In order to solve this equation, a series of experiments has to be made, to determine the molality dependence of the osmotic coefficient (φj).

The activities can be obtained by plotting φj against mj [28].

4.2.2. The pseudo Isopiestic Method

The pseudo isopiestic method was first used by Seith, Krauss and Hargreaves in 1938 to determine the activities of zinc in the Cu-Zn-system [29-30]. This method is used to determine the activity of volatile Components of metallic systems. Volatile metals and semi-metals are for example Zn, Sn, Te, Sb, Li, K and Hg.

In the pseudo Isopiestic method a non-volatile component A, which is kept at a defined Temperature (T_S), is exposed to the vapour of a volatile component B from a reservoir, which is kept at a lower Temperature (T_R). In order to perform this experiment, the non-volatile component A needs to have a negligible vapour-pressure at the Temperature (T_S).

In contrast to the common isopiestic method, this method is used in a non-isothermal way. After applying a high enough temperature gradient, component A will equilibrate with the vapour of component B at the Temperature (T_S). The equilibrium condition, which is given in equation 8, shows that the chemical potential of B at the temperature T_R must be equal to the chemical potential of B in the formed $A_{1-x}B_x$ alloy at T_S, which means that at the temperature Ts, over the sample must be equal to the vapour pressure of pure B at the temperature T_R can be made.

$$p_B(T_s) = p_B^0(T_R) \quad (7)$$

How can the activity of B over the sample be calculated? If the pressure of pure B in the System is constant and independent of the temperature gradient, the pressure inside the system is given by the reservoir temperature T_R. Due to this simplification, the activity of B in the Sample $A_{1-x}B_x$ can be calculated by:

$$a_B(T_S) = \frac{p_B(T_S)}{p_B^0(T_S)} = \frac{p_B^0(T_R)}{p_B^0(T_S)} \quad (8)$$

$p_B\ (Ts)$….partial pressure of component B over the sample

$p_B^0(Ts)$….pressure of the pure volatile component at Ts

$p_B^0(T_R)$….pressure of the pure volatile component at Tr

The pressure of the pure volatile component at different Temperatures can be calculated using the standard tables for “Selected Values of Thermodynamic Properties of Metals and Alloys and supplements” [31]. These calculated activities still have to be attributed to a certain composition of the system A-B. The easiest way to calculate the composition is by weighing the samples before and after the experiment. From the weight gain, a composition can be calculated. Other possible analysis methods are X-ray fluorescence, EPMA or chemical Analysis (ICP-AAS, ICP-MS etc.). The next figure shows a sketch of a simple non-isothermal experimental set-up.

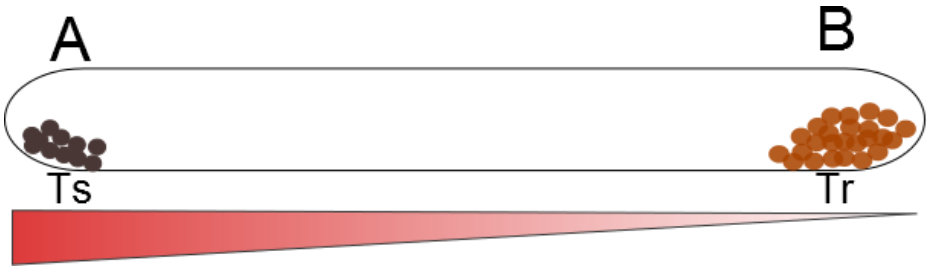

Figure 28 Simplified pseudo-isopiestic experimental set-up

Usually the experimental set-up is modified, so that more samples can be investigated simultaneously. While the reservoir temperature (T_R) will be the same for all samples, which are placed along the temperature gradient, the sample temperature (T_S) will differ for each sample.

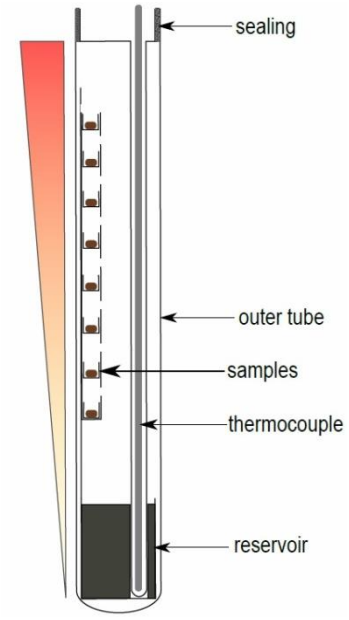

Figure 29 Schematic of a conventional isopiestic set-up

Figure 29 shows the experimental set-up which is used for pseudo-isopiestic-experiments with more samples. Since all these experiments are usually performed in quartz glass tubes, the pressure of the volatile component should be kept under 1bar. Literature showed that pseudo-isopiestic-experiments were used between 10^{-1} bar (Aluminium systems) and 10^{-10} bar (Selenium systems). [32]

When the activities and the composition are known, it is possible to calculate the partial molar enthalpy for zinc, which can be used to convert the activities, measured at the temperature Ts, to a standard temperature by linear regression.

Considering a solution of two components A and B, the Gibbs energy is a function of pressure, temperature and the two components. $G = G\ (p, T, n_A, n_B)$.

$$dG = \left(\frac{\partial G}{\partial p}\right)_{T,n_A,n_B} dp + \left(\frac{\partial G}{\partial T}\right)_{p,n_A,n_B} dT + \left(\frac{\partial G}{\partial n_A}\right)_{p,T,n_B} dn_A + \left(\frac{\partial G}{n_B}\right)_{p,T,n_A} dn_B \qquad (9)$$

The last two terms are of special interest when for an isopiestic experiment since these terms deal with the change in Gibbs energy when a solution of two components (n_1,n_2) is formed. The partial derivative of the Gibbs energy with respect to the moles of an component (n_i) is called “chemical potential (μ_i)”.

$$\mu_i = \left(\frac{\partial G}{\partial n_i}\right)_{T,P,n_{i\neq j}} = \bar{G}_i \qquad (10)$$

The chemical potential is also the partial molar free Gibbs energy.

If a mixture is an ideal solution, the partial vapour pressure of each component (methanol or water) can be calculated by Raoult’s Law:

$$p_i = x_i p_i^* \rightarrow x_i = \frac{P_i}{P_i^*} \qquad (11)$$

A universal symbol for the standard state was introduced by IUPC in 1970. The sign ° or * are possible. In this master-thesis, if a quantity is referred to the reference state, it will be denoted by °.

$$\mu_i = \mu_i^0 + RTlna_i \qquad (12)$$

Equation 12 represents clear relation between the measured activities in a pseudo-isopiestic experiment and the chemical potential. [33]

If the chemical potential is the differentiated Gibbs energy with respect to the component i, it can be assumed that it should be possible to obtain other thermodynamic properties from

the measured activities. In a system in an isopiestic experiment, for example palladium-zinc, the partial molar Gibbs energy of zinc can be calculated by:

$$\left(\frac{\partial G}{\partial n_i}\right)_{T,p} = \bar{G}_i = \mu_i = RTlna_i \tag{13}$$

Using the Gibbs-Helmholtz equation it is possible to calculate partial molar enthalpy of zinc. The Gibbs-Helmholz equation is:

$$\left(\frac{\partial(\Delta\bar{G}_{Zn}/T)}{\partial(1/T)}\right)_p = \Delta\bar{H}_{Zn} \tag{14}$$

We substitute equation 13 for $\Delta\bar{G}_{Zn}$:

$$\Delta\bar{H}_{Zn} = \left(\frac{\partial(RTlna_{Zn}/T)}{\partial(1/T)}\right)_p = R\frac{\partial lna_{Zn}}{\partial 1/T} \tag{15}$$

Calculating the partial molar enthalpy of zinc requires plotting $\ln a_{Zn}$ against 1/T for one single composition (Fig. 30). This plot should give a straight line with the slope $-\Delta H_{Zn}/R$ and the intercept $\Delta S_{Zn}/R$.

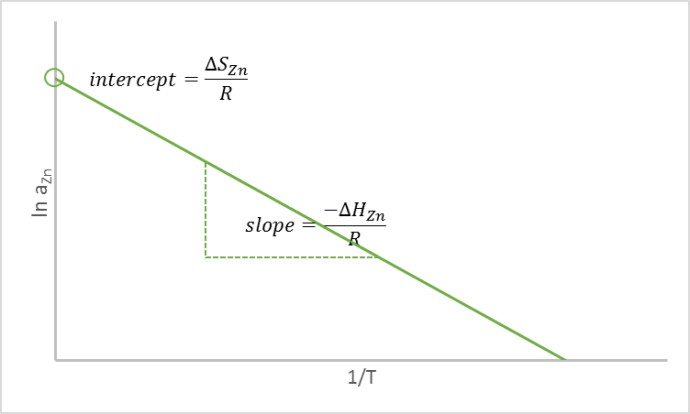

Figure 30 Logarithmised activieties of zinc plotted against the temperature [K]

In an isopiestic experiment, the temperature T will be the sample temperature Ts of the sample. While the experiment yield activities for fixed temperatures, the plot above can be used to derive activities for a distinctive temperature which wasn´t measured in the experiment. This extrapolation can proof rather helpful because it allows for a comparison of experimentally found activities with activities published in other literatures at different temperatures. [32]

4.2.3. Errors of the pseudo-isopiestic-method

The first possible error of a measurement is an error in temperature measurement. Two uncertainties are possible: The first uncertainty is the accuracy of the used thermocouple in

the given temperature range. Usually thermocouples have an error from ±0.1 up to ±1.5°C depending on the type of thermocouple. The second uncertainty is the position of the thermocouple. Since a temperature gradient usually is non-linear, the possible error depends on the temperature profile of the furnace. Measuring the temperature at the steep part of the profile-curve can lead to a larger error than measuring it on the flattened part of the curve.

The second error is a deviation in the analysis of the sample composition. For a better understanding of the weighing error, a short example from the Pd-Zn System is shown. If a sample mass of 0.5g before the reaction has 1g after the reaction, the sample consists of 0.5g Zn and 0.5g Pd. This leads to a weight percentage (wt. %) of 50 % for both elements. Converting this weight percentage into atomic percentage (at. %) results in a composition of 62 at. % Zn and 38 at. % Pd. If the weight of zinc and palladium is changed to 0.501g and 0.409g the found composition is 62.03 at. % Zn and 37.97 at. % Pd. In this example, a weighing error of ±1mg leads to an error of ±0.03 at. % in the composition. This error increases if the total sample mass is lowered. A third possible error is the molecular composition of the the gas phase. While zinc vapour consist mainly of isolated zinc atoms, the situation is different for example antimony. When antimony is used as a volatile component all molecular species, which might be formed during the reaction in the gas phase need to be considered. In this case Sb(g), Sb_2(g), Sb_4(g) would need to be considered to calculate the total pressure. The fourth and very often discussed error is the assumption of a constant pressure of the volatile component from the reservoir. If the temperature (T_R) is set too low the resulting pressure of the volatile component will be small and the so-called Knudsen-Flow might occur inside the quartz glass tube. Knudsen flow occurs at a pressure from $1 – 10^{-3}$ mbar, where the mean-free-path length is longer than the diameter of the tube (l > d). [32] Assuming that the gas inside the tube has a particle density n and a collision-cross-section σ. Now a very fast particle with the radius r_1 is fired into a gas where the molecules don´t move and have a radius r_2. A collision occurs when the distance between the centre of the fast particle and the centre of the molecule is smaller than r_1+r_2. The collision-cross-section σ is therefore calculated by:

$$\pi \cdot (r_1 + r_2) = \sigma \tag{16}$$

If the particle density is n, then the mean number of particles inside the volume σx is nσx. Exactly one collision will occur along x if $n \cdot \sigma \cdot x$ is 1. When this is true x is called mean-free-path-length l.

$$n \cdot x \cdot \sigma = 1 \tag{17}$$

$$l = \frac{1}{n \cdot \sigma} \tag{18}$$

If the mean-free-path-length l is larger than the diameter of the quartz tube in our pseudo-isopiestic-experiment the probability of a collision between two gas molecules is lower than the probability of a collision between a gas molecule and the wall of our quartz tube. In that case, the pressure inside the quartz tube is no longer constant but differs along the tube. Therefore measuring activities as described above will only lead to false results since the condition for a constant pressure is no longer fulfilled [34]. The Knudsen flow can be corrected for by a simple formula [32].

4.3. X-ray-Diffraction

4.3.1. Production of X-rays

X-rays were discovered in 1895 by Wilhelm Conrad Röntgen. X-rays are part of the electromagnetic Spectrum with a wavelength from 10^{-8} to 10^{-13}m. Before the introduction of SI-units, a conventional unit for X-ray-wavelength was Angstrom (Å) [35]. The correlation between the metric unit nanometre and Angstrom is:

$$1\,\text{Å} = 10^{-10}m = 0.1nm$$

X-rays are generated when highly accelerated electrons hit on a target material. The production of X-rays happens in so-called, X-ray tubes shown in Figure 31. Two metal electrodes are sealed into a ceramic tube under vacuum, and a high voltage is applied between them. In most cases, the anode material is copper and the cathode material is tungsten. When the cathode is heated while applying a high voltage, electrons will be emitted from the cathode and accelerated, due to the high voltage, towards the anode. Upon collision, the kinetic energy will be transferred into X-ray-radiation (1%) and heat (99%). Since 99% of the incoming energy is transferred into heat, the anode material needs to be cooled. Before clashing on the target, the highly accelerated electrons are decelerated, because they experience repulsion by the electrons of the anode material. This loss of kinetic energy leads to an emission of X-rays. The resulting spectra for many electrons is called continuous X-ray spectrum or white radiation. The reason why the deceleration of electrons produces a spectra rather than a discrete line, is the distribution of velocity of the electrons and the different paths each electron can take. The intensity of the white radiation is determined by the kinetic energy of the electrons, which in turn is determined by the applied voltage between the electrodes. However, the deceleration is not the only observable phenomena. A second kind of radiation, a discrete part can also be observed. This radiation is called "characteristic radiation" and it is characteristic for each anode material [36]. These discrete

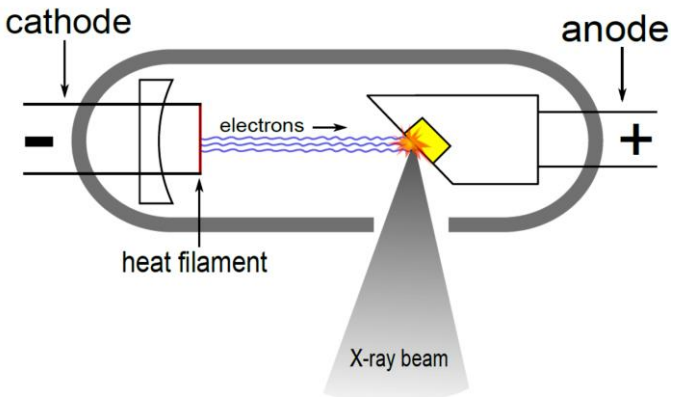

Figure 31 Schematic of an X-ray tube for the production of characteristic X-ray radiation

lines are superimposed upon the white radiation and are caused by a different mechanism. If the kinetic energy of an electron is high enough to excite a core-shell electron of an atom of the anode material, an electron hole will be created, which is filled by an electron from an outer shell. This process is a so called relaxation process. Since the state in a near-shell orbital is more favourable than the state in an outer shell, the relaxing electron has to loose energy in order to reach a lower ground state. This loss in energy is facilitated by emitting an X-ray photon with energy equal to the difference in energy between the two orbital energies. This energy difference is a discrete value depending only on the involved shells. The shell of the excited electron and the shell of the electron, which fills the resulting hole, are defining the nomenclature of these discrete lines (Fig. 33).

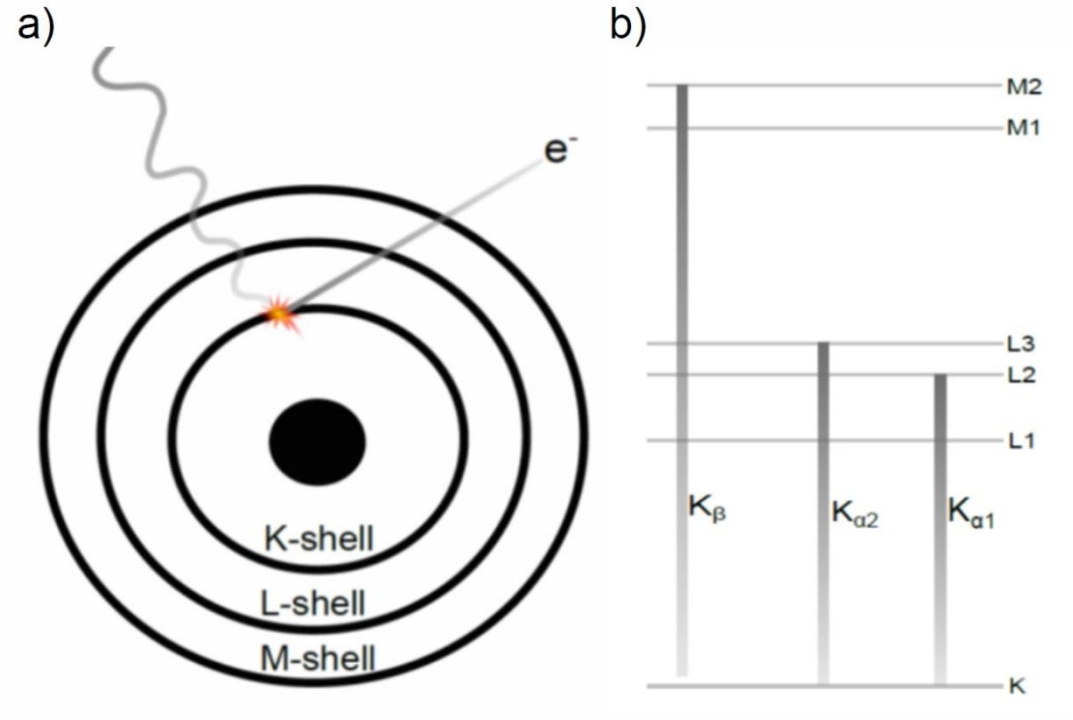

Figure 32 a) Dislodged electron from a K-shell by absorbing the kinetic energy of an incoming electron b) Relaxation after emitting a near-core electron by filling the hole with an outer shell electron

The first letter defines the shell of the dislodged electron, while the Greek latter stands for the "filling" electron with a number in respect to the angular momentum of the orbital. As already illustrated in Figure 32, the relaxation process is restricted to certain quantum numbers. If Δn is the change in principal quantum number, Δl is the change in the "orbital-shape" quantum number and Δj is the change in the total angular momentum quantum number, following selection rules can be found:

$$\Delta n = \text{anything};\ \Delta l = \pm 1;\ \Delta j = 0 \text{ or } \pm 1$$

For example, the transition from L1 to K is forbidden because here Δl would be 0.[37]

4.3.2. X-Ray diffraction

X-rays are electromagnetic waves, which can be scattered by atoms. If a beam of X-rays hit an electron of an atom it will oscillate about its rest position, emitting an X-ray-photon of same wavelength in a random direction. If the energy between incident and emitted photon is 0, the process is called “elastic scattering”.

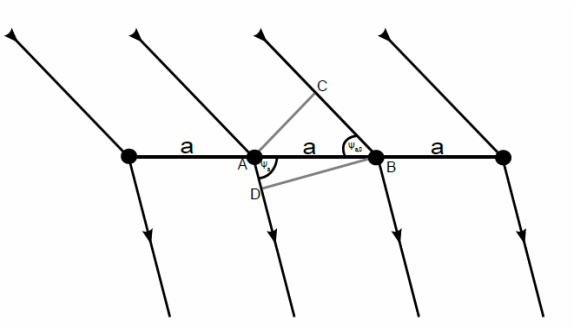

Figure 33 Path difference of two diffracted X-rays [37]

The situation changes if not a single atom, but a beam of X-rays illuminates a line of atoms. The elastically scattered, or diffracted, X-rays interfere with each other. Constructive and destructive interference result in a scattered composite wave front. The rule for constructive interference can be derived from Figure33.

Constructive interference is only possible if the path difference between the distances $\overrightarrow{CB}$ and $\overrightarrow{AD}$ is an integer (n) of the incoming X-ray wavelength (λ). Therefore:

$$\overrightarrow{CB} - \overrightarrow{AD} = n\lambda \qquad (19)$$

This can also be written as:

$$a\left(cos\psi_a - cos\psi_{a,0}\right) = n\lambda \qquad (20)$$

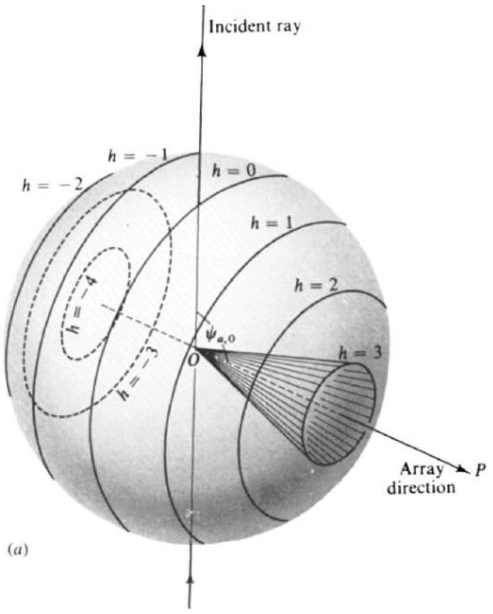

Figure 34 Diffraction cones of increasing order in h [36]

Before scattering, the X-rays are not necessarily co-planar so that for a fixed angle $\psi_{a,0}$ and a fixed integer n, the permitted diffraction angle ψ_a forms a cone, where its axis are the aligned atoms. The permitted cones and their respective integer are shown in Figure 34. This concept can be extended from aligned atoms to a three dimensional crystal. Equation 33 is a solution for only one dimension. Extending the concept will lead to the so-called Laue-conditions or Laue-equations.

$$a\left(cos\psi_a - cos\psi_{a,0}\right) = h\lambda \qquad (21)$$

$$b\left(cos\psi_b - cos\psi_{b,0}\right) = k\lambda \qquad (22)$$

$$c\left(cos\psi_c - cos\psi_{c,0}\right) = l\lambda \qquad (23)$$

The integers h,k and l correspond to the miller indices, which will be explained in chapter 4.3.3. . The three equations correspond to the three axis of a crystal and each equation describes a different diffraction cone. The conditions for constructive interference states, that constructive interference can only occur when all three cones intersect (Fig. 35). W.L Bragg found a much easier approach in 1913. Bragg stated that instead of being scattered by single atoms, X-rays could be reflected by a set of planes, which passes through all the scattering atoms and are equally spaced. The planes are defined by the miller indices and represent the integers h,k and l of the Laue-equations. This approach resulted in the equation:

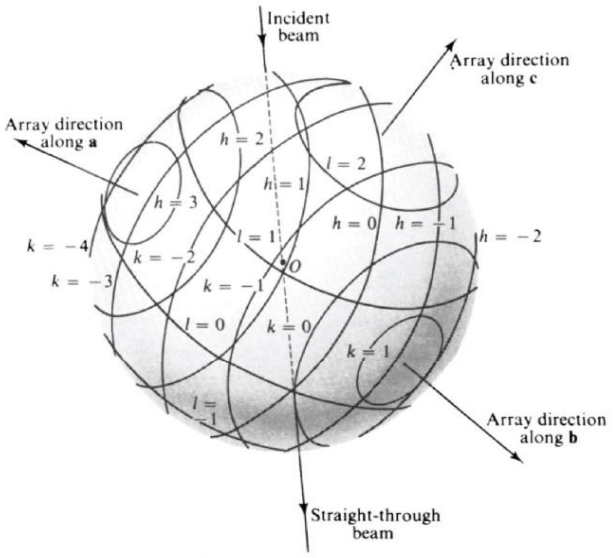

Figure 35 Diffraction cones resulting from the Laue-equation along the three basic axis a,b and c [36]

$$2d_{hkl}sin\theta = n\lambda \qquad (24)$$

The distance between the equally spaced planes is given by d_{hkl}. Reflection for a defined set of planes, with a fixed interplanar distance, can only occur at a certain angle θ.[37]

4.3.3. Miller Indices

Miller indices are used to describe different crystal planes in a unit cell of a crystal. As an example, the notation of a plane in a cubic unit cell in 4 steps will be shown.

1) List the points where the plane intercepts with the axes a,b and c.
2) Take the reciprocal of these interceptions. For example if the plane goes through ½ of an axis, its reciprocal will be 2. If the plane never intersects the Miller indices will be zero.
3) The resulting miller indices for all axes are written in parentheses. Pay attention to the ordering of the indices in the brackets. For a orthorhombic system the order will be (abc).

Nevertheless, since the Bragg equation has no information about the unit cell other than the spacing of the planes, there has to be a correlation between this spacing and the unit cell

parameters (a, b, c, α, β, γ). For a two-dimensional unit cell the relation, shown in Figure 36 can be constructed (note that a/h is the intercept of the plane h with the axis a):

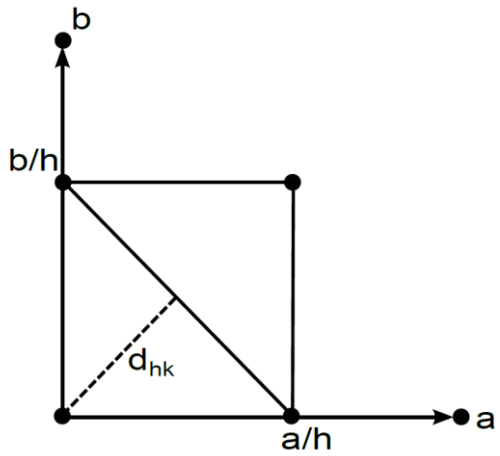

Figure 366 Relationship between the spacing (d_{hk}) between two planes and the crystallographic axis

Extending this concept to a three dimensional cubic unit cell, allows for a calculation of the unit cell parameters by:

$$\frac{1}{d^2} = \frac{h^2+k^2+l^2}{a^2} \quad (25)$$

If d is known, the lattice parameter of the unit cell can be calculated. Further information about the Bravais lattice of the unit cell can be obtained by the appearance or missing of certain planes. For example if a unit cell is cubic-body-centred all reflections with h+k+l=odd will vanish.[38]

4.3.4. Atomic Scattering factor

As mentioned in section 4.3.1., X-rays cause an electron of an atom to oscillate. During relaxation, the atom emits an X-ray of same wavelength (elastic scattering). While hydrogen has only one electron, all other atoms have more electrons, which can scatter the incoming X-rays. This can lead to interference between two X-rays, which are scattered by the same atom but different electrons, since their phase will be different. This interference depends on the phase difference between scattered and incoming X-rays.(Fig. 37). The scattering factor f is defined by:

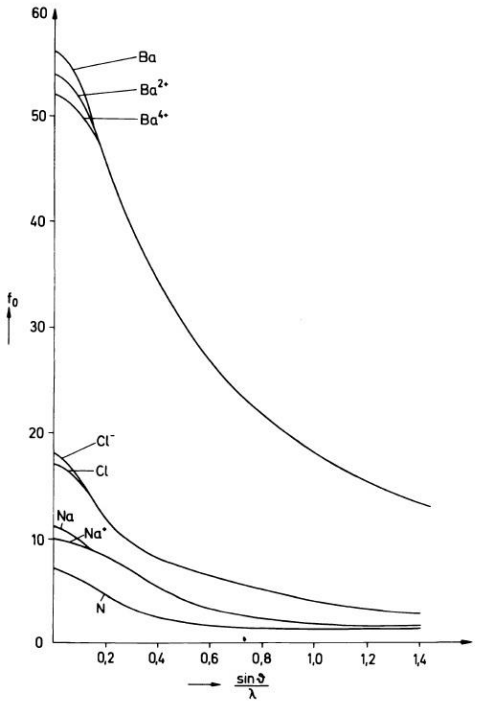

Figure 37 Atom-Scattering F actor for different atoms and their ionic states [38].

$$f = \frac{amplitude\ of\ the\ wave\ scattered\ by\ an\ atom}{amplitude\ of\ the\ wave\ scattered\ by\ one\ electron} \quad (26)$$

In Figure 37 f(z) is plotted against $sin\theta/\lambda$. The scattering factor is a function of the atomic number, the reflection or scattering angle θ and the wavelength of the incident X-ray

radiation. If the reflection angle becomes zero, the scattering amplitude is normally equal to z. [39]

4.3.5. Structure Factor

While the scattering factor describes only one atom, a crystal is composed of many atoms, which are periodically arranged. This periodicity is limiting the scattering to certain directions as mentioned in the chapter 4.3.2. . As its name is already suggesting, the structure factor describes the effect of a crystal structure on the incoming X-ray beam. The equation for the structure factor (F) is:

$$F_{hkl} = \sum_i \ f_i e^{2\pi i(hx_i + ky_i lz_i)} \tag{27}$$

Here x_i, y_i and z_i are the coordinates of an atom in the unit cell and h, k and l are the Miller indices of a reflection plane. A drawback of this formula is, that a diffraction pattern doesn`t yield directly the structure factor but the squared structure factor (F^2). The measured intensities (I) are therefore related by:

$$F^2 \propto I \tag{28}$$

Equation 40 shows that the structure factor is a complex quantity which includes amplitudes and phases of scattered waves. The information about the phase of the scattered waves is lost when the structure factor is squared. This problem is the so-called “phase problem”. After a measurement, the phase angles have to be attributed to the resulting intensities using different mathematical approaches like Patterson analysis or direct methods [40].

4.3.6. X-ray Powder Diffraction

For crystal structure determination of a single crystal “single-crystal-diffraction” is used, but for phase identification in a mixture of more than one phase, it makes sense that not a single crystal is taken and measured but a powder of this mixture. In a powder, all crystals of different phases are randomly oriented. This statistical distribution of crystal orientations is the main condition for this type of analysis. The powder is exposed to a monochromatic X-ray beam and a diffraction pattern is measured. If the crystals are randomly distributed, a few will always fulfil the Bragg condition and reflection will occur. The reason why this technique is not used for crystal-structure-determination is the possible overlapping of coincidences. In a single-crystal-diffraction-diagram point signals can be detected which will become circles in a powder-diffraction-diagram. This loss of information is making a

determination of an unsolved crystal structure more difficult. Additionally the background of powder diffraction is higher than the background of a single crystal diffraction pattern, due to the random orientation of the crystals and the existence of more than one phase. Nevertheless, unknown structures can be compared with already known structures if no single crystal of a phase can be obtained. In most cases X-ray-diffractometer with Bragg-Brentano θ/2θ geometry are used to measure the diffraction pattern. In this work a Bruker D8 Powder-X-ray-diffractometer was used. In this type of diffractometer the X-ray source is fixed while the detector moves along the diffractometer circle. The sample holder moves with half the speed of the outer the detector. Several slits are used to focus the X-rays before and after they were scattered from the sample. Intensities are measured by a Silicon strip detector, which can measure 3° simultaneously at one detector position, which drastically reduces the measurement time when compared to a single point detector. The sample is usually a powder and therefore it needs to be "glued" to the sample holder. For this purpose, commercially available Vaseline is used. The sample holders are single crystalline silicon crystals, which are cut at a defined angle so that the sample holder itself shows no diffraction. [39]

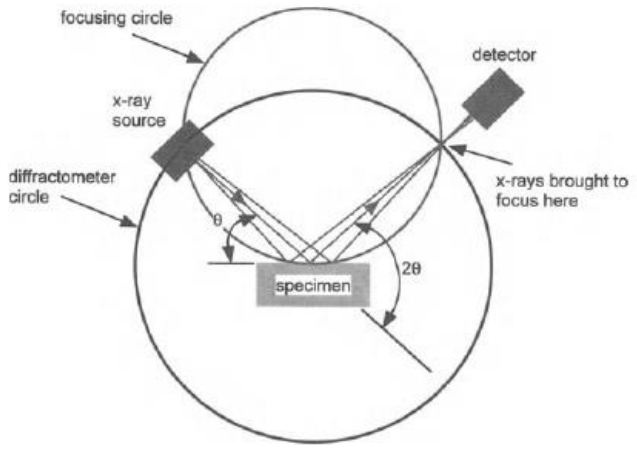

Figure 38 Schematic of a powder diffractometer in Bragg-Brentano geometry [37]

4.3.7. Rietvield Refinement

In this last chapter of X-ray-Diffraction the analysis of such a powder pattern will be discussed. The Rietvield method is a method for calculating the position of Bragg-Reflexes and their intensities of an already known structure and comparing them with the Bragg-Reflexes of a measured structure. With this method, overlapping reflexes of different structures can be separated when the Structure Modell of both structures is known. The comparison between the calculated and observed Bragg-reflexes is done by a least square fit. The variable parameters of the least square fit are the lattice parameters, atomic coordinates, thermal parameters, occupation etc. These parameters are then optimized to obtain the best "fit" or the smallest difference between calculated and observed Intensities. All these parameters are related by the following equation [35]:

$$y_{ci} = S \cdot \sum_K L_K . |F_K|^2 \cdot \Phi(2\theta_i - 2\theta_K) \cdot P_K \cdot A \cdot S_R \cdot E + y_{bi} \quad (29)$$

The calculated Intensities y_{ci} at the angle Θ are compared to the observed intensities y_{bi}. In order to see if a fit is "good" two different values are calculated together with y_{ci}. The R-Bragg (R_B) value is the major criteria for the fit of a single phase, while the weighted profile R_{wp} describes the fit of the whole profile. All standard programmes for Rietvield refinement have both values in their output.

K….Miller indicies for a certain reflex
S….scaling factor
L_K..Includes Lorentz,Multiplicity and Polarisation factors
F_K..Structurefactor for Reflex K
Φ..Profil Function shape (Lorenzian or Gauss or physical model)
P_K..factor for preferred orientation
A…Absorbtion factor
S_K…Roughness of the crystal surface
E..Extinction coefficient
y_{bi}..background at point i

$$R_B = \frac{\sum_i |I_{obs,i} - I_{calc,i}|}{\sum_i I_{obs,i}} \quad (30)$$

$$R_{wp} = \sqrt{\frac{\sum_i w_i (y_{obs,i} - y_{calc,i})^2}{\sum_i w_i (y_{obs,i})^2}} \quad (31)$$

$I_{calc,i}$ are the integrated Intensities of the reflex i. The measured intensities are fragmented according to their fractions. $Y_{obs,i}$ and $y_{calc,i}$ are the observed and calculated intensities at the point i. Therefore the Bragg-R-value R_B is based on the integrated Intensities of the structure model while the Bragg-R_{wp}-value is based on the actual Intensities.

Additionally site occupation, crystal domain size and the temperature factor can be refined. Refining the crystal domain size to smaller values results in a broadening of the peaks. If measured peak intensities of a phase are smaller than the calculated peak intensities of the model then the investigated crystal can be assumed to have several vacancies. Vacancies are sites, which are normally occupied by atoms but are now empty. This missing of atoms leads to a smaller electron density which results in a smaller intensity of the diffraction peaks. The occupation factor corrects these vacancies. The temperature factor or "Debye-Waller factor" corrects the thermal motion of atoms. Atoms in a crystal are not located at fixed points but oscillate about their mean position. This oscillation leads to a reduced in electron density and therefore also a reduced intensity. The Debye-Waller factor is I function of sinθ, $f_0(z)$ and λ as shown if equation 32.

$$f = f_0 e^{\left(\frac{-B \sin^2 \theta}{\theta}\right)} \quad (32)$$

f_0…..atomic scattering factor

f…..corrected atomic scattering factor

B…..temperature factor

The temperature factor B is responsible for an additional attenuation of the atomic scattering factor (Fig. 36).

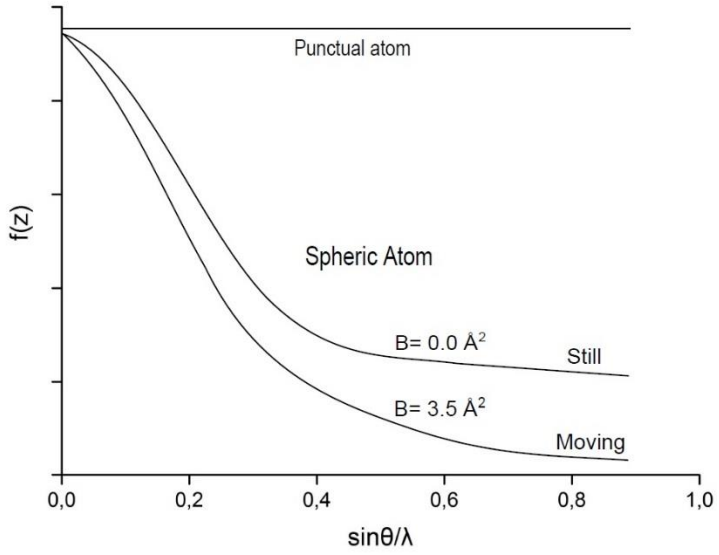

Figure 39 Atomic scattering factor for different temperature factor values (B)

4.4. Atomic-Force-Microscopy

Atomic force microscopy (AFM) is a technique for measuring the surface structure of a sample with high resolution and accuracy. The difference to other microscopes is that AFM does not need to focus a light or electron beam on a sample to create an image. The working technique of AFM can be compared to a blind man reading braille. A tip scans over a sample and registers height and topography (Fig. 40). In most cases the tip which scans over the sample is fixed while the sample is mounted on a "stage" which is moved. The high resolution of an AFM is the product of three important instrumentations. The first are the "Piecoelectric transducers". Piezoelectric materials are used to move the tip as well as the x-y stage on which the sample is mounted. These materials have a known expansion coefficient, which allows for a precise movement of the tip or the sample by applying a small voltage to the material. Typical piezoelectric materials expand with ~1nm per applied volt. The second instrumentation is the "Feedback control". Setting a constant force value between sample and tip allows for a constant tip-sample distance. If the distance changes the force changes too and the sample will be moved away from the tip, until a set force value is reached. Since the main criterion is the force between sample and tip, the third instrumentation is the so-called "Force transducer". These transducers measure the force between sample and tip and usually consist of a cantilever with integrated tip and an optical lever. A laser beam is reflected by the cantilever and registered by a detector, most commonly a four-segment photo detector. If the cantilever is deflected or attracted by the surface, because the force between sample and tip changes, the change in the position of the laser beam is registered

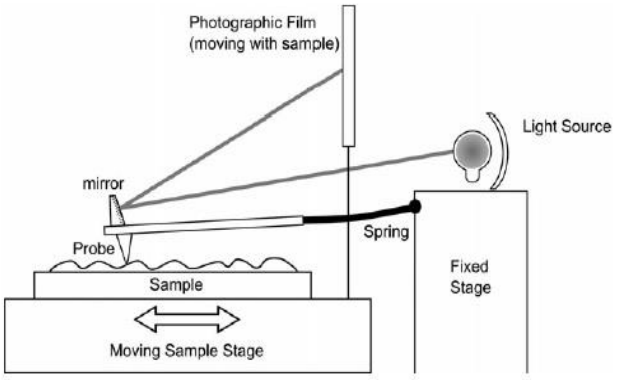

Figure 40 Simplified schematic of an AFM set-up [41]

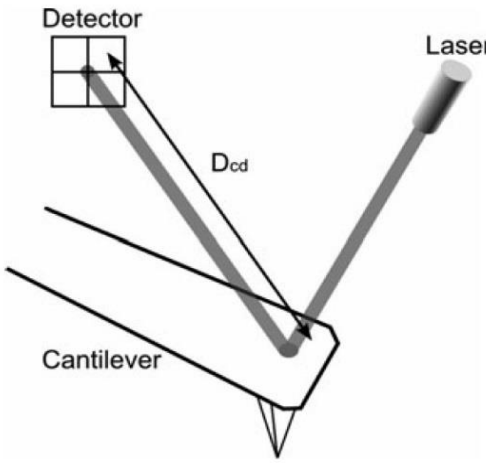

Figure 41 Detection of the cantilever position via the position of a laser spot on a photodiode [41]

by the detector (Fig. 41). [41] The resolution of an image is not only determined by the accuracy in x-y-z position but also by the tip geometry. Measuring the same sample with a dull and a sharp tip can lead to two very different results (Fig. 42).

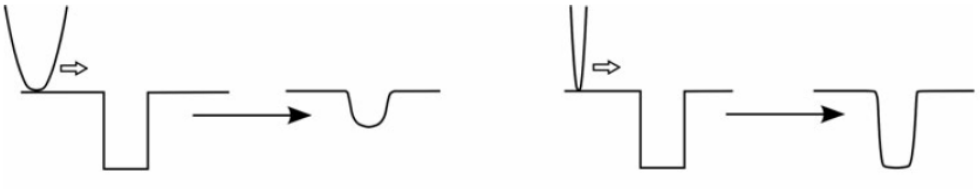

Figure 42 Signal differences of a sharp and dull AFM-tip [41]

The AFM can be operated in three different modes. The modes are contact, non-contact and tapping mode. These three modes are classified by their respective force-distance curves (Fig. 43). In contact-mode the tip is in constant "contact" with the sample surface. This mode has the disadvantage that the tip can easily be damaged by the sample or vice versa but the measurement can be done on air or even in liquid. The second mode is the tapping-mode. The tip is oscillated with its resonance frequency so that the tip just briefly touches the sample. Working in tapping-mode is friendlier for the sample since no friction can occur, but the resolution is drastically reduced compared to the contact-mode. The last mode is the non-contact mode. It is special form of the tapping mode, but the tip is resonated with a much lower amplitude. The tip is brought close to the sample surface, but stopped before reaching the zone of repulsive interaction. For this mode, a stiff cantilever is needed which is able to measure small dynamic effects by measuring small changes in the oscillation. Changes in the attractive force between tip and sample will result changes of the resonance frequency of the cantilever, which can be detected and converted into a height value. The AFM images in this work were all recorded using contact mode.[42]

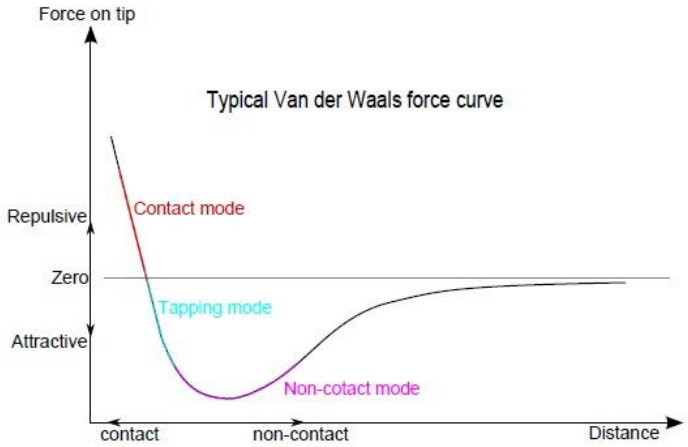

Figure 43 Force-distance curve between sample and tip with modes corresponding to their average force

4.5. Scanning Electron Microscopy (SEM) and Electron Probe Micro-Analysis (EPMA)

Scanning electron microscopy is quite similar to light optical microscopy (LOM) but instead of visible light, SEM uses an electron beam to illuminate a sample. The microscope column of a SEM consists of an electron gun, which generates electrons and accelerates them to an energy of 0.1-30keV, electron lenses for focusing the electron beam to a spot size less than 10nm, the sample holder and the detector. Unlike the light optical microscopy, the sample image is obtained by scanning over the sample point by point while in LOM the whole sample is illuminated at once. To avoid interaction of the highly accelerated electrons and with gas molecules, the electron column is kept under vacuum (10^{-6}mbar). When an electron beam illuminates the sample several interaction are possible, depending on the energy of the incoming electron beam.

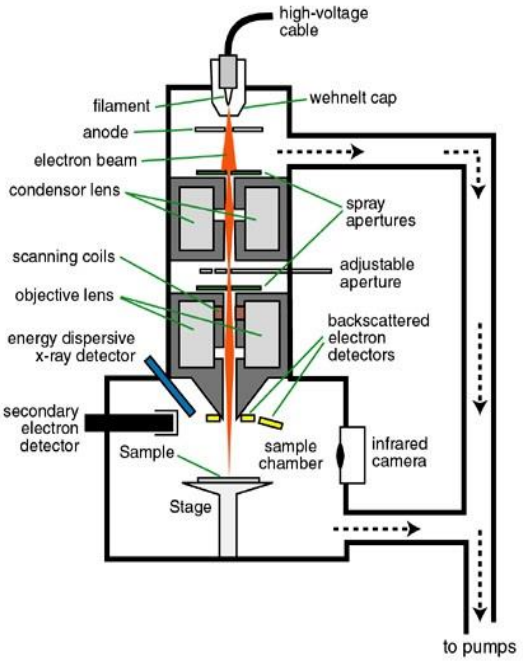

Figure 44 Schematic drawing of the electron column [43]

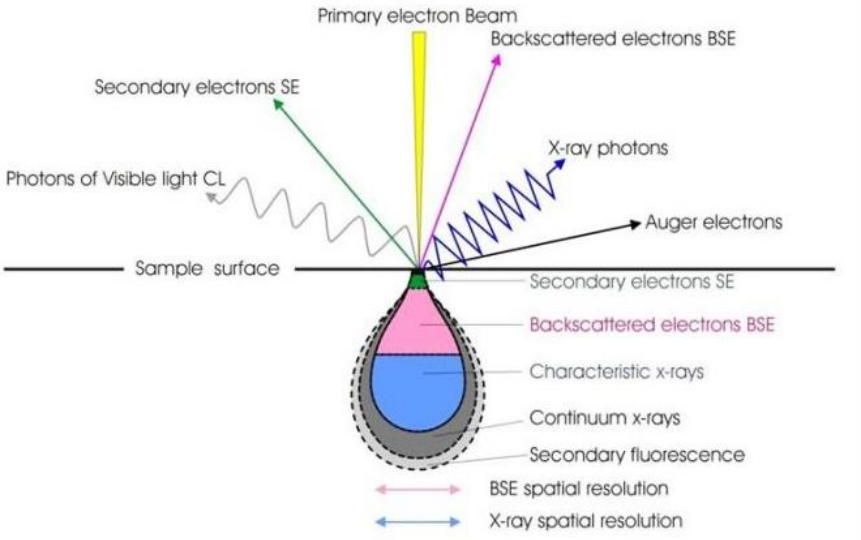

Figure 45 Possible reaction after interaction of an electron beam with a sample [44]

Backscattered electrons (BSE) are usually used for sample imaging. The primary electrons collide with the surface of the sample and are almost elastically backscattered. The backscattering probability is proportional to the atomic number (Z). The larger the atomic

number the higher the amount of backscattered electrons. These electrons yield no information about the quantity of certain elements and they are mainly used for imaging since they allow for a good contrast, if the investigated atoms have enough difference in Z. In case of BSE analysis a detector, usually a semi-conductor type detector is placed very close to the sample surface to collect the scattered electrons.

Topographic images are created by **secondary electrons (SE)**. These electrons are outer shell electrons of the sample, which received enough energy from a primary electron to be ejected from their shell. Since there can be no distinction between electrons, all electrons with an energy less than 50eV are considered to be secondary electrons. If a secondary electron, created in the bulk of the sample, reaches the surface of the sample, it has to overcome the surface potential barrier (work function). In addition, SE electrons continuously lose their energy when passing through the sample. Because of these two reasons, the probability for generating secondary electrons decreases exponentially with sample depth (only first 2nm are visible). For detection, a positively biased electrode is used to collect SE and the resulting current gives the SE signal.

Characteristic X-rays radiation is used to quantify the investigated elements. X-ray generation is described in section 4.3.1. in more detail. Note that the anode material is now the investigated sample. Detection of these lines is performed by analysing energy and intensity distribution of the X-ray signals. Either **Energy-Dispersive-Detectors (EDX)** or **Wavelength-Dispersive Detectors (WDX)** can be used. In an EDX-detector, X-ray-photons illuminate a p-i-n (p-type, intrinsic, n-type) crystal which absorbs the radiation by exciting electrons, forming electron-hole pairs. The amount of electron-hole pairs is directly proportional to the energy of the incoming X-ray. These electron-hole pairs are compensated by applying a charge pulse, which is converted into a voltage, yielding the signal for the characteristic X-ray radiation. WDX detectors use a crystal to diffract incoming X-rays from the sample into certain “channels” where they are counted. The crystal lattice and its angle determine which wavelengths can be analysed. Some detectors allow changing the analyser-crystal, so that a larger spectrum can be analysed. While the resolution and “signal to noise ratio” of the WDX detector far exceeds the resolution of the EDX detector, WDX crystals are more expensive and it might not be possible to investigate the whole sample with one crystal. [45]

4.6. Transmission-Electron-Microscopy

Transmission-electron-microscopes (TEM) were commercially available since the late 1940s and the basic components haven`t changed since then. A TEM is quite similar to a SEM, but while SEM uses scattered electrons for imaging, TEM is using transmitted electrons, which are passing through the sample. The five main compartments of a TEM set-up are, the electron gun, the illumination stage, the objective lens, where the sample is placed, the magnification/projecting system and the detector. In a TEM electrons are emitted and accelerated by the electron gun and focused, by magnetic lenses, towards the sample. Since TEM uses electrons it is operated under vacuum (down to 10^{-10}mbar) [46]. TEM is also related to X-ray analysis since both techniques are used to obtain diffraction patterns. In this mode, an electron beam illuminates a thin sample and a diffraction pattern of these electrons is recorded. Since the electron beam can be focused on a small spot up to 0.1nm, it is possible to investigate the diffraction patterns of single nano crystals. Additionally it is possible to perform energy-dispersive X-ray-spectrometry (EDS) of very small crystals yielding the chemical composition, or electron energy-loss spectrometry (EELS), where the loss in energy of the primary electrons is analysed, which can provide information about the local chemistry and structure of a micro crystal. The information in EELS spectrometry originates from core-electron or plasmon-excitations [49]. In this theoretical chapter, I will focus on the two imaging modes that were used in my experiments, the imaging

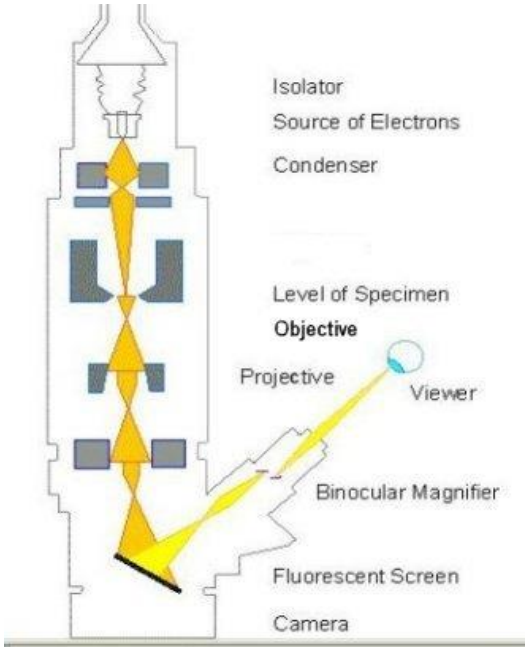

Figure 476 Set-up of a transmission electron microscope [46]

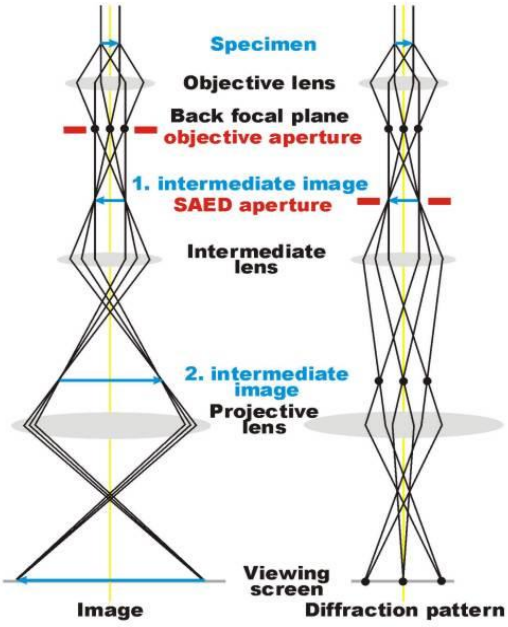

Figure 467 Imaging (left) and diffraction (right) mode in TEM [47]

mode and the diffraction mode. To understand the imaging modes it is necessary to understand the operating lenses of a TEM. After being accelerated by the electron gun, the electrons pass the condenser lens which is focuses the electron beam in the sample plane. If the sample is crystalline, two different interactions can be observed. First, some electrons will pass through the sample staying in the course of the primary beam and secondly, some electrons will be diffracted, according to Braggs law, and leave the primary beam. An objective lens in the focal plane, the plane where all beams are focused, behind the sample can block the diffracted electrons so that only the primary beam can pass through. In the imaging mode, the objective lens blocks the diffracted electron beams and enlarges the primary beam. Intermediate lenses further enlarge the image and a fluorescence screen visualizes the resulting image. When working in the diffraction mode the objective lens is removed and a sector aperture is inserted allowing only the diffracted beams to pass through. From the diffraction pattern, the point group symmetry of a crystal structure as well as lattice parameters can be obtained. For example, a hexagonal unit cell will show a 6-fold diffraction pattern if the c-axis of the unit cell lies parallel to the electron beam (Fig. 48). [49]

Figure 48 Example of an electron diffraction pattern of a hexagonal cell [49]

Most TEMs have two different electron detectors shown in Figure 47. One detector is for analogue observation (fluorescent screen in the Figure 47) while the other detector (camera) produces a digital image. In most cases the fluorescence screen is a phosphor or zinc sulphide viewing screen. Electrons, either diffracted or primary electrons, illuminate the screen by exciting outer shell electrons of the fluorescent material which will create an image by emitting “green” photons (green referring to the wavelength of those photons). This type of detector cannot be used for very high electron intensities or for focusing at one point for a longer time, because these high-energy electrons will “burn-in” and destroy the detector. The second detector for digital images is a charged-couple-device (CCD) detector. This detector consists of a p-doped silicon substrate (protected by a silicon

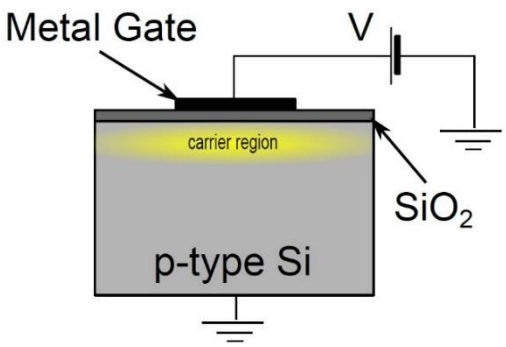

Figure 49 Schematic of a single CCD device

dioxide layer) and a metal gate. Applying a positive voltage will repel the carriers (holes in case of p-type semiconductors) creating a layer of electron-acceptors close to the oxide layer. The electrons of the diffracted or primary beam are converted into photons by illuminating a phosphor or YAG (yttrium aluminium garnet) scintillator. If photons hit the CCD-detector they will excite electrons on the surface of the CCD cell, and these electrons will travel through the silicon material to the electron hole region (carrier region) because of the difference in potential. This "filling" of the holes can be measured by reading the charge. The set-up of such a CCD-device is quite sophisticated. Imagine that each pixel of the detector is a small p-type silicon piece with its own metal gate and oxide layer. Every column and row of these pixels has its own potential well so that the pixels are separated in x and y direction by different potential wells. This allows for a progressively reading of a single column as illustrated in Figure 50. The arrays are shifted until all cells have been read out. [51]

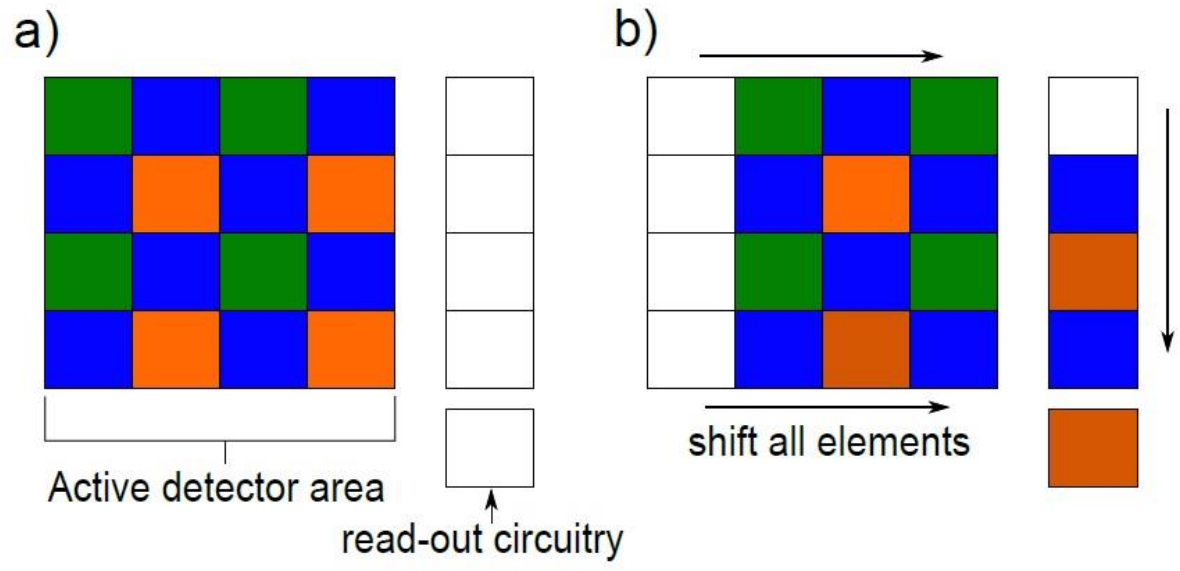

Figure 50(a) 4x4 CCD cells are exposed to a photon beam; (b) the first column is shifted towards the empty column (white) and the first "cell" is shifted vertically into the read-out circuitry.

4.7. CALPHAD (Calculation of Phase Diagrams)

About 50 years ago, Larry Kaufman and Himo Ansara started, together with other scientists, their work on calculating phase diagrams based on experimental thermodynamic data. [52] Thermodynamic data can be obtained from various experiments and a critical assessment has to be performed before calculating a phase diagram in order to exclude contradicting data. This assessment has to include not only literature review but should also include direct contact with authors, to get detailed information about different experiment conditions and experimental set-ups. What kind of data can be used in a CALPHAD calculation? CALPHAD has a wide range of possible input. Primarily scientists work with input from calorimetric methods like enthalpy, heat capacity or enthalpy of transformation. If the investigated system has a volatile component, gas phase equilibria techniques like non-isothermal isopiestic methods can be used to determine activities which can be used as a basis for thermodynamic calculations. In some cases, electromotive force measurements (EFM) are available, which can also be included. In addition to the thermodynamic quantities, experimental investigations of phase diagrams have to be included as well. This data can be divided into non-isothermal and isothermal data. Non-isothermal data includes data obtained from thermal analysis, chemical potential measurements, magnetic susceptibility measurements etc. Isothermal Data, which is the majority of data, is obtained from metallography, X-ray analysis and diffusion couples measurements [53]. CALPHAD calculations are based on a standardised description of Gibbs energy of pure components. In the first step CALPHAD is used to calculate simple binary phase diagrams, assuming enough thermodynamic data is available. This description can then be extended to more complex systems such as ternary or quaternary systems. [52]

Since the Gibbs energy of a pure substance is a function of pressure and temperature, the Gibbs energy of the elements is a function of temperature, assuming a system at standard pressure. These functions are collected in the SGTE-Database (Scientific Group Thermodata Europe). The Gibbs energy function, in terms of temperature, is described as a polynomial function as shown in equation 33.

$$ {}^{0}G_i^{\phi}(T) = a + bT + cTln(T) + \sum_i \ d_i T^n \qquad (33) $$

The coefficients a-d_i are defined for each element. Other thermodynamic variables like enthalpy, entropy and heat coefficient can be calculated by deriving equation 46. Phase

diagrams can be understood as a mixture of two or more components. Every phase is described by:

$$G_m^{\emptyset} = G_{ref}^{\emptyset} + G_{id}^{\emptyset} + G_E^{\emptyset} + G_{mag}^{\emptyset} + G_{surf}^{\emptyset} \tag{34}$$

The term $G_{ref}^{\emptyset}$ denotes the sum of the molar Gibbs energies of all elements or compounds according to their fraction. If the standard conditions are used for the description, this term is called "Standard element reference state".$G_m^{\emptyset}$ is the Gibbs energy of the pure components (also called reference state or surface of reference), $G_{mag}^{\emptyset}$is the contribution in case of magnetic ordering, G_{surf} denotes contributions due to the change in surface energy, $G_{id}^{\emptyset}$ is the contribution of ideal mixing and $G_E^{\emptyset}$ is the excess Gibbs energy for non-ideal interactions and deviations from an ideal solution behaviour. The ideal mixing, assuming that all constituents are statistically distributed can be described as:

$$G_{id}^{\emptyset} = -TS_{id}^{\emptyset} = RT\sum_i \; x_i log x_i \tag{35}$$

The non-ideal mixing describes the real state of a mixture, which includes all possible contributions to the Gibbs energy that are not expressed in equation 34. The non-ideal solutions model used by CALPHAD is the so-called "Redlich-Kister" model. For an easier understanding the solution model will be shown for a binary system. Note that i and j represent the fractions of the constituents.

$$^{bin.E}G_E^{\emptyset} = \sum_{i=1}^{n-1}\sum_{j=i+1}^{n} x_j x_i L_{ij} \qquad\qquad L_{ij} = \sum_{v=0}^{k}(x_i - x_j)^v \cdot \; ^vL_{ij} \tag{36}$$

The exponent v denotes the order of the parameter. When performing calculations, the order of the parameters should be kept as low as possible. The parameter $^vL_{ij}$ describes the temperature dependence of the interaction parameter and can be written in a form of:

$$^vL_{ij} = \; ^va_{ij} + \; ^vb_{ij}T \tag{37}$$

Usually a linear dependence is sufficient but it should only be changed if the temperature dependence of the heat-capacity of the investigated solution is known. The form of equation 37 has a very familiar form to the Gibbs energy. The parameter $^va_{ij}$ describes the excess enthalpy and $^vb_{ij}T$ the excess entropy.

The dominant model used by CALPHAD to describe solutions and non-stoichiometric phases is the "sublattice model". If a structure from the type AB has a primitive cubic body-centred

lattice, it can be divided into two sublattices with the positions (0,0,0) and (½,½,½). In a sublattice model, the atoms at these positions are allowed to mix, so that A can change position with B. When working with a sublattice model one has to include all different sublattice models in the calculations.[53]

After constructing a consistent thermodynamic database and the selection of different model parameters for each phase (in respect to the available data), CALPHAD can optimise these parameters in a least square fit and calculate the total Gibbs energy of the whole system. Minimisation in respect to a certain temperature, pressure and composition yield the equilibrium Gibbs energy, which allows for the construction of a phase diagram. The output has to be checked and compared with the input data. If the output can`t fully describe the system or contradicts the input in certain points the evaluation of input data and the thermodynamic modelling need to be revised. This procedure is repeated till the output and input data are in good agreement. Now this model can be used for predictions of different thermodynamic quantities or other simulations. This approach is sketched represented in Figure 51[54].

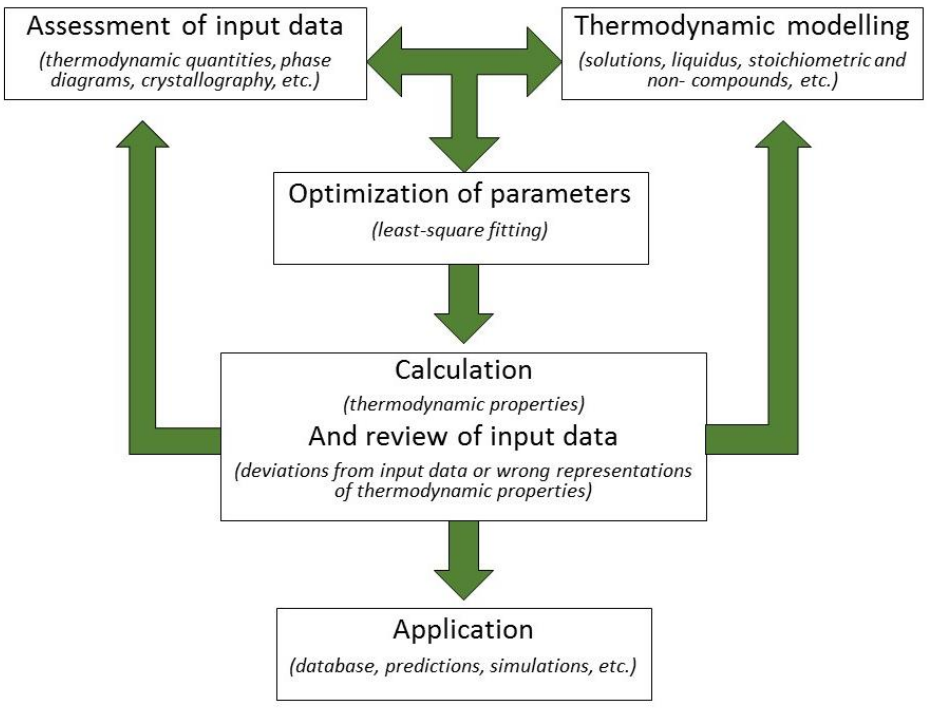

Figure 51 Schematic of the CALPHAD assessment method [55]

4.8. Catalytic testing for Methanol-Steam-Reforming

Catalysis plays a major role in our everyday lives and, the interest in catalysis has grown in the last years because of its applications in alternative energy. In this chapter, I will deal exclusively with methanol steam reforming and the method of testing catalytic activity of the samples which were produced in the course of my master thesis.

Before talking about catalysis, all possible side reactions of the methanol-steam-reforming reaction have to be considered. This is essential in order to be able to calculate the catalytic activity and selectivity. In this reaction, the selectivity is a crucial point because one of the side products is carbon monoxide. The conversion depends on the specific activity and amount of the catalyst and is therefore an intrinsic material property. Following catalytic reactions are possible[3]:

$$CH_3OH \rightarrow CO + 2H_2 \qquad \Delta H°=90 \text{ kJ/mol}$$

$$CH_3OH + H_2O \rightarrow CO_2 + 3H_2 \qquad \Delta H°=49 \text{ kJ/mol}$$

$$CO + H_2O \rightleftharpoons CO_2 + H_2 \qquad \Delta H°=-41 \text{ kJ/mol}$$

$$CO + 3H_2 \rightleftharpoons CH_4 + H_2O \qquad \Delta H°=-206 \text{ kJ/mol}$$

The methanol-steam-reforming-reaction (second reaction) seems to be the most favourable in terms of hydrogen because it has the highest hydrogen to carbon dioxide ratio. This reaction needs a 1:1 reactant ratio of methanol to water. In order to determine the catalytic activity the gases hydrogen (H_2), carbon monoxide (CO), carbon dioxide (CO_2) and methane were analysed [20].The reactor (Fig. 52) is a commercially available “plug-flow” reactor (PID Eng & Tech). The whole reactor was mounted in a box, which was heated to 120°C to avoid condensation of liquids on the reactor tubes. The reactor tube (with reactor bed) was mounted in a furnace and programmed for a certain temperature program. HPLC pumps (Gilson) and an evaporator (120°C) were used for dosing the methanol-water-mixture (Flow rates MeOH:0.0225ml/min; Water:0.01ml/min). Nitrogen (20mmol/min) was used as a transport gas and Helium (1.7mmol/min) was used as a calibration gas for the GC. The flow was directed from top to the bottom through the reactor bed. After the reactortube, the resulting mixture of educts and products was cooled to 4°C to extract unreacted water and methanol. The resulting gas was filtered by a Nafion-membrane before reaching a micro gas chromatograph (Varian) for a quantitative analysis of the gas components. The chromatograph was calibrated for He, N_2, CO, CO_2, CH_4, O_2 and H_2. The amount of unreacted

educts could not be analysed and therefore it was not possible to determine the yield directly. Helium was used as an internal standard and because of its inertness; the helium flow was independent of the reaction. Analysing the helium concentration allowed for a determination of the amount of hydrogen after the reaction. Comparing the experimentally found and calculated (at 100% conversion) hydrogen flow allowed for a determination of the real conversion (equ. 38)

$$C = \frac{V(H_{2\,prod})}{V(H_{2\,theo})} \tag{38}$$

The CO_2-Selectivity was calculated by the following equation:

$$S = \frac{V(CO_2)}{V(CO)+V(CO_2)+V(CH_4)} \tag{39}$$

The CO-Fraction in the product mixture can be calculated by:

$$G = \frac{V(CO)}{V(CO)+V(CO_2)+V(CH_4)+V(H_2)} \tag{40}$$

To compare the investigated catalytic material to other catalysts, the activity in terms of produced hydrogen per used amount of catalytic material per time, was calculated. The equation is:

$$A = \frac{n(H_2)}{m_{catalytic\ material} \cdot t} \tag{41}$$

If a material shows a catalytic activity in a certain reaction but the active sites are still unknown, the activity will be calculated for the amount of the used noble metal rather than the whole catalytic material.

The ratio between the concentrations of CO_x and H_2 allowed determining which reaction was taking place. A ratio of CO_x and H_2 of 1:3 is characteristic for the methanol-steam-reforming reaction (assuming a high CO_2 concentration in CO_x). If the ratio of CO_x and H_2 would be 1:2 the observed reaction would be the methanol decomposition (if the CO concentration is high in CO_x). The catalytic activity was measured in a stepped temperature program to see if a direct correlation between temperature, conversion and CO_2 selectivity exists. The last temperature step was a 4 hours long isothermal step to observe if the catalysts showed deactivation of after a long exposure time. [20]

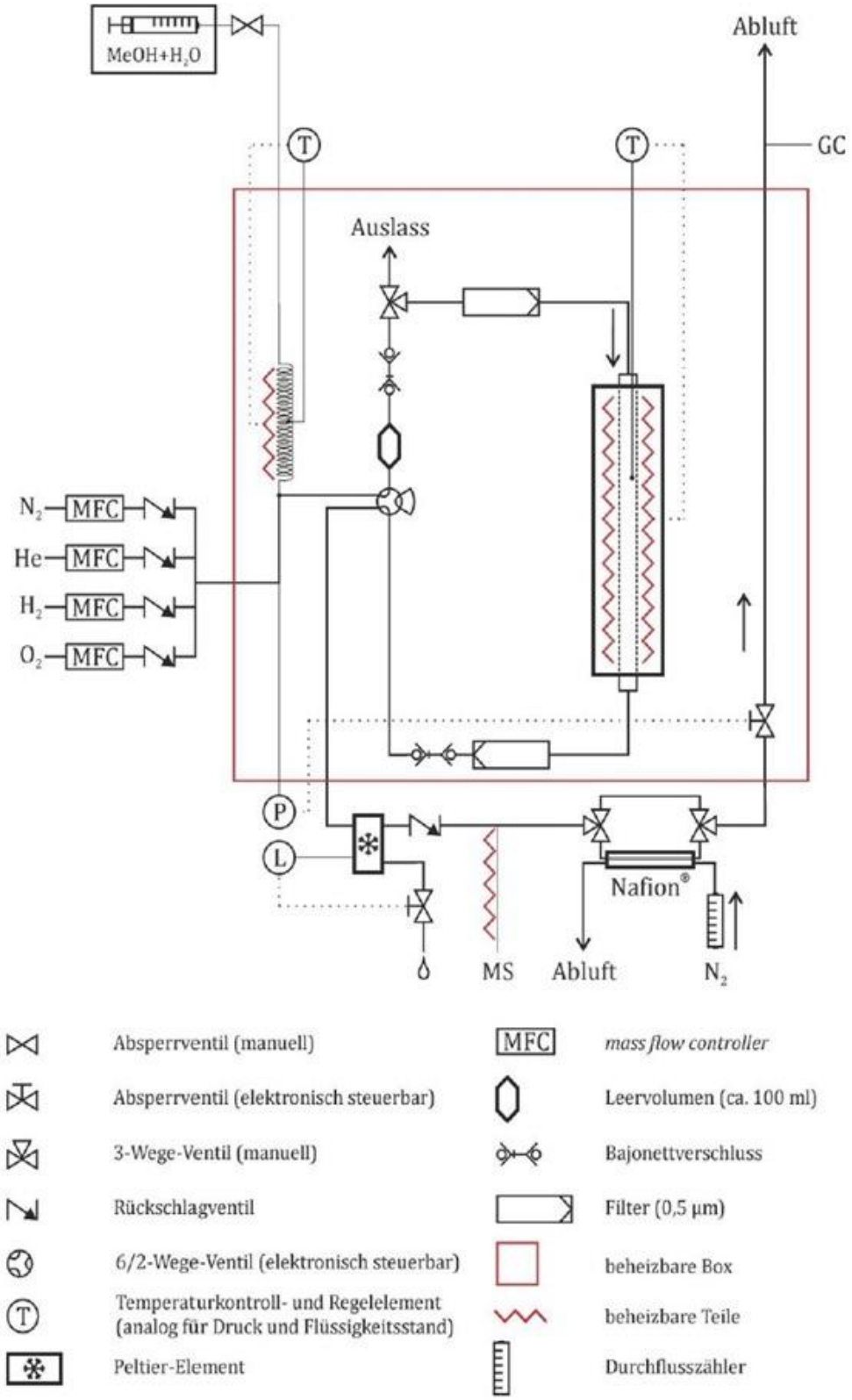

Figure 52 Schematic of a flow through reactor with additional custom modifications. No MS was used in this work and instead of spray pumps, HPLC pumps were used.[20]

5. Results and Discussion

5.1. CALPHAD preliminary reassessment

Latest literature [20] suggested a change in the melting point of the PdZn (1:1) phase and that the cubic β-phase might not be stable at higher temperatures as suggested by Köster and Zwicker. The phase diagram published by Friedrich showed a clear separation of the related β- and β_1-phase by the high-melting δ-phase. Based on this new data, a reassessment of the palladium-zinc phase diagram was performed. The phase diagram of this reassessment is shown in Figure 11. The purpose of the present work was to extrapolate thermodynamic properties of the system at low temperatures and use this data to synthesize supported $PdZn/Al_2O_3$ nanoparticles by using a modified "pseudo-isopiestic" method as described in section 4.2.2. .

In the first step of the reassessment, the system palladium zinc was calculated via the CALPHAD method. This calculation was based on the already existing model published by Vizdal et al [18]. Since the SGTE unary database, for the description of the elements, was not drastically changed in the recent years, the database from Vizdal et al could be directly adapted for further calculations. The resulting phase diagram obtained from the database provided by Vizdal et al is shown in Figure 53.

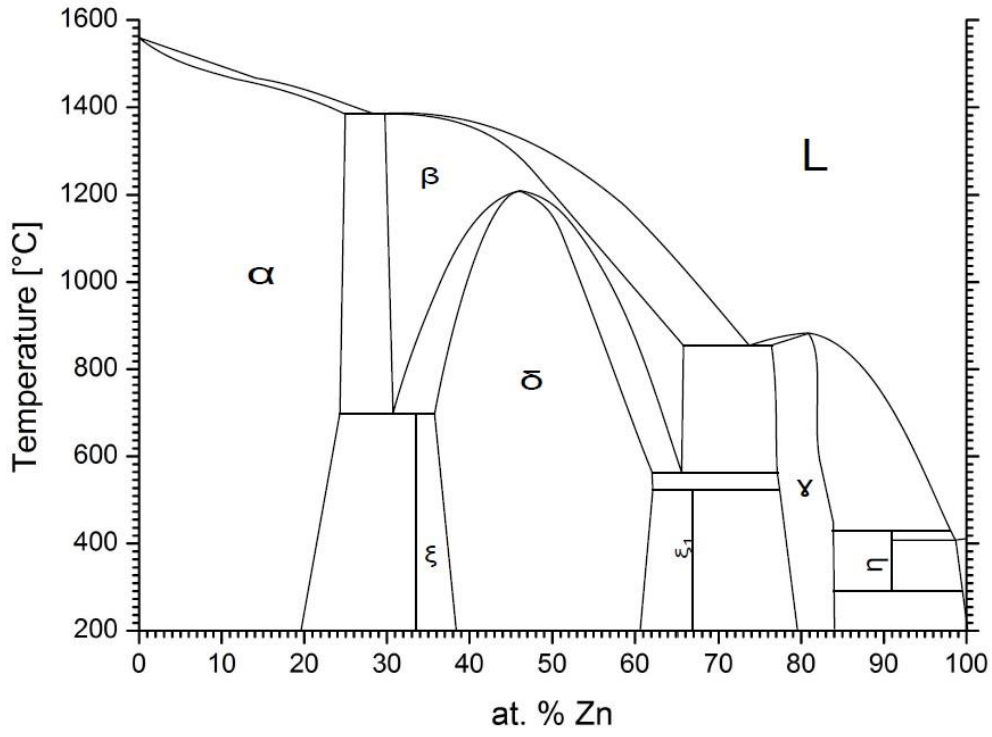

Figure 53 Assessed phase diagram of the Pd-Zn system provided by Vizdal [16]

Vizdal et al [18] described the γ-phase as a single component instead of two inter-growing γ-brass type structures as published by Gourdon et al [14-16] and Armbrüster [13]. In a first step, the γ_1-phase was added and the phase boundaries of the γ- and γ_1-phase were adjusted according to Gourdon. The decomposition of the η-phase at 300°C is not supported by any literature. Vizdal prepared samples at 97 at. % zinc and annealed them at 300°C and 400°C. Since 300°C was the lowest annealing temperature, all reactions and phase boundaries in this region below 300°C were extrapolations and were not supported by any literature. In this work, the η-phase was assumed to be stable from room temperature to 418°C.

The stability of the δ-phase at higher temperatures was changed, according to Friedrich [20], from 1220°C to 1460°C. This stabilization lead to a separation of the closely related β- and β_1 phases. Adjusting the narrow binary phase fields between δ and β or β_1 was not possible if β and β_1 were modelled as a seperate phase. The thermodynamic modelling required the introduction of β_1 as a single phase. This approach was further supported by personal correspondence by with Dennis Ivarsson [55] who was investigating the phase diagram at that time and suggested that the structures of β and β_1 might not be completely identical after long term annealing experiments. Adjusting the melting point of β required a change of the model parameters of the liquid phase, in order to reproduce the eutectic decomposition of liquid into δ and β. Since no experimental data of the liquid were available, Vizdal et al used an arbitrary thermodynamic function, which was fitted to their phase diagram. Therefore, changing the model parameters of the liquid in this work was justified. Changing the liquid requires and adjustment of all phases, which are in equilibrium with the liquid. The parameters of the liquid were changed in respect to the eutectic at 26 at. % Zn, in respect to the phase boundary between liquid and alpha-palladium and the eutectic at 75 at. % Zn where the liquid decomposes to β_1 and γ. The ξ phase was remodelled as a compound with a decrease in zinc and increase in palladium solubility above 600°C instead of being a simple line component, according to Nowotny et al [7]. While the peritectoid transformation temperature of $\alpha+\beta\rightarrow\xi$ (Pd_2Zn) was in good agreement with the literature, the eutectoid decomposition of $\beta\rightarrow\delta+\xi$ needed to be adjusted from 720°C to 600°C. Nowotny et al [7] reported the melting point of the ξ-phase to be between 550°C and 650°C. In this work the average of these two values, 600°C, was chosen as a “true” value. Increasing the stability of β to lower temperatures was only possible while simultaneously changing the solubility of

the ξ-phase towards palladium. Calculating the binary phase field between δ and β_1, in respect to the experimentally determined activities of zinc , was problematic due to the large scattering of experimental activities at the stoichiometric composition, shown in Table 2 [10]. This scattering is due to the very steep slope of a_{zn} at this composition.

Table 2 Excerpts of activities of zinc in δ-PdZn at different Temperatures. Standard states are Pd(s) and Zn(l)

No.	At. % Zn	Phase	Ts [K]	$\ln a_{Zn,Tr}$	$a_{Zn,Tr}$
Run5		Tr= 655 K	26 days		
3	50.06	β_1	808	-4.27	0.01398178
4	49.99	β_1	858	-5.3	0.00499159
5	49.98	β_1	889	-5.88	0.00279479
Run3		Tr= 679 K	26 days		
2	50.17	β_1	801	-3.27	0.03800643
3	50.16	β_1	841	-4.12	0.01624451
4	49.98	β_1	912	-5.44	0.00433948
5	49.95	β_1	953	-6.11	0.00222055
Run4		Tr= 701 K	26 days		
3	50.09	β_1	839	-3.38	0.03404745
4	50.08	β_1	886	-4.28	0.01384266
5	49.98	β_1	924	-4.94	0.0071546
6	49.89	β_1	963	-5.56	0.00384878
Run2		Tr= 735 K	26 days		
8	50.08	β_1	943	-4.29	0.01370493
9	50.05	β_1	966	-4.65	0.0095616
10	50.07	β_1	987	-4.96	0.00701293
11	50.01	β_1	1010	-5.29	0.00504176
12	50.03	β_1	1029	-5.55	0.00388746
13	49.99	β_1	1048	-5.79	0.00305798

Table 2 showed that on changing the composition within of 0.07 atomic percent, the activity changed one order of magnitude. According to the phase diagram published by Friedrich [20], even samples with more than 50 at. % at the given temperatures zinc should still lie inside the β-phase.

Values of almost identical composition and temperature were averaged and used to optimize the phase boundary between δ and β_1. Figure 54 shows a plot of activity against composition at a temperature of 1000°C.

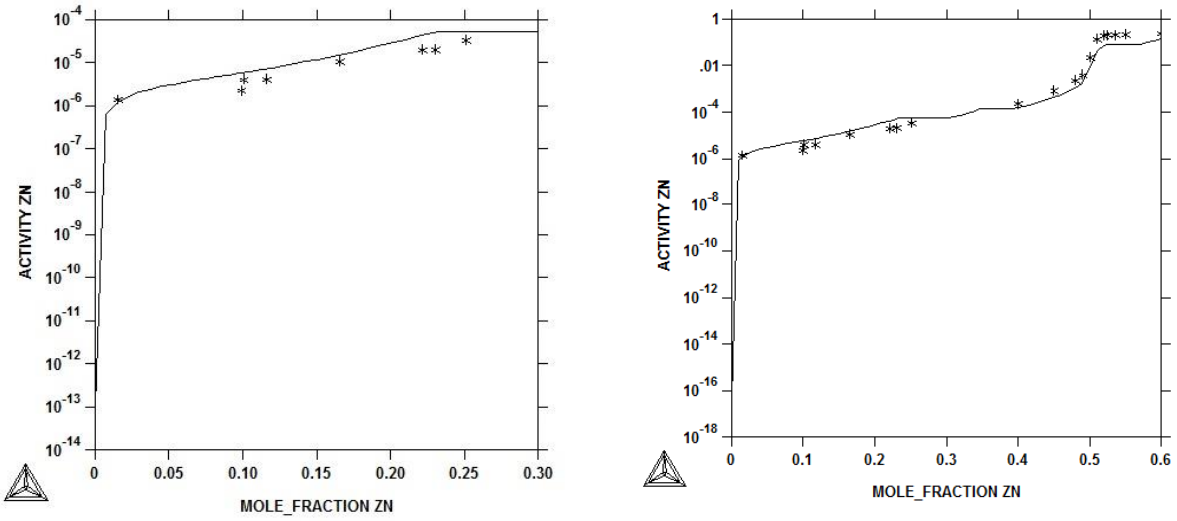

Figure 54 Measured activities (points) and calculated activities (line) at 1000°C at a composition range from 0-30at. % zinc (left) and 0-60 at. % zinc (right)

The activities, used to optimize the δ-phase and its interaction parameters are shown in Figure 55. In this work, it was decided to choose the activities of smaller magnitude for the optimisation since the existing model did not allow for such a steep slope in a_{Zn}. Modelling this steep slope would have required a different description of the whole system. Although the calculated activities didn`t completely correspond to the measured activities, they were close enough to consider the optimisation of the phase boundary as finished. The reason for the special interest in the two-phase field of δ-PdZn and ξ-$PdZn_2$ was the application of the extrapolated activities of this two-phase field for a synthesis of supported palladium zinc nanoparticles with an exact composition.

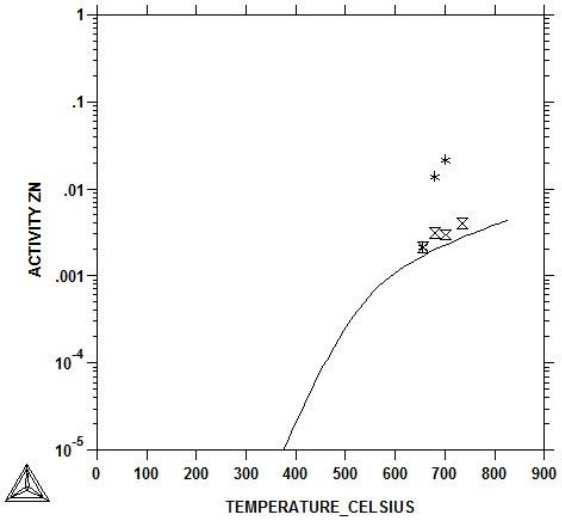

Figure 55 Measured activities (points) of upper (∗) and lower (⧖) limit at different temperatures (points) and calculated activites (line) at a composition of 49.99 at. % Zn in the phase-field δ-PdZn

The resulting calculated phase diagram and experimental points are shown in Figure 56.

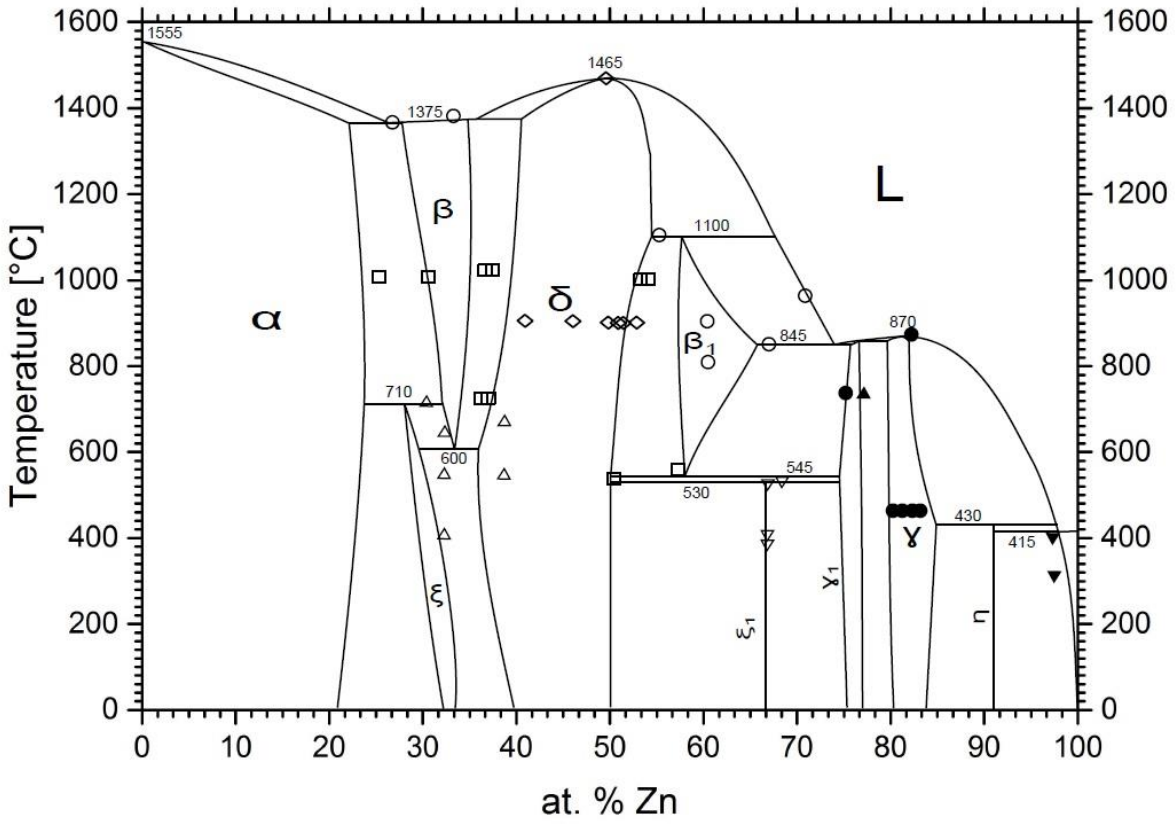

Figure 56 Calculated phase diagram via CALPHAD method and experimental data points.

The points in this calculated phase diagram are data from following literature: △ Nowotny [7]; □ Chiang [10]; ○ Köster and Zwicker [8]; ◇ Friedrich [20]; ▽ Alasafi [12]; ● Armbrüster [17]; ▲ Gourdon [14-16]; ▼ Vizdal [18].

Table 3 Summary of the thermodynamic parameters in the Pd-Zn system

Phase and Model	Model parameters (j/mol)	Reference
Liquid: (Pd,Zn)	${}^{0}L^{Liq}_{Pd,Zn} = -181731.731 + 24465T$	
	${}^{1}L^{Liq}_{Pd,Zn} = 36050$	
	${}^{2}L^{Liq}_{Pd,Zn} = -5000 + 15T$	
FCC_A1	${}^{0}L^{FCC\_A1}_{Pd,Zn:Va} = -205608 + 39.755T$	[Vizdal]
	${}^{1}L^{FCC\_A1}_{Pd,Zn:Va} = 5544.5 + 3.5\mathrm{T}$	
	${}^{2}L^{FCC\_A1}_{Pd,Zn:Va} = 47785.933 - 6.116\mathrm{T}$	
BCC_A2	${}^{0}L^{BCC\_A2}_{Pd,Zn:Va} = 7844.3 - 19.8T$	[Vizdal]
	${}^{1}L^{BCC\_A2}_{Pd,Zn:Va} = -58890 + 33.4$	
HCP_Zn	${}^{0}L^{HCP\_Zn}_{Pd,Zn:Va} = -171200 + 20T$	
	${}^{1}L^{HCP\_Zn}_{Pd,Zn:Va} = 32800$	
HCP_A3	${}^{0}L^{HCP\_A3}_{Pd,Zn:Va} = 171200 + 20T$	[Vizdal]
	${}^{1}L^{HCP\_A3}_{Pd,Zn:Va} = 50000$	
γ-$Pd_{82}Zn_{18}$	$(Pd,Zn)_{82}(Pd,Zn)_{18}$	
	${}^{0}G^{\gamma}_{Pd:Pd} = .18\ GHSERPD + .82\ GHSERPD + 25000$	
	${}^{0}G^{\gamma}_{Pd:Zn} = .18\ GHSERPD + .82 GHSERZN - 40404 + 6.65T$	
	${}^{0}G^{\gamma}_{Zn:Pd} = .82\ GHSERZN + .18 GHSERPD$	
	${}^{0}G^{\gamma}_{Zn:Zn} = .18\ GHSERZN + .82\ GHSERZN + 5000$	
	${}^{0}L^{\gamma}_{Pd:Pd,Zn} = -142000 + 30T$	
	${}^{0}L^{\gamma}_{Pd,Zn:Zn} = -4836$	
	${}^{1}L^{\gamma}_{Pd,Zn:Zn} = -4000 + 5T$	
γ_1-$Pd_{77}Zn_{23}$	$(Pd,Zn)_{77}(Pd,Zn)_{23}$	
	${}^{0}G^{\gamma_1}_{Pd:Pd} = .23\ GHSERPD + .77\ GHSERPD + 28000$	
	${}^{0}G^{\gamma_1}_{Pd:Zn} = .23\ GHSERPD + .77 GHSERZN - 44838 + 6.5T$	
	${}^{0}G^{\gamma_1}_{Zn:Pd} = .77\ GHSERZN + .23 GHSERPD + 10000$	
	${}^{0}G^{\gamma_1}_{Zn:Zn} = .23\ GHSERZN + .77\ GHSERZN + 2000$	
	${}^{0}L^{\gamma_1}_{Pd:Pd,Zn} = -128190 + 30T$	
β-PdZn	$(Pd,Zn)_1(Pd,Zn)_1$	
	${}^{0}G^{\beta}_{Pd:Pd} = GHSERPD + GHSERPD + 5000$	
	${}^{0}G^{\beta}_{Zn:Pd} = GHSERZN + GHSERPD - 123876.849 + 18.85T$	
	${}^{0}G^{\beta}_{Pd:Zn} = GHSERPD + GHSERZN - 123876.849 + 18.85T$	
	${}^{0}G^{\beta}_{Zn:Zn} = GHSERZN + GHSERZN + 1000$	
	${}^{0}L^{\beta}_{Pd,Zn:Pd} = -30000 - 3.03T$	
	${}^{1}L^{\beta}_{Pd,Zn:Pd} = 26000$	
	${}^{0}L^{\beta}_{Pd:Pd,Zn} = -30000 - 3.03T$	
	${}^{1}L^{\beta}_{Pd,Zn:Pd} = 26000$	
δ-PdZn	$(Pd,Zn)_1(Pd,Zn)_1$	
	${}^{0}G^{\delta}_{Pd:Pd} = GHSERPD + GHSERPD + 10000$	
	${}^{0}G^{\delta}_{Zn:Pd} = GHSERZN + GHSERPD - 125000 + 14.8T$	
	${}^{0}G^{\delta}_{Pd:Zn} = GHSERPD + GHSERZN - 125000 + 14.8T$	
	${}^{0}G^{\delta}_{Zn:Zn} = GHSERZN + GHSERZN + 1000$	
	${}^{0}L^{\delta}_{Pd:Pd,Zn} = -46300 + 19T$	
	${}^{0}L^{\delta}_{Pd,Zn:Pd} = -46300 + 19T$	

	${}^{1}L^{\delta}_{Pd,Zn:Pd} = -10800 + 3T$
	${}^{0}L^{\delta}_{Zn:Pd,Zn} = -84000 - 90.5T$
	${}^{2}L^{\delta}_{Zn:Pd,Zn} = -32000 + 16T$
	${}^{0}L^{\delta}_{Pd,Zn:Zn} = -84000 - 90.5T$
	${}^{2}L^{\delta}_{Pd,Zn:Zn} = -32000 + 16T$
ξ-Pd_2Zn_1	$(Pd,Zn)_2(Pd,Zn)_1$
	${}^{0}G^{\xi}_{Pd:Pd} = GHSERPD + GHSERPD + 20000$
	${}^{0}G^{\xi}_{Zn:Pd} = GHSERZN + 2\,GHSERPD + 50000$
	${}^{0}G^{\xi}_{Pd:Zn} = 2\,GHSERPD + GHSERZN - 139200 + 16.72T$
	${}^{0}G^{\xi}_{Zn:Zn} = GHSERZN + GHSERZN + 1000$
	${}^{0}L^{\delta}_{Pd:Pd,Zn} = -30800 - 5T$
	${}^{1}L^{\delta}_{Pd:Pd:Zn} = -7500$
$\beta_1Pd_{57}Zn_{43}$	$(Pd,Zn)_{57}(Pd,Zn)_{43}$
	${}^{0}G^{\beta_1}_{Pd:Pd} = 0.57\,GHSERPD + 0.43\,GHSERPD + 40000$
	${}^{0}G^{\beta_1}_{Zn:Pd} = 0.43\,GHSERZN + 0.57\,GHSERPD + 30000$
	${}^{0}G^{\beta_1}_{Pd:Zn} = 0.57\,GHSERPD + 0.43\,GHSERZN - 55086 + 3.14T$
	${}^{0}G^{\beta_1}_{Zn:Zn} = 0.57\,GHSERPD + 0.43\,GHSERZN + 500$
ξ_1-$PdZn_2$	${}^{0}G^{\xi_1}_{Pd:Zn} = GHSERPD + 2\,GHSERPD - 156019.43 + 21.43T$
η-$Pd_{91}Zn_9$	${}^{0}G^{\eta}_{Pd:Zn} = 0.09\,GHSERPD + 0.91\,GHSERZN$-21105+4.05T

Altough the model does not reproduce all details of the experimental phase diagram, in particular some of the phase boundaries, it serves well for the extrapolation of activity data at 300-500°C in the area between 50-70 at. % Zn, which is the area of intrest in the current study.

5.2. Pseudo-Isopiestic Measurements

These measurements were conducted in order to verify the calculated Zn activities, obtained by the CALPHAD model. The experiments were performed in a "reversed-pseudo-isopiestic-method". Therefore, instead of synthesizing a compound with a certain composition, an already synthesized compound was used as starting material. A temperature gradient was applied and lowered until zinc started to evaporate from the sample. The temperature were zinc vapour was visible on the cooler side of the crucible was compared to the calculated temperature of the CALPHAD model. A sample with a composition of $Pd_{33}Zn_{67}/Al_2O_3$ (5 wt. % loading of palladium on Alox) was prepared. For the reversed-pseudo-isopiestic measurement, a small temperature gradient between heat source and sink of the sample was applied. The source temperature (sample temperature, T_S) was fixed while the corresponding sink temperature (reservoir temperature. T_R), where elemental zinc should have the same vapour pressure as zinc in the compound, was calculated via the obtained activities of the CALPHAD-model. The vapour pressure of pure zinc at the reservoir temperature was calculated according to the equation published by Hultgren et al [30].

$$p_{Zn}^{0} = a - \frac{b}{T} - clnT \tag{42}$$

Table 4 Values a,b and c for calculating the standard pressure of zinc at different temperatures

	400K<T<692.65K	692.65K<T<1700K
a	30.76	33.47
b	15910.00	15360
c	0.73	1.26

The activities obtained from the CALPHAD model and the vapour pressure of pure zinc were used to calculate the vapour pressure of zinc over the compound $Pd_{33}Zn_{67}$ (equ. 9). A temperature Ts was chosen and the corresponding partial pressure of zinc inside the compound was used to find the temperature where the vapour pressure of pure zinc is equal to the vapour pressure of zinc inside the compound. Table 3 shows chosen values for T_S and the corresponding reservoir temperatures (T_R). The pressure of pure zinc ($p°_{Zn}$) and zinc in the component (p_{Zn}) are equal.

Table 5 Calculated source and sink temperatures at equilibrium

T_R [°C]	p_{zn} [Pa]	T_S [°C]	a_{zn}	$\ln a_{zn}$
300.0	0.1905	416.85	0.01023	-4.58
335.4	0.844	446.85	0.02054	-3.89
334.05	1.197	456.85	0.01475	-4.22
352.57	1.682	466.85	0.02399	-3.73
360.96	2.342	476.85	0.02565	-3.66
369.25	3.232	486.85	0.02728	-3.60

For synthesis of the compound $Pd_{33}Zn_{67}/Al_2O_3$, the reservoir temperature was increased in order to establish a smaller temperature gradient. After the reaction of zinc with the supported Pd/ Al_2O_3 powder, no zinc residue was visible inside the reaction crucible. The temperature of T_R was now lowered in steps, while keeping the temperature of T_S constant, until elemental zinc started to deposit at the sink temperature. When small zinc crystals were visible at the sink side, it was assumed that the vapour pressure of zinc in the synthesized palladium-zinc powder was now equal to the vapour pressure of elemental zinc. Since the activity is constant inside a two phase field and only a little amount of zinc residue was observed, the resulting compound should still lie in the two phase field region but with a slightly less zinc. A furnace temperature profile of such an experiment is shown in Figure 57 Temperature profile of a two-zone furnace. Distance is the depth of the furnace.

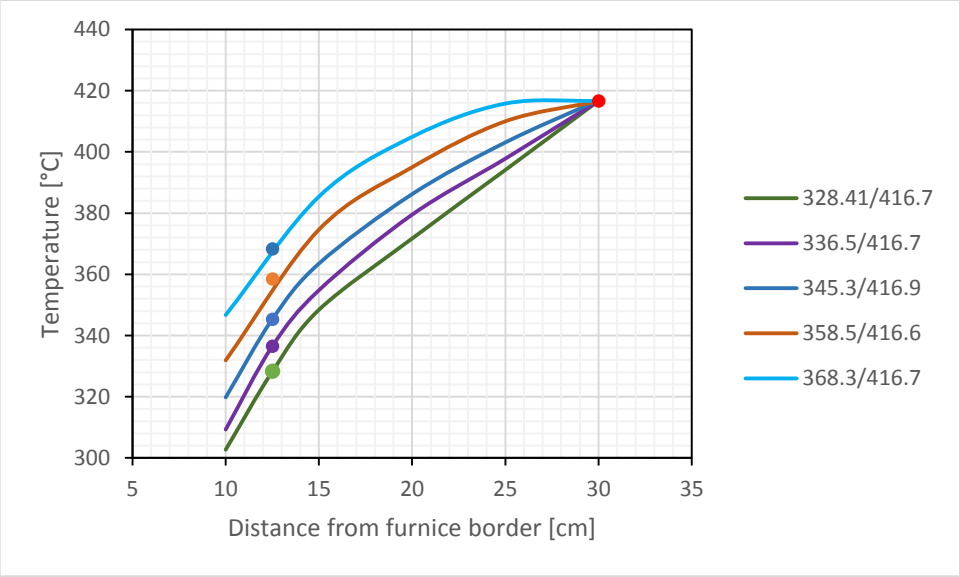

Figure 57 Temperature profile of a two-zone furnace. Distance is the depth of the furnace

The samples were placed between 30 centimetres (T_S) and 12.5 centimetres (T_R,) and observed for several days at the temperatures shown in Figure 57. The results from three

different temperature measurements are shown in Table 4. The results show a deviation of ca. 30°C between the calculated and experimentally observed reservoir temperatures.

Table 6 Calculated and observed source and sink temperatures

Gradient Calc. [°C]		Gradient Obs. [°C]	
T_r	T_s	T_r	T_s
369.2	486.8	400.9	486.8
344.5	457.2	374.3	457.2
299.9	416.7	328.2	416.7

From these observed temperatures the activities of zinc in the compound were calculated and compared to the activities of the calculated temperatures. The results are summarized in table 5

Table 7 Comparison of activities of zinc in the alloy calculated from theoretical and observed temperature gradients

	$a_{Zn,Ts}$ calc.	$a_{Zn,Ts}$ obs.	ln $a_{Zn,Ts}$ calc.	ln $a_{Zn,Ts}$ obs.
Isopiestic 1	0.02809	0.0844	-3.57	-2.47
Isopiestic 2	0.02204	0.0711	-3.82	-2.64
Isopiestic 3	0.01027	0.0365	-4.58	-3.31

The resulting activities indicated that the model in the δ+ξ_1 region need some adjustment at lower temperatures, to fit the experimentally obtained results. The reason for the deviation between the experiment and the theoretical values might lie in the lack of thermodynamic data of the ξ_1-phase. Since no thermodynamic data was available for this phase, its the Gibbs energy and temperature dependence was estimated. Another reason for the devation of experiment and calculation could be the large variation of the activities around the stoichiometric composition. Activities around 50 at. % zinc showed a mean deviation of ±0.01which couldn´t be described by the CALPHAD model. Activities, obtained by Chiang and Ipser, around the stoichiometric compositions are summarized in table 6. For a better modelling of the δ-phase around the stoichiometric composition, calorimetric measurements should be performed to measure the enthalpy of formation of the palladium-zinc 1:1 compound and the ξ_1-phase, which can then be used in a CALPHAD reassessment. Relying on activities, afflicted with such a large mean error will probably not lead to the desired results. Last but not least, it should be pointed out that the activities of the samples may deviate from the bulk activities due to the nano crystalline character of the PdZn particles. At this particle size, surface energy effects on the thermodynamic properties cannot be neglected.

Table 8 Experimental results from Chiang and Ipser for the Zn-activities around the stoichiometric composition

No.	At. % Zn	Phase	Ts [K]	$\ln a_{Zn,Ts}$	$a_{Zn,Tr}$
Run5		Tr= 655 K	26 days		
3	50.06	β_1	808	-4.27	0.01398
4	49.99	β_1	858	-5.3	0.00499
5	49.98	β_1	889	-5.88	0.00279
Run3		Tr= 679 K	26 days		
2	50.17	β_1	801	-3.27	0.03800
3	50.16	β_1	841	-4.12	0.01624
4	49.98	β_1	912	-5.44	0.00433
5	49.95	β_1	953	-6.11	0.00222
Run4		Tr= 701 K	26 days		
3	50.09	β_1	839	-3.38	0.03404
4	50.08	β_1	886	-4.28	0.01384
5	49.98	β_1	924	-4.94	0.0071
6	49.89	β_1	963	-5.56	0.00384
Run2		Tr= 735 K	26 days		
8	50.08	β_1	943	-4.29	0.01370
9	50.05	β_1	966	-4.65	0.0095
10	50.07	β_1	987	-4.96	0.00701
11	50.01	β_1	1010	-5.29	0.00504
12	50.03	β_1	1029	-5.55	0.00388
13	49.99	β_1	1048	-5.79	0.00305

5.3. Sample preparation

The conditions for sample synthesis were chosen according to their composition. Early experiments showed that at zinc contents, higher than 53 at. % zinc, the reaction time for zinc vapour with the palladium powder is significantly longer. If the powder did not fully reacted after one week, the temperature on both sides of the gradient was increased. This stepwise increasing of the temperature was necessary, in order to keep the reaction temperatures as low as possible in order to avoid possible sintering or agglomeration of the powder. Table 8 shows a summary of all samples and synthesis conditions.

Table 9 Synthesis Conditions of all samples

Samples	Expected Composition		Synthesis Conditions
	Pd	Zn	
PaWi003	47.6	52.4	1 W*380 °C / 480 °C
PaWi006	47.6	52.4	1 W 310 °C / 342 °C
PaWi010	45	55	1W 310 °C / 350 °C, 1W 360 °C/ 395 °C
PaWi011	42	58	1 W 310 °C / 350 °C, 1 W 360 °C/ 395 °C
PaWi013	37	63	2 W 380°C / 310 °C, 2 W 400 °C / 312
PaWi015	41	59	2 W 380 °C / 310 °C, 2 W 400 °C / 312 °C, 2 W 418 °C / 346 °C
PaWi020	41	59	PaWi015 2 Weeks Isotherm at 418°C
Isopiestic 1	33	67	Sample used for Isopiestic Testing
Isopiestic 2	-	-	Isopiestic Test 5 W 416.7 °C / 328.4 °C

** Reaction time in weeks*

Although sample PaWi010 showed zinc oxide on the walls of the reaction crucible, due to residual water or oxygen, after the reaction, the catalytic performance was tested in order to investigate the influence of possible palladium oxide on the catalytic properties. Sample PaWi020 underwent an additionally isothermal heat treatment at 418°C for 2 weeks. For this experiment, a part of sample PaWi15 was resealed in a quartz glass vessel and transferred into a furnace. It should be noted that the resealing of the sample might introduce agglomeration of the particles, since the nano powder now consists of palladium and zinc instead of the first sealing, where the powder consists mainly of Alox and palladium. Sample Isopiestic 1 was prepared at different temperatures and used to verify the calculated isopiestic temperature gradients by the CALPHAD model. The calculated and observed gradients are shown in Table 5. Sample Isopiestic 2 was prepared in order to verify the gradient obtained by the isopiestic measurements of sample Isopiestic 1. In this sample, a small amount of powder was sealed together with a large zinc reservoir and transferred into a two-zone furnace. The observed temperature gradient shown in Table 5 (Isopiestic 3 obs.)

was applied. The sample was left in the furnace for 5 weeks, giving it enough time to reach equilibrium. After 5 weeks the composition was measured. Samples Isopiestic 1 and 2 were prepared in order to test the assessed CALPHAD model and were therefore not tested for their catalytical performance.

5.4. Results of catalytic Testing

The catalytic testing of the samples was done at the Max-Planck-Institute for Chemical Physics of Solids in Dresden as described in section 4.8. Conversion, Activity and CO_2-selectivity were investigated. Note that the activity is usually calculated by millimol hydrogen per gram catalyst per hour but for a better comparison with other literature, the activity was transformed to millimol hydrogen per millimol palladium per hour. If the course of a reaction or the active site are still unknown, then the activity is ususally described in terms of the amount of noble metal rather than the total amount of the catalyst. This transformation also allowed for a better comparison with the reference catalyst $CuO/ZnO/Al_2O_3$. For the transformation to millimol palladium the weight percentage of palladium obtained by ICP-OES-analysis was used. The composition and nomenclature of the samples are shown in Table 9. The same temperature profile was used for all measurements. The temperature profile was set to several isothermal heating and cooling steps of 50 minutes at 150-200-250-300-275-225-175-200-250-300°C, with intermediate heating and cooling of two Kelvin per minute. The time for the last isothermal step was increased to four hours. Figure 58 shows the CO_2-selectivity and Figure 61 shows the conversion, with the corresponding temperature profile, of the Sample PaWi011.

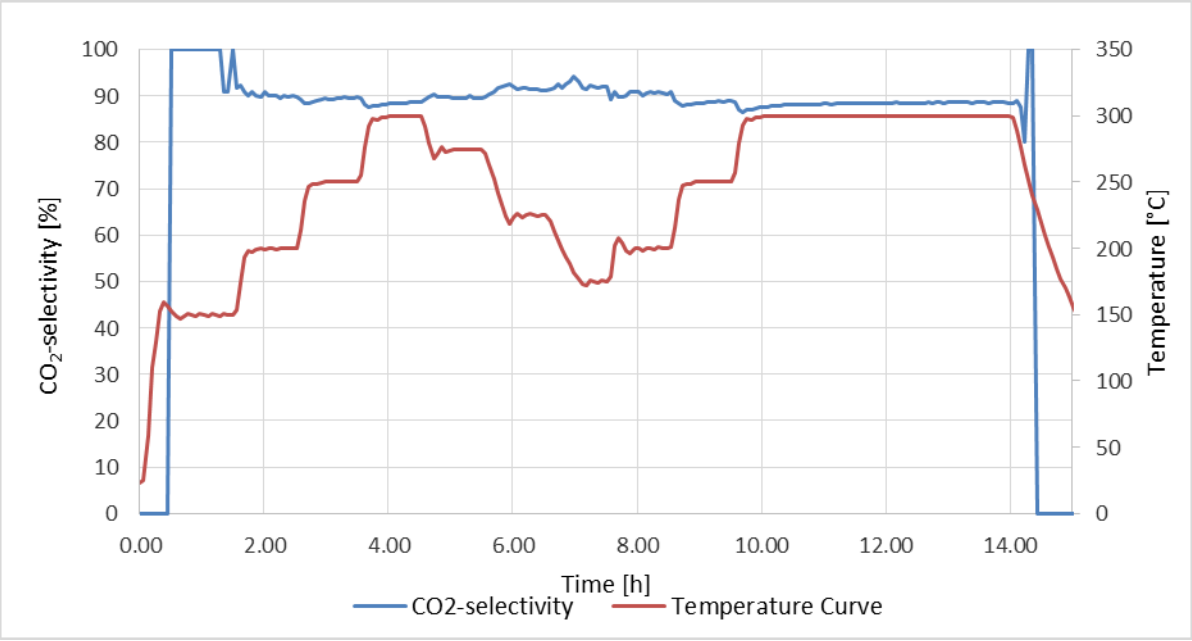

Figure 58 CO_2-selectivity of the Sample PaWi011 in methanol steam reforming as a function of reaction temperature and time

Comparing the resulting CO_2-selectivities of all samples showed that the selectivity was almost independent of the temperature and depended mainly on the initial zinc composition

of the sample. During the four-hour long isothermal section, no deactivation of the catalyst was observed in any sample. The sharp peaks of the CO_2-selectivity at the beginning and the end of the measurement are artefacts caused by the on and off switching of the reactive gases. Plotting the Selectivity against the composition yielded the following plot(note that the line is only a guide to the eye):

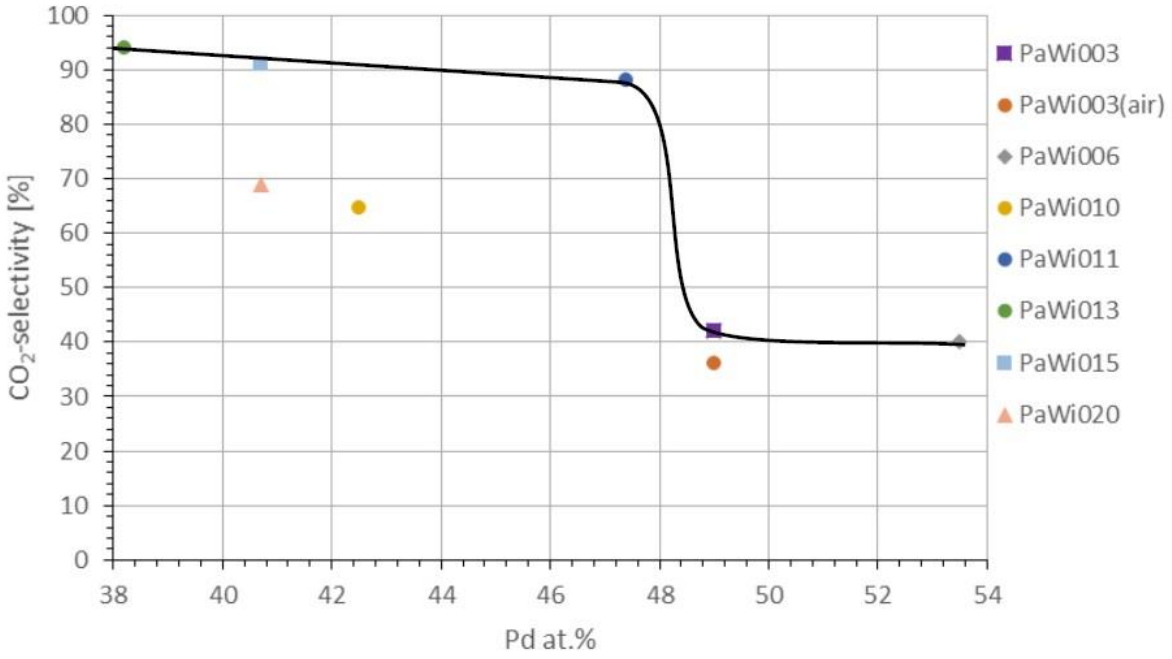

Figure 59 Dependence of CO_2-selectivity on palladium content under MSR-conditions (MeOH:H_2O = 1:1) at a reaction temperature of 300°C

The CO_2-selectivity increased drastically for samples above 50 at. % zinc. The samples PaWi010, PaWi003 and PaWi020 were not included in the graph since they were synthesized or measured under different conditions. PaWi010, as already mentioned above, was partially oxidised during the reaction and therefore it was not included in the comparison to other samples. In the case of sample PaWi003(air) the preparations for the catalytic testing were done under air instead of the glovebox and the sample received an additional reduction pre-treatment. Because of the different handling and pre-treatment, this sample was not used for direct comparison. This experiment showed that the samples either has to be exclusively handled under Argon or that the reduction process is diminishing the catalytic activity.

It was still unclear if zinc was equally distributed in the nano powder after synthesize. To clarify the situation a part of sample PaWi015 received an additional isothermal heat treatment as described in section 3.1. and the resulting sample was called PaWi020. Because of the different synthesis conditions the sample was not included in the comparison of the CO_2- selectivity of other samples. After annealing the CO_2-selectivity decreased drastically.

The reason for this might lie in the resealing of the nano powder. After the reaction, the nano powder consists of palladium and zinc. It could be possible that during the sealing of the powder in the glass vessel, the powder started to agglomerate or zinc distributed unevenly during the isothermal reaction.

The CO_2-selectivity of palladium-zinc bulk samples, obtained by Friedrich [20] are shown in Figure 60.

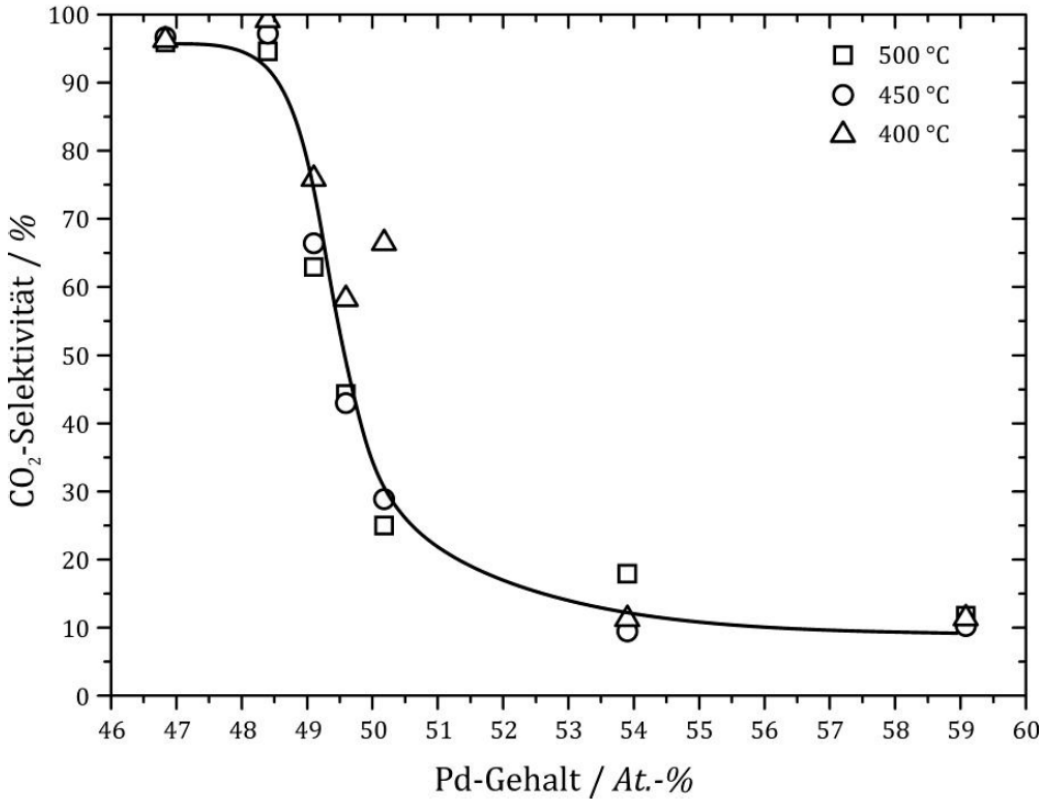

Figure 60 Dependence of CO_2-selectivity on palladium content under MSR-conditions (MeOH:H_2O= 1:1) at different temperatures.[21]

Despite the different reaction temperature, the CO_2- selectivity of the bulk material and the supported nano-particles were quite comparable. In case of the supported nano particles, the sharp increase of selectivity shifted to 52 atomic percent zinc compared to the sharp shift at 51 at. % of the bulk material. Since both curves were only estimated, the shift could also occur at the same composition. While Friedrich [20] observed a plateau of CO_2-activity at 53 at. % zinc, the CO_2-selectivity of the supported nanoparticles continued to steadily increase up to 60 at. % zinc. Requiring less amount of a noble material is quite favourable, since it will decrease the price of the catalyst, and therefore making it more attractive for industrial application. Friedrich [20] reported that zinc rich bulk samples of palladium zinc had similar CO_2-selectivities as the supported catalyst ZnPd/ZnO. The reason for this

increased selectivity was, according to Friedrich, either the result of a high zinc content of the ZnPd particles on the ZnO carrier particles and/or the zinc oxide formed on the surface of the PdZn-particles during the reaction as well as the zinc oxide carrier material. Since the partial oxidised sample, PaWi010 exhibited a decreased selectivity and conversion, compared to samples with lower zinc content, it was concluded that the selectivity depended mainly on the zinc content and present palladium oxide counteracted the selectivity. It is also possible that ZnO, which is formed during synthesis, counteracts the selectivity because it could cover the whole surface of several PdZn nano-particles where as in-situ formed ZnO during the MSR experiment provides a larger interface between ZnO and PdZn, which promotes the CO_2-selectivity.

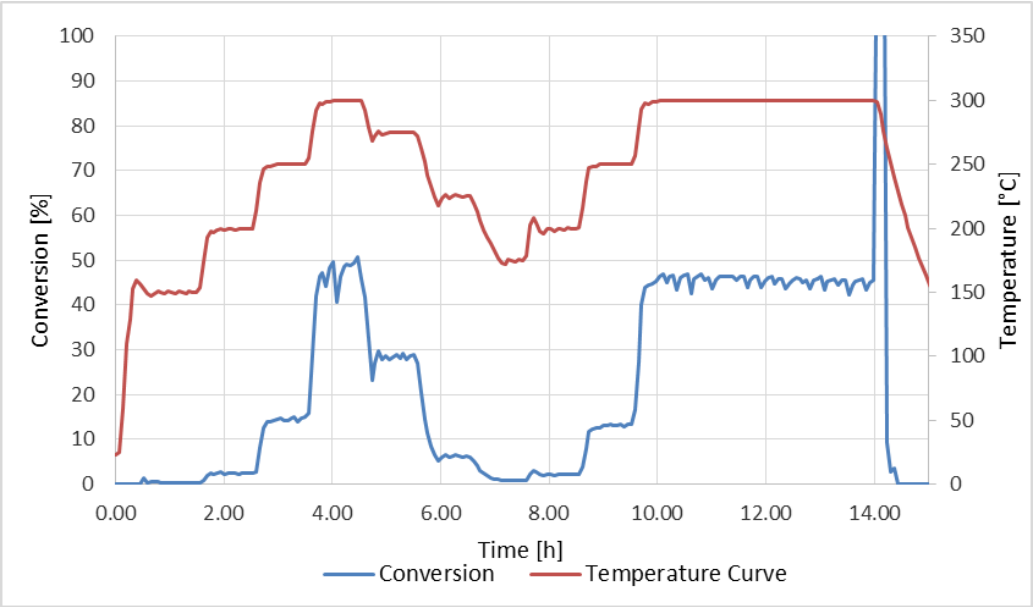

Figure 61 Figure Conversion of the Sample PaWi011 in methanol steam reforming as a function of reaction temperature and time

All samples showed that the conversion was proportional to the reaction temperature. The conversion curve seemed to be not as smooth as the selectivity curve. The reasons for these discontinuities could be slight inhomogeneities of the catalyst in the catalyst/graphite mixture, possible changes on the surface of the catalyst material or slight discontinuities of the reactant gas flow. A large change in conversion could be observed between 250°C and 300°C. The conversion rate changed from 46% at 300°C to 29% at 275°C. In comparison to the $CuO/ZnO/Al_2O_3$ catalyst, no deactivation could be observed at 300°C. Table 10 shows a comparison of conversion of all samples

Table 10 Conversion [%] at 300 °C averaged over a 4 hour long isothermal step

	Pd at. %	Zn at. %	Conversion at 300°C
PaWi003	49	51	24.6
PaWi003(air)	49	51	18.5
PaWi006	53.5	46.5	31.6
PaWi010	42.5	57.5	35.4
PaWi011	47.4	52.6	45.5
PaWi013	38.2	61.8	60.3
PaWi015	40.7	59.3	58.4
PaWi020	40.7	59.3	30.1

According to the investigations of bulk palladium-zinc from Friedrich, increased zinc, content correlated directly to an increase in conversion and an identical behaviour was expected for the supported nanoparticles. The samples PaWi003(air), PaWi010 and PaWi020 were excluded from the interpretation of the data for the same reasons as mentioned above (Note that the line should only serve as a guide to the eye).

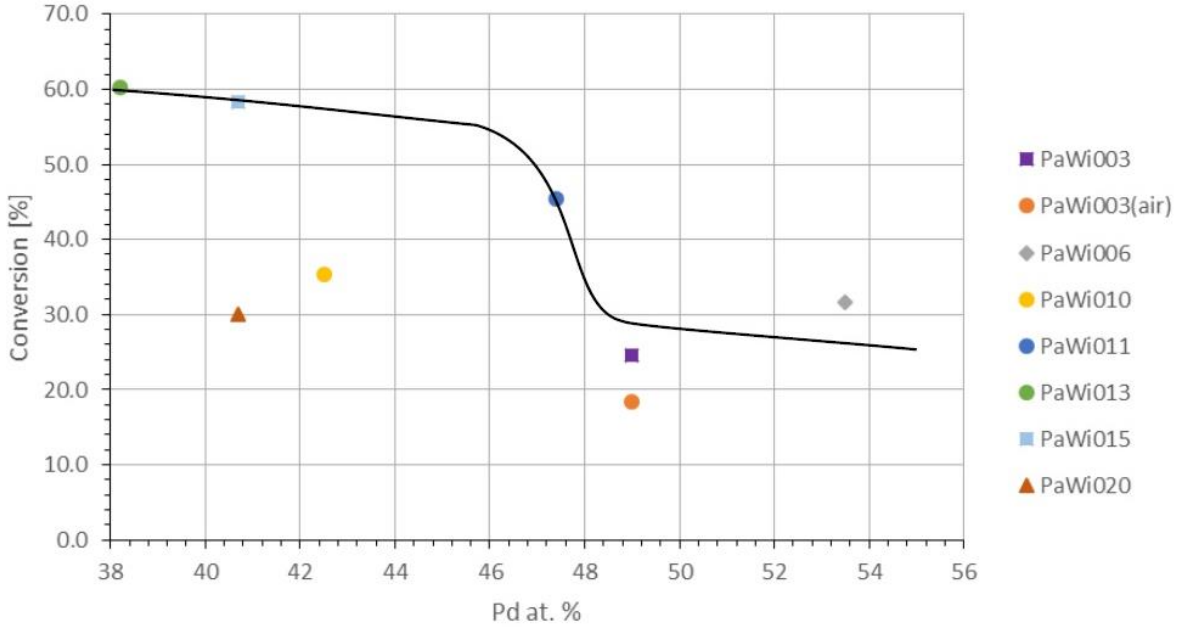

Figure 62 Dependence of Conversion on palladium content under MSR-conditions (MeOH:H_2O = 1:1) at a reaction temperature of 300°C

The reason for the reduced conversion of the sample PaWi003 compared to sample PaWi006, despite its higher zinc content and higher CO_2-selectivity couldn´t be explained during this work. A possible explanation could be an insufficient mixing of the nano powder with the filling material, which could lead to an inhomogeneous distribution and therefore a reduced conversion. Sample PaWi003 also had with the highest source temperature during synthesize (480°C). It could be possible that during the reaction with zinc, nanoparticles

started to agglomerate. Agglomeration of particles would lead to a reduced surface and therefore also a reduced conversion. Agglomeration during the heating of the original nano powder (Pd/Al_2O_3, 5 wt. % loading) could be excluded since the CO_2-selectivity [%] and conversion [%] of other samples were comparable to the bulk material. Since zinc is a very mobile element, agglomeration due to the adding of zinc lied within the realm of possibilities. Overall, the conversion increased with increasing zinc content up to 60% for 62 at. % zinc. To compare the overall catalytic quality of the syntheseized catalysts, the CO_2-selectivity was plotted against the activity. The catalysts are listed in Table 11. . A good catalysts should have a high activity combined with a high selectivity. In this case. the most promising catalyst would be PaWi013 since it showed the highest activity while having a selectivity of 94%.

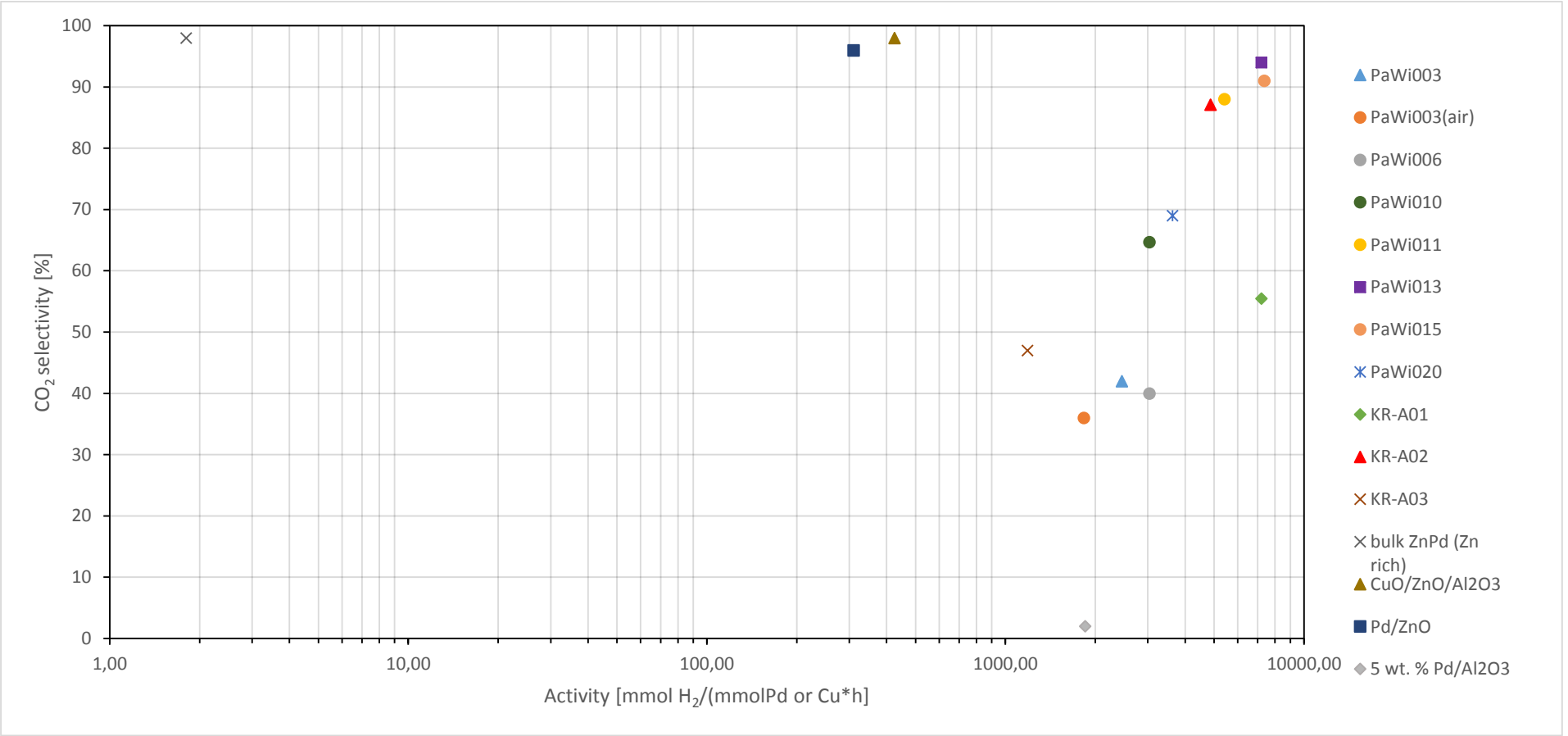

Figure 63 CO_2-selectivity plotted against the activity in mmol H_2/mmol Pd or mmol Cu per hour of samples and model catalysts under MSR conditions (MeOH:H_2O = 1:1) [20]

Table 11 Activity and CO2-selectivity of all Samples and referenced catalysts

Samples	Pd	Zn	temperature treatment	activity at 300 °C	CO_2 selectivity [%]	Conversion [%]
	ICP/OES [at.-%]			at 300°C	at 300°C	at 300°C
				[mmol H2 / mmol Pd h]		
PaWi003	49	51	1W 380 °C / 480 °C	2452.91	42	24.6
PaWi003(air)	49	51	1W 380 °C / 480 °C	1830.00	36	18.5
PaWi006	53.5	46.5	1W 310 °C / 342 °C	3030.98	40	31.6
PaWi010	42.5	57.5	1W 310 °C / 350 °C, 1W 360 °C/ 395 °C	3870.06	64.7	35.4
PaWi011	47.4	52.6	1W 310 °C / 350 °C, 1W 360 °C/ 395 °C	5411.33	88	45.5
PaWi013	38.2	61.8	2 W 380°C / 310 °C, 1W 400 °C / 312	7201.88	94	60.3
PaWi015	40.7	59.3	2 W 380 °C / 310 °C, 1W 400 °C / 312 °C 1W 418 °C / 346 °C	7352.00	91	58.4
PaWi020	41	59.3	RK3O006 2 Wochen Isotherm bei 418°C	3625.70	69	30.1
KR-A01*	50.5	49.5	450 °C / 480 °C	7201.55	55.5	-
KR-A02*	40.2	59.8	450 °C / 480 °C	4862.41	87.1	-
KR-A03*	47.4	52.6	450 °C / 480 °C	1184.00	47	-
bulk ZnPd (Zn rich)	-	-	-	1.8	98	-
$CuO/ZnO/Al_2O_3$	-	-	-	425	98	-
Pd/ZnO	-	-	-	310	96	-
5 wt. % Pd/Al_2O_3	-	-	-	1850	2	-

*Samples prepared and measured by Prof. Mag. Dr. Klaus Richter

The last question was the influence of the carrier material on the catalytic performance of intermetallic PdZn nano particles. For this purpose zinc-rich bulk material of the composition Pd48Zn52 (composition determined by ICP-OES) was grinded with alpha-Al_2O_3 in a ball mill and tested in MSR. The amount of bulk material was chosen so that the amount of palladium was about 5 wt. % Pd of the total mass, so that the mixture was as close to the nano particle samples as possible. This experiment should clarify if the presence of alumina oxide favours a side reaction for methanol decomposition or the water-gas-shift reaction (WGS). The results showed no influence of the carrier material on the catalytic activity and selectivity. The physical mixture of 5% PdZn ($Pd_{48}Zn_{52}$) in alpha-alumina showed that the selectivity of the bulk material is compareable to the selectivity of the nano-powder, while the conversion showed a deactivation after 4 hours. The physical mixture displayed an overall lower conversion compared to the samples with similar zinc content (Pawi003 and PaWi006) at the same temperature. While the nano powder showed catalytic activity an temperatures above 225°C, the physical mixture showed no activity up to 300°C.

The following Figures show the CO_2-selectivity and conversion of all samples, including the experiment with bulk material and alpha-Al_2O_3.

PaWi003 (air)

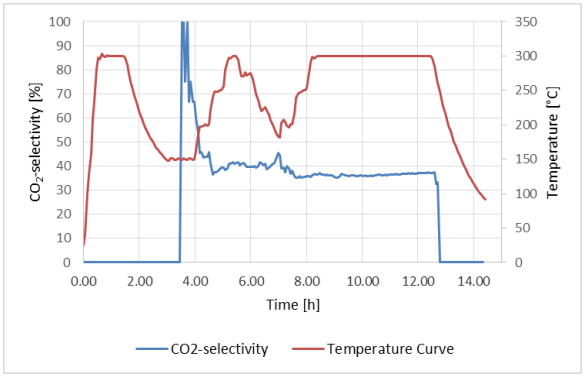

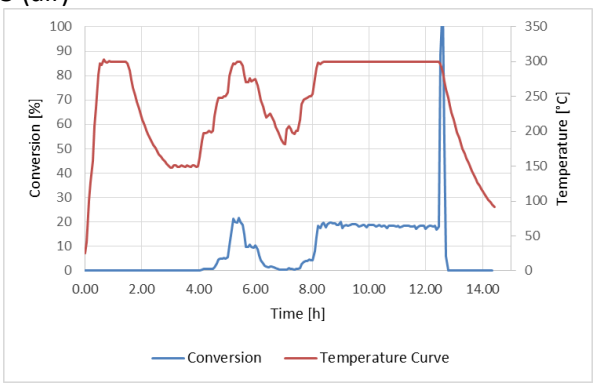

PaWi003

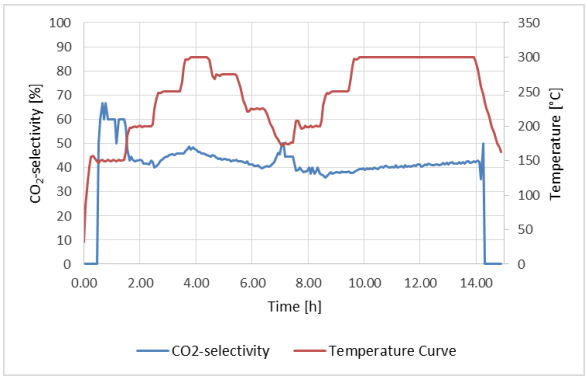

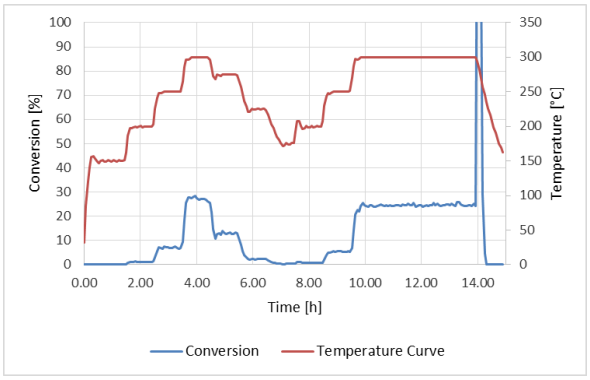

PaWi006

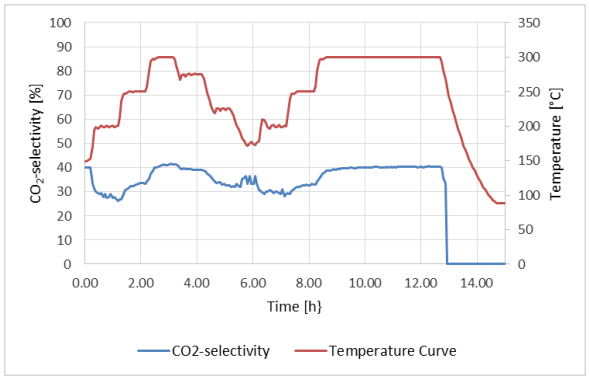

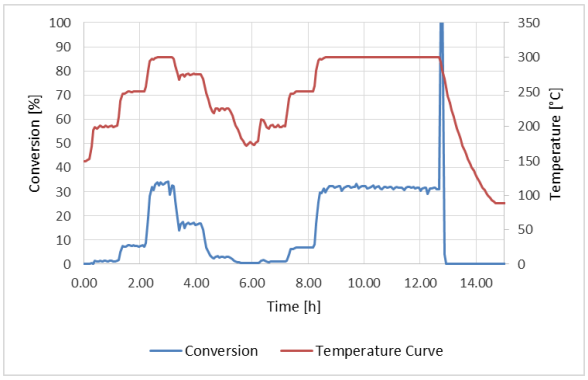

PaWi010

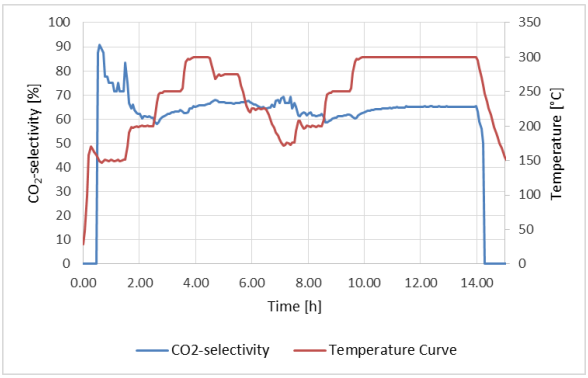

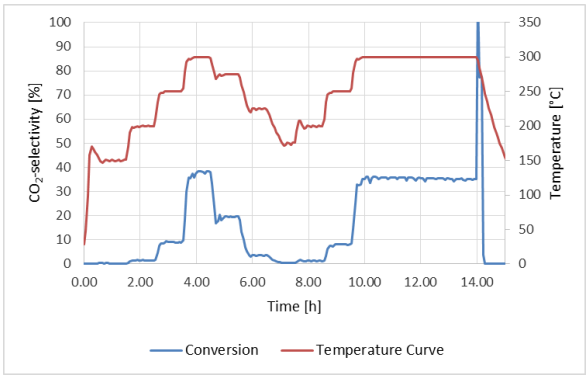

PaWi011

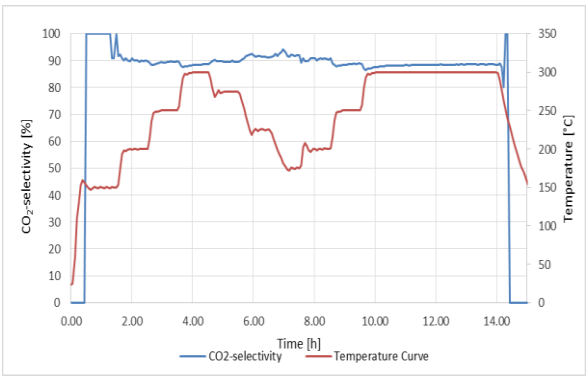

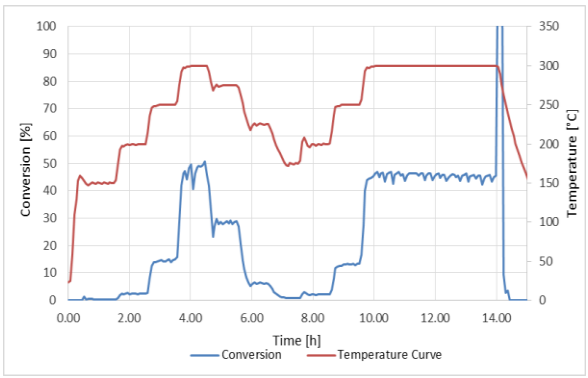

PaWi013

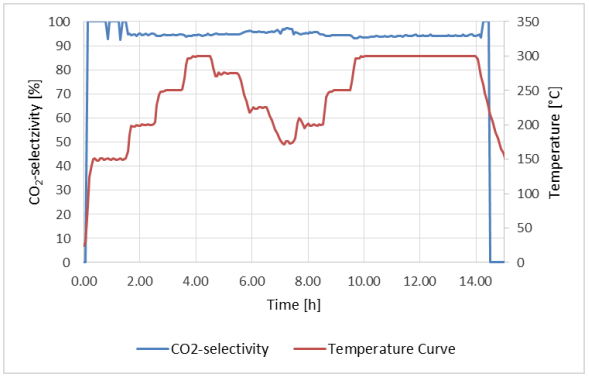

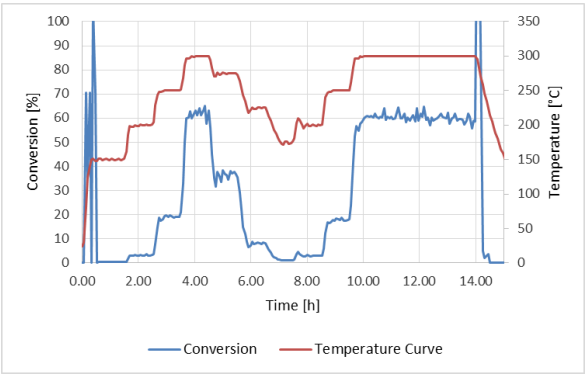

PaWi015

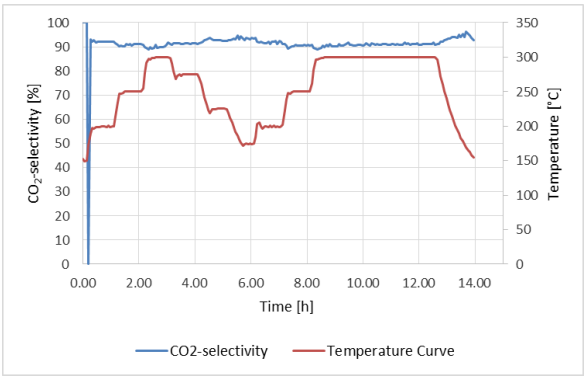

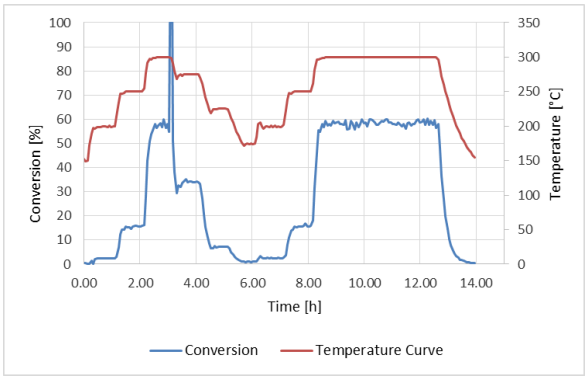

PaWi020

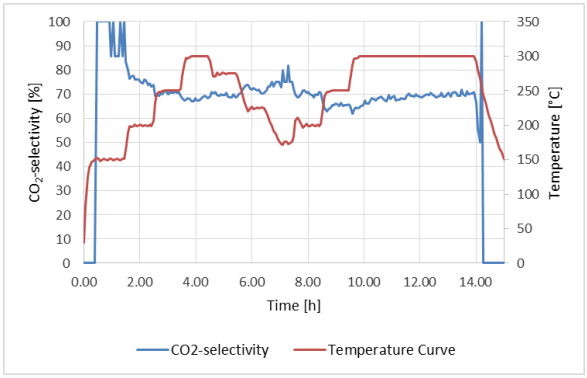

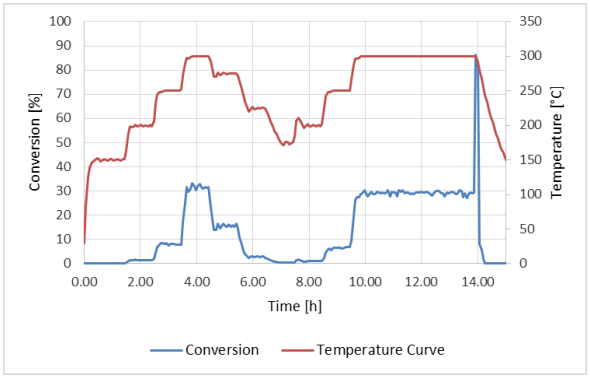

5% PdZn /bulk material in Al_2O_3

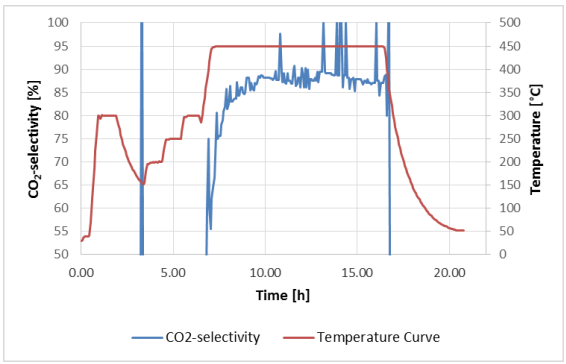

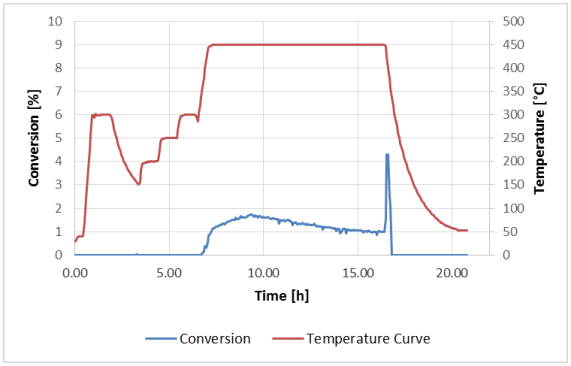

5.5. Characterisation of the Catalysts

5.5.1 X-ray-Characterisation

According to the phase diagram, all prepared samples should lie within the two-phase field PdZn(δ)+$PdZn_2$(ξ_1). After the reaction of the Pd/Al_2O_3 nano powder with zinc, XRD was used to identify the PdZn (1:1)-phase that should be present in all samples. Making an X-ray analysis of $Pd_{1-x}Zn_x$ nanoparticles, which are sitting on much larger aluminium oxide particles, was very difficult, since the carrier material produced a large background. It was impossible to refine the background with any known structure of aluminium oxide and the producer didn´t provide any manufacturing information. In order to eliminate the large background of the aluminium oxide it was necessary to prepare an X-ray diffraction pattern of pure carrier particles. For that purpose, palladium was removed by suspending the powder in concentrated nitric acid for 1 hour. After washing and drying the powder an X-ray diffraction pattern of the carrier was prepared. Figure 64 shows the X-ray-patterns of the cleaned nano powder, the original nano powder before the reaction with zinc and the reacted sample PaWi011.

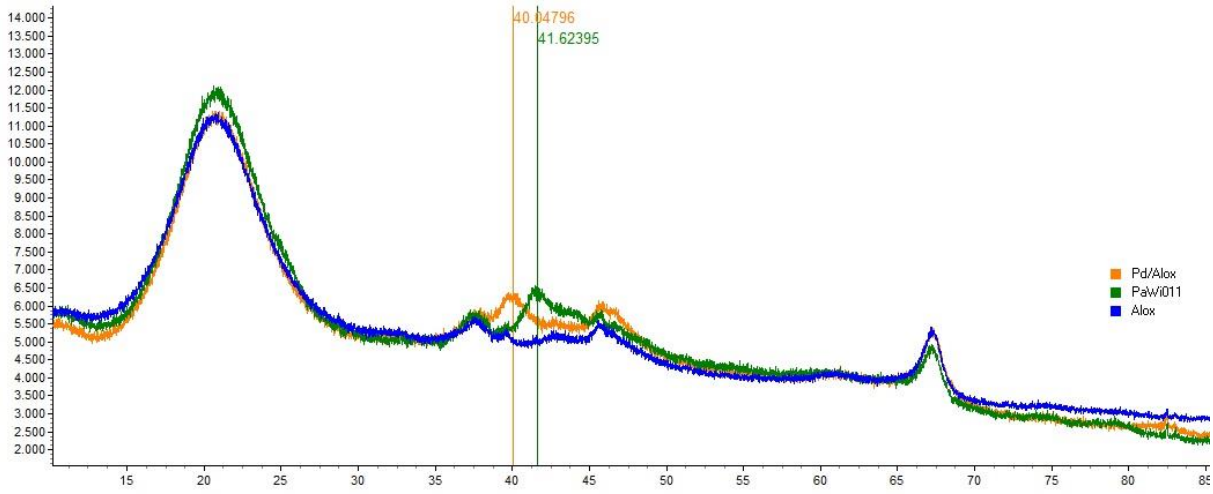

Figure 64 X-ray pattern of the original Pd/Alox-powder, the cleaned powder and the sample PaWi011

The peak at the 41.62 degrees (2θ degrees) corresponded to the (011)-reflex of PdZn while the peak at 40.04 degrees correspond to the (111)-reflex of elemental palladium. The large reflex between 15-30 degrees (2θ degrees) is produced by the sample carrier. The resulting X-ray-pattern of the cleaned Al_2O_3 nano powder was subtracted from the X-ray-patterns of the samples, yielding a pattern where only reflexes of the intermetallic phases should be present. Since the intensities of the measured X-ray patterns depended on the amount of

used powder it was not possible to directly subtract two profiles. Before subtracting the Al_2O_3-profile from a sample profile, their intensities were adjusted, using the program EVA (Evaluation) provided by BRUKER. After subtracting the background, all samples exhibited different intensities, making a direct comparison of these samples rather difficult. One sample was chosen as a reference and the intensities of all other samples were adjusted to the reference. The resulting X-ray-patterns are summarized in Figure 65 Comparison of all measures X-ray samples after background correction and normalization of the intensities.

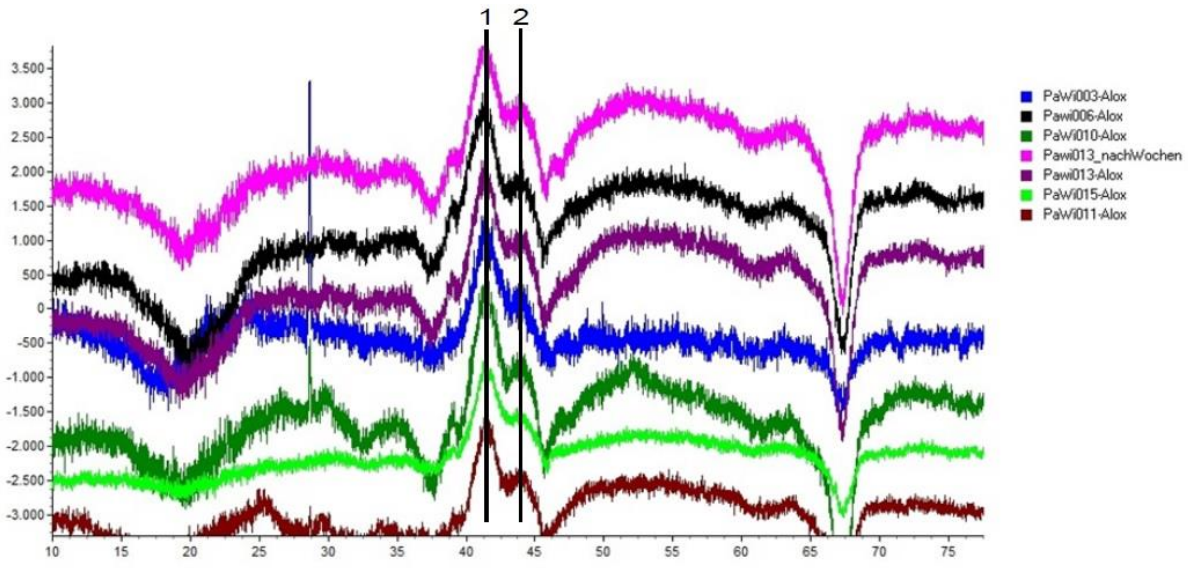

Figure 65 Comparison of all measures X-ray samples after background correction and normalization of the intensities

After the reaction, two PdZn peaks,1 (011) and 2 (110), were visible in all samples but no palladium or $PdZn_2$ (ξ-phase) peaks could be observed (Fig. 65). As an example, the X-ray analysis of PaWi011 is shown in Figure 66.

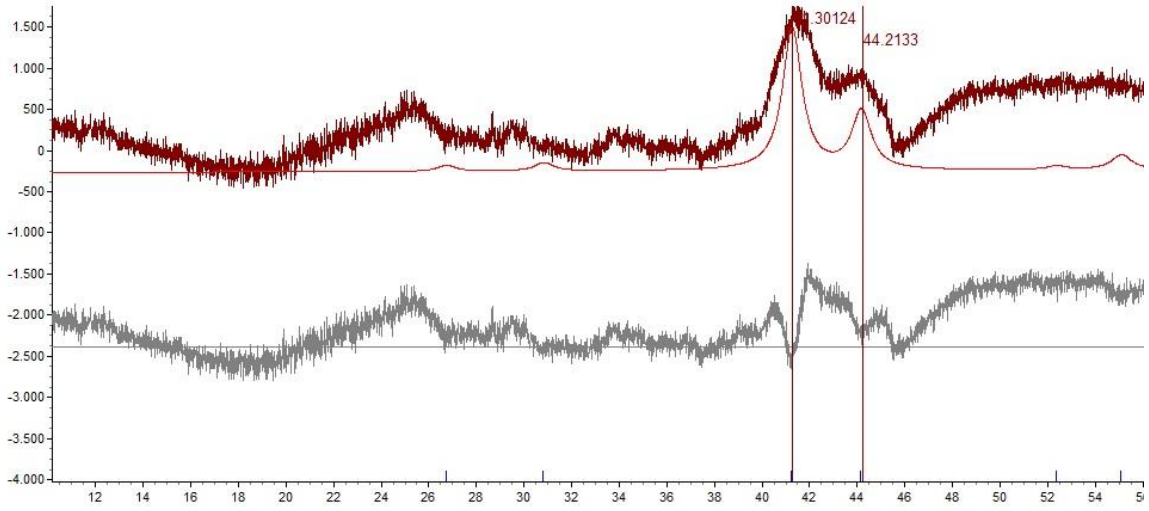

Figure 66 X-ray analysis of PaWi011. The measured profile (brown) and the calculated profile (red) of PdZn (δ-phase) show 2 peaks which can be found in both patterns. Other peaks which are present in the calculated PdZn-pattern disappear below the noise floor.

The refinement yielded a crystal seize domain of around 9 nanometer for the PdZn crystals. Because of the high noise, no information about the change of c-lattice parameters of the PdZn-Phase towards higher zinc content could be observed.

5.5.2. TEM Analysis

For a more detailed particle size statistic, the commercially available powder and the sample PaWi011 were investigated in a transmission-electron-microscope. The TEM images showed no visible difference between the starting material and the reacted samples. An example for a TEM image is shown in Figure 67.

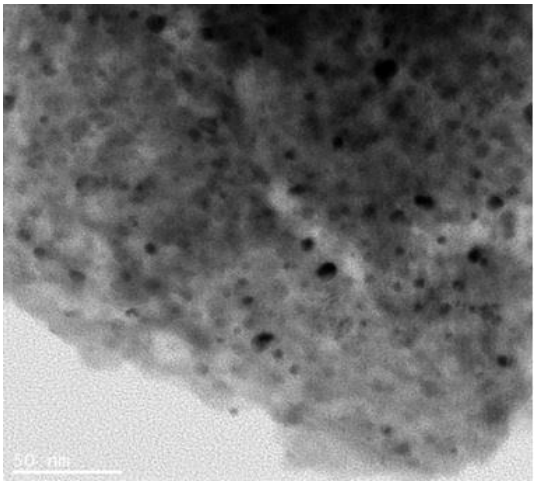

Figure 67 TEM image of sample PaWi011. The black dots are the PdZn particles (black) sitting on a larger Alox particle (dark grey).

The PdZn and palladium particles appeared to be oval shaped and therefore, the larger and smaller radii of over 300 PdZn or palladium particles were measured and averaged. The resulting particle seize statistics are shown in Figure 68 and Figure 69Figure 69 Particle seize statistic of palladium particles of the starting material.

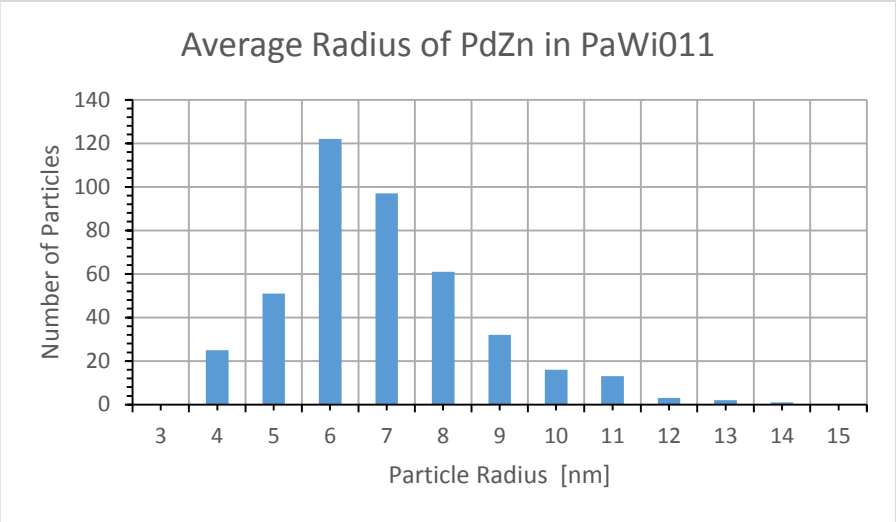

Figure 68 Particle size statistic of PdZn particles of the sample PaWi011

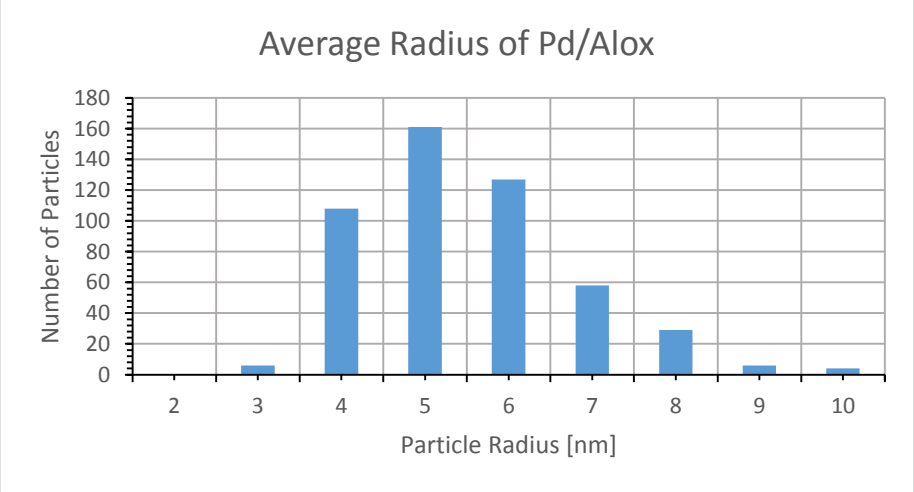

Figure 69 Particle seize statistic of palladium particles of the starting material

After the reaction with zinc, the average particle radius increased from 5nm to 6nm and the overall distribution width increased as well. If the radius would have changed more than 1 or 2 nano meters it could be assumed that particles might have started to agglomerate. No agglomeration or clusters of the PdZn-particles were observed in case of the sample PaWi011. The small change in particle seize and the absence of agglomeration are critical parameters for the manufacturing of a catalyst. Particle size or particle size distribution of the catalyst particles has a direct influence on reactivity. Smaller Particles have a higher

surface and should therefore have a higher activity while agglomeration would reduce the surface of the catalyst and therefore reduce the activity. In a next step, the electron-diffraction pattern of the starting material (Pd/Alox) and the sample PaWi011 were recorded and compared (Fig. 70 and Fig. 71). Both diffraction patterns exhibited a hexagonal unit cell for the alumina. The electron-diffraction-pattern couldn´t be refined using the structure of alpha-Al_2O_3. Additional reflexes (turquoise dots in Fig 70 and Fig 71) suggested a unit cell with a lattice parameter a, of twice the size of alpha alumina. All alumina oxide particles in both samples showed a hexagonal unit cell independent of which particle was investigated and without any adjustment of the particle position. The conclusion was reached that all alumina oxide particles consisted of several single crystals, all oriented with their c-axis parallel to the electron beam. The alumina particles appeared to be a few micrometres in length and width while the height had to be below 500 nano meters because recording an electron-diffraction-pattern of particles with a thickness greater than 500 nano meters would not be possible. Both diffraction patterns showed additional reflexes to alpha-alumina. In case of the starting material the additional reflexed were attributed to present palladium and in case of PdZn the reflexes were attributed to the present PdZn-phase. The reflexes of PdZn lied in the range of the calculated Debeye-ring but the intensities were too weak for a detailed analysis. The $Pd_{1-x}Zn_x/Al_2O_3$ particles were too small to determine the composition via electron-energy-loss-spectroscopy (EELS).

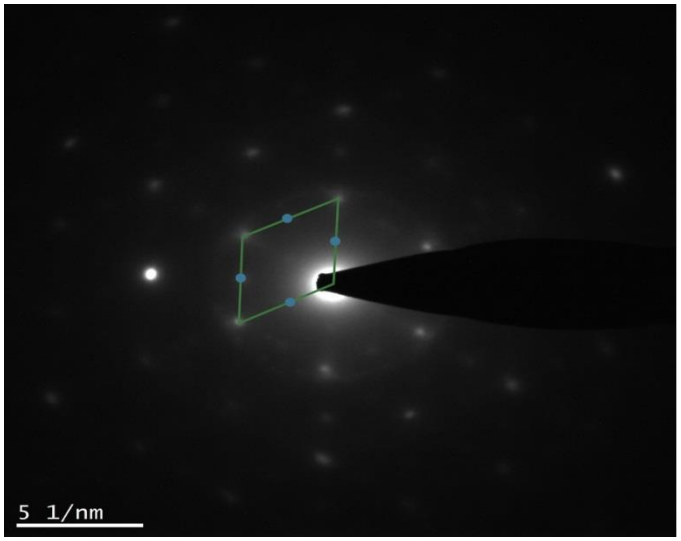

Figure 70 Electron-Diffraction-Pattern of the starting material

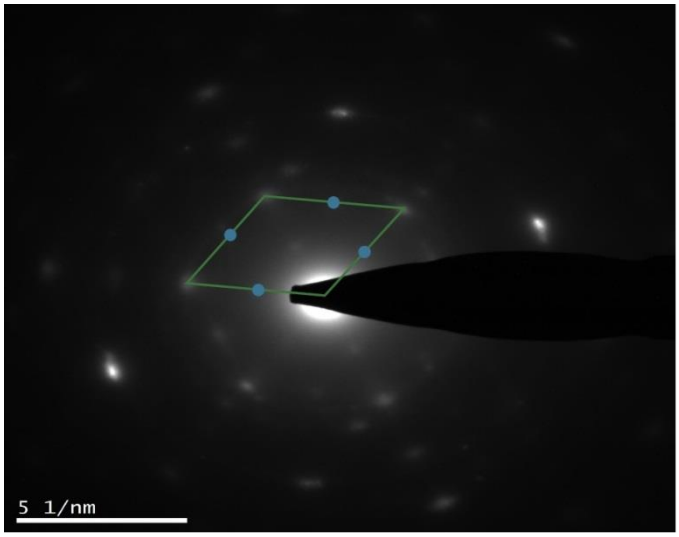

Figure 71 Electron-Diffraction-Pattern of PaWi011

5.5.3. AFM-Analysis

Atomic-force-microscopy was used for a detailed analysis of the particle height of the support. It was assumed that the height of the support particles didn`t change after the reaction with zinc and therefore only the starting material was investigated. The particles showed a height between 120 and 310 nano meters while the length and width was in the range of 2-3 micro metres.

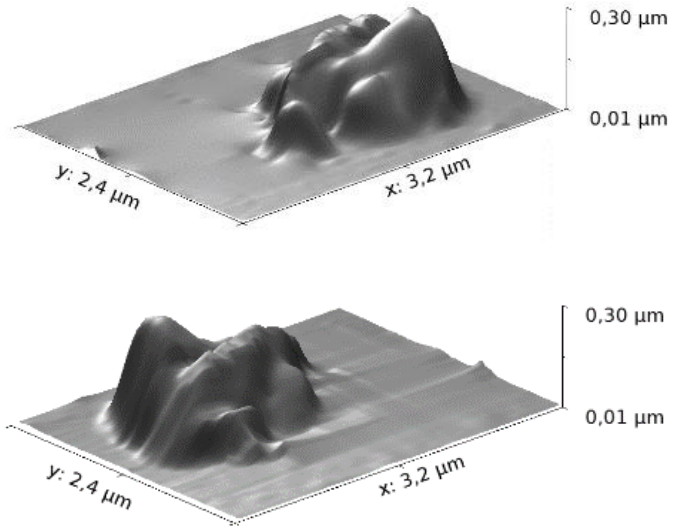

Figure 72 Front and back view of a nanoparticle

The results are in good agreement with the acquired TEM-results. The AFM-measurements confirmed that the height of the particles was smaller than their width and length. The difference in height and width/length was also an explanation for the measured electron-diffraction-patterns. It was assumed that the c-axis of the hexagonal lattice lied parallel to the z-axis of the particles (Figure 72) so that if the powder was applied to the surface of the sample carrier of the TEM it was more likely that the particle would lie on their x-y plane rather than on one of their x-z or y-z planes. This information was also an explanation for the large background of the alumina oxide particles in the XRD-pattern. X-ray powder analysis requires a statistical distribution of crystal orientations. A poor particle statistic can lead to incomplete Debye-Diffraction-Rings and can therefore cause errors in the observed diffraction peaks. Calculated diffraction patterns are based on a statistical distribution of the crystal orientations, so comparing them, with an observed diffraction pattern of a poor particle statistic will not give conclusive results.

5.5.4. SEM-Analysis

Scanning-electron-microscopy was used to determine the average radius of the carrier material. The resulting radii were between 1-30µm. The particles tended to cluster at higher concentrations making it rather difficult to determine the radii of single alumina oxide particles (Figure 73). SEM was also used to determine the composition of the PdZn particles. Note that SEM-analysis is a technique requiring flat surfaces and larger grains rather than a powder, so the acquired compositions were not as precise as the compositions of a conventional SEM-sample. The measured compositions are summarized in section 9.3. .

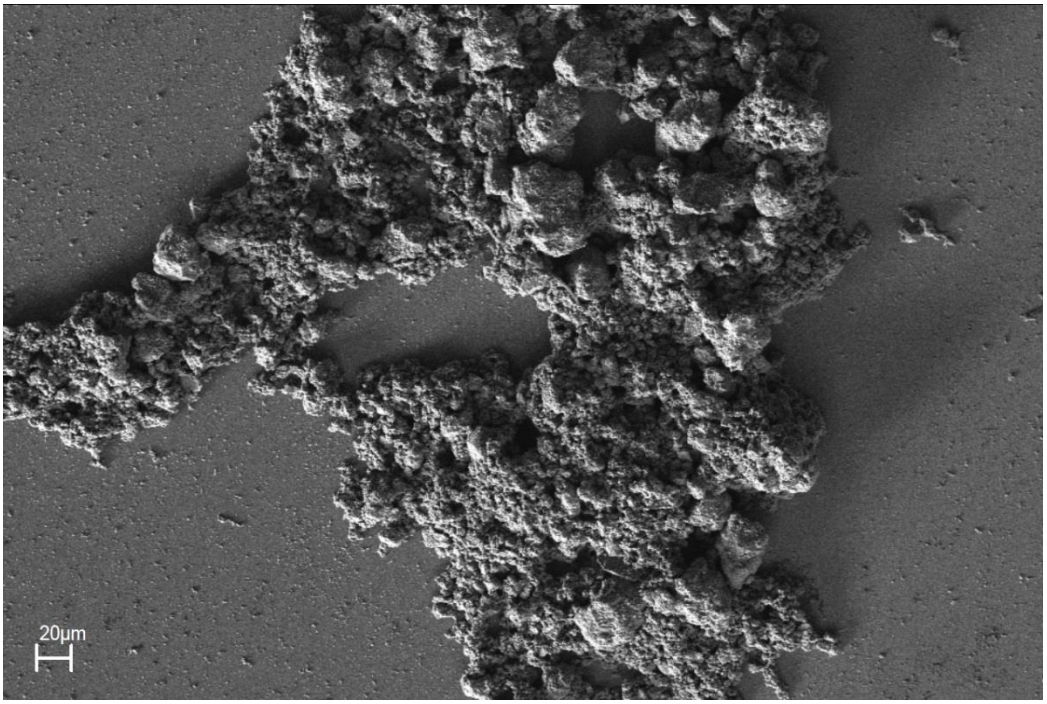

Figure 73 Clustered micro particles of the starting material

5.5.5. Determination of Sample Composition

The compositions of all samples were determined via wet chemical methods (ICP-MS, ICP-OES) and scanning electron microscope. In ICP-OES and ICP-MS each sample was weighed three times and digested. The results from both techniques showed a compositional deviation of 1-4 atomic percent zinc within the same sample. All measured zinc compositions differed significantly in their zinc concentration. All zinc concentrations were lower than the expected concentrations. A possible explanation for these deviations might be an insufficient digestion of the samples. The samples were digested in an automatic microwave digestion system by heating them in diluted nitric acid. It is possible that partially oxidised zinc on the surface of the $Pd_{1-x}Zn_x/Al_2O_3$ couldn´t be removed by this digestion method and therefore the zinc content was lower than expected.

The sample PaWi011 was measured 2 times in ICP-OES with a gap of 14 days between the measurements. The second measurement yielded higher zinc content than the nominal one. One possible explanation for this difference in composition could be that the sample was inhomogeneous, but it should be noted that having an inhomogeneous sample is very unlikely for a powder of nano particles. The powder was mixed during synthesis, again when it was filled into the gas impermeable glass vessels and again before taking a sample for the ICP-MS measurements. In case of the ICP-MS measurements the deviations in zinc composition within a single sample were smaller than the ones from ICP-OES but the overall composition was further from the expected composition than the composition determined by ICP-OES. In SEM-analysis, higher concentrations of the nano powder were applied on the silica carrier forcing the powder to cluster. The composition was measured using area-scans over these clusters. The SEM measurements yielded palladium-zinc compositions, which differed from one to five atomic percent when being compared to the expected compositions. In summary it must be stated that, that the analysis of particle composition is not of sufficient quality to allow for deeper discussion of the composition dependence of catalytic properties.

Table 12 Summary of sample composition determination with different methods

Samples	Expected Composition		Analyse ICP-MS		Analyse SEM		Analyse ICP OES	
	Pd	Zn	Pd	Zn	Pd	Zn	Pd	Zn
PaWi003	47.6	52.4					49	51
PaWi006	47.6	52.4					53.5	46.5
PaWi010	45	55	51	49			42.5	57.5
PaWi011	42	58	45	55	40.4	59.6	47.4	52.6
PaWi013	37	63	40	60	42.1	57.9	38.2	61.8
PaWi015	41	59	45.8	54.2	38.9	61.1	59.3	59.3

6. Conclusion

Taking all results into account it can be said that during the present work it was possible to optimise the synthesis method for $Pd_{1-x}Zn_x/Al_2O_3$ nanoparticles up to 63 at. % zinc. Particles with a higher zinc content might need a different synthesis approach.

Since no agglomeration could be observed, except sample PaWi003, after the reaction and the catalytic performance of the nano particles was comparable to the bulk material, it can be assumed that during the reaction, zinc was distributed evenly over the palladium powder. TEM and SEM results supported this assumption.

X-ray diffraction analysis was possible, despite the large background of the carrier particles, and it was possible to refine a crystal seize domain of 9 to 10 nano metres. This is in good agreement with the particle seize distribution of PdZn obtained by TEM measurements. After subtracting the background, it was impossible to determine accurate lattice parameters

Although all samples lay in the two-phase field of $\delta+\xi_1$, no evidence of the ξ_1-phase was found. The reason for the absence of the ξ_1-phase might be the kinetic inhibition of the crystallisation of this phase due to the nano crystalline character of the samples. If the particle size of PdZn-particles is in the range of a few nano metres, it is possible that the forming of a crystallisation seed or the growing of such seeds is kinetically hindered and therefore no ξ_1-phase can be observed in the X-ray diffraction pattern. Small seeds, which cannot grow, can be considered amorphous and therefore no reflections of this phase can be observed.

Composition analysis turned out to be quite difficult since all methods showed errors when measuring the same sample multiple times. The most reliable method appears to be ICP-OES, which showed the smallest deviations within the measurements.

The extrapolated activities of the preliminary CALPHAD assessment of the Pd-Zn system were tested in “reversed-pseudo-isopiestic” experiments. The results showed that the system still needed more adjustment at lower temperatures.

7. Summary

8.1. Summary (English)

Since the beginning of the 21st century, scientists are searching extensively for a renewable and sustainable energy source. Fossil fuels are limited resources and should therefore be replaced with unlimited energy sources like the wind or the sun. New model catalysts are needed to drive reactions for a "green" energy generation and storage. Working with catalysts requires a good understanding of the catalysts design, the catalysed reaction, the catalyst characterisation, possible deactivation processes and regeneration of the catalyst. In this work, the supported catalyst $Pd_{1-x}Zn_x/Al_2O_3$ was synthesized and studied. Catalysts with different compositions and synthesize temperatures were produced in order to find the best path for synthesizing a catalyst with high activity and high CO_2-selectivity. A phase diagram assessment of the Pd-Zn system was performed and the system modelled via CALPHAD-method, yielding activities, which were used to calculate a temperature gradient for synthesizing a catalyst with an exact composition. The measured catalysts in this work were synthesized using a temperature gradient, suitable for complete reaction with the zinc reservoir.

The catalysts were characterised by the means of XRD, ICP-MS, ICP-OES, SEM and TEM. Neither ICP-OES nor ICP-MS delivered high accuracy results in term of composition and could only provide the total composition of the PdZn particles. Detailed EELS-measurements will be necessary to determine the real composition of the single PdZn-particles. Additionally Raman spectroscopy should be used to determine if zinc oxide is present on the surface of the PdZn particles before and after the reaction.

TEM imaging was used to obtain the particle size distribution of the starting and the synthesized material. Activity and CO_2-selectivity of the synthesized catalyst was determined and compared to other model catalysts. A maximum CO_2-selectivity and activity was reached for the catalyst with the highest zinc content.

Further experiments with different carrier material such as BN should be conducted, which should give a better signal to noise ratio in the XRD-patterns. Detailed peak analysis can be used to determine the amount of present phases. Changing the carrier particle should not change the properties of the catalyst itself, if inert carriers are used.

8.2. Summary (Deutsch)

Seit dem Beginn des 21´ten Jahrhunderts sind Wissenschaftler auf der Suche nach erneuerbaren und nachhaltigen Energiequelle. Fossile Brennstoffe sind eine limitierte Ressource und sollten daher mit einer unlimitierten Energiequelle wie Wind und Sonne ersetzt werden. Neuartige Modell-Katalysatoren sind nötig für das katalysieren von Reaktionen für eine “grün“ Energieproduktion und Energielagerung. Ein gutes Verständnis des Herstellungsprozesses der Katalysatoren sowie eine genau Aufklärung der ablaufenden Reaktion, die Charakterisierung und mögliche Deaktivierung des Katalysators bei längerem Einsatz und die Regeneration des Katalysators sind unabdingbare Faktoren die alle untersucht werden müssen bevor ein Katalysator zum tatsächlichen Einsatz kommt. In dieser Arbeit wurde der geträgerte Katalysator $Pd_{1-x}Zn_x/Al_2O_3$ untersucht. Katalysatoren mit einer Zusammensetzung zwischen 50-62 at. % Zink und unterschiedlichen Synthesetemperaturen wurden synthetisiert um die Zusammensetzung und Synthesetemperatur zu finden, bei welchen der Katalysator die höchste Aktivität und CO_2-Selektivität hat. Ein Phasendiagramm Assessment des Pd-Zn Systems wurde durchgeführt und das resultierende Phasendiagramm mittels CALPHAD modelliert. Die daraus berechneten Aktivitäten wurden verwendet um einen Temperaturgradienten zu berechnen der es erlaubte einen Katalysator mit genauer Zusammensetzung zu synthetisieren. Allerdings wurden die in dieser Arbeit getesteten Katalysatoren mit einem an die Synthese Bedingungen angepassten Temperaturgradienten hergestellt.

Die Katalysatoren wurden mittels XRD, ICP-MS, ICP-OES, SEM und TEM charakterisiert. Weder ICP-OES noch ICP-MS lieferten genau Ergebnisse der Zusammensetzung. Mit diesen Methoden konnte nur die gesamt Zusammensetzung der Partikel ermittelt werden. Für eine Bestimmung der Zusammensetzung einzelner PdZn-Partikel wären EELS Messungen nötig. Ob ZnO auf der Oberfläche der PdZn-Partikel vor beziehungsweise nach der Reaktion vorhanden ist, könnte mit Ramanspektroskopie aufgeklärt werden.

TEM aufnahmen wurden angefertigt um die Verteilung der Partikelradien der PdZn-Partikel zu bestimmen. Eine Erhöhung des gemittelten Partikelradius um 1-2 nm nach der Reaktion mit Zink wurde beobachtet.

Die Aktivität und CO_2-selektivität der hergestellten Katalysatoren wurde gemessen und mit einem Referenzkatalysator verglichen. Ein Maximum der CO_2-selektivität und Aktivität wurde für den Katalysator mit dem höchsten Zinkgehalt gefunden.

Weitere PdZn-Katalysatoren mit unterschiedlichen Trägermaterialien wie BN sollten hergestellt und untersucht werden. Diese “neuen“ Trägermaterialien würden im Gegensatz zu dem quasi einkristallinen Al_2O_3 einen schwächeren Hintergrund im Röntgenbeugungsdiagram liefern und so eine genaue XRD-Analyse der vorhandenen intermetallischen Phasen ermöglichen. Die Verwendung eines anderen Trägermaterials sollte die katalytischen Eigenschaften des Katalysators nicht ändern da die Trägermaterialien inert sind.

8. References

[1] Tools for Climate Policy Planning Charles Heaps, Ph.D. Stockholm Environment Institute SEI-U.S. Center 11 Curtis Avenue, Somerville MA, 02144, USA

[2] Crane H., Kindermann E. Malhotra R., "*A Cubic Mile of Oil. Realities and options for averting the looming global energy crisis*", 2010, Oxford: Oxford University Press

[3] Lázló G., Erdőelyi F., "*Catalysis for Alternative Energy*", 2012, New York Springer publisher

[4] Fujishima A. Rao R. N., Tryk D.A., "Titanium dioxide photo catalysis" J. Photochem. Photobio. 1, 2000, 1-21.

[5] Meng N., Leung M. K. H., Leung D.Y.C., Sumathy K., "A review and recent developments in photocatalytic water-splitting using TiO_2 for hydrogen production" Renewable & Sustainable Energy Reviews 11, 2006, 401-425.

[6] Nowotny H., Bittner H., "*Die Kristallstruktur von PdZn*", *Monatsh. Chem. 81*, 1950, 679-680.

[7] Nowotny H., Bauer E., Stempfl A., "*Ein Beitrag zum System Palladium-Zink*", Monatsh. Chem. 82, 1951, 221-36

[8] Köster W., Zwicker U., "*Festschrift 100 Jahre W. C. Heräus*", 1951, 76 ,Hanau

[9] Kou S., Chang Y.A., "*Thermodynamics of ordered β_1-PdZn Alloys*" Acta Metall. 1975, 23, 1185–1190.

[10] Chiang T.; Ipser H.; Chang Y.A., "*Thermodynamic Properties of Palladium-Zinc Alloys*" Z. Metallkd. 1977, 68, 141–147.

[11] Neumann J. P., Ipser H., Chang Y. A., "*The Structural Stability of the B2 and $L1_0$ Phases in the System Pd-Zn*" *J. Less-Comm. Met. 57*, 1978, P29-P37.

[12] Alasafi K.M., Chattopadhyay T., Schubert K., "*Zur Mischung $PdZn_N$**"J. Less-Comm. Met. 59,1978,P41-P50

[13] Armbrüster M., Diploma Thesis, "*Synthesis, Structure and properties of the Hume-Rothery-Phases $Pd_{15}Zn_{54}$, Pt_2Zn_{11} and $(Pd_xPt_{1-x})_{2.4}Zn_{10.6}$*" Philipps University Marburg, 2001.

[14] Gourdon O., Izaola Z., Elcoro L., Petricek V., Miller G.J., "*$Zn_{1-x}Pd_x$ (x = 0.14-0.24). A missing link between intergrowth compounds and quasicrystal approximants*" Philos. Mag. 2006, 86,419–425.

[15] Gourdon O., Miller G.J., "*Intergrowth Compounds in the Zn-Rich Zn-Pd System: Toward 1D Quasicrystal Approximants*" Chem. Mater. 2006, 18, 1848–1856.

[16] Gourdon O.; Izaola Z.; Elcoro L.; Petricek V., Miller G.J., "*$Zn_{1-x}Pd_x$ (x =0.14–0.24): a missing link between intergrowth compounds and quasicrystal approximants*" Inorg. Chem. 2009, 48,9715–9722.

[17] Habrecht B., Thimmaiah S., Armbrüster M. Pietzonka C., Lee S., "*Structure and properties of γ-brass-type $PtZn_{11-\delta}$ (0.2<δ<0.3)*" Z. Anorg. Allg. Chem. 628, 2002, 2744-2749

[18] Vizdal J., Kroupa A., Popovic J., Zemenova A., "*The experimental and theoretical study of phase equilibria in the Pd-Zn(-Sn) system*" Adv. Eng. Mat. 8,2006,164-176

[19] Iwasa N.; Kudo S.; Takahashi H.; Masuda S., Takezawa N., "*High selective supported Pd catalysis for steam reforming of methanol*" Catal. Lett. 1993, 19, 211–216.

[20] Friedrich M. Ph.D. Thesis, "*Die intermetallischen Verbindungen ZnPd und ZnNi als Modellkatalysatoren in der Methanoldampfreformierung* " Technical University Dresden, 2013.

[21] Amore S., Delsante S., Parodi N., Borzone G., "Thermochemistry of Pd-In, Pd-Sn and Pd-Zn alloy systems" Acta Thermochem. 2009, 481, 1-6

[22] Friedrich M., Penner S., Heggen M., Armbrüster M., „High CO2 selectivity in Methanol Steam Reforming through ZnPd/ZnO Teamwork" Angew. Chem. Int Ed. 2013, 52, 4389-4392

[23] Thomas R., "*A Beginner´s Guide to ICP-MS*", 2001, Part 1-10, Spectroscopy

[24] Hou X., Jones B. T., "*Inductively Coupled Plasma/Optical Emission Spectrometry*", 2000, Encyclopaedia of Analytical Chemistry, 9468-9485, Chichester, John Wiley & Sons Ltd.

[25] Brunnee C., "*The Ideal Mass Analyser: Fact or Fiction?*" Int J. Mass Spectrom. Ion Proc.,1987, 125-237.

[26] Taylor, H.E., "*Inductively Coupled Plasma Mass Spectrometry*",2001 , Academic Press, San Diego.

[27] Robinson R. A., "*The Vapour Pressures of Solutions of Potassium Chloride and Sodium Chloride*" Trans. Of the Roy. Soc. New Zealand, 1945, 75, 203-217.

[28] http://www.le.ac.uk/chemistry/thermodynamics/pdfs/2500/Topic2370.pdf

[29] Seith, W., Krauss, W., "*Copper-Zinc system*" Z. Elektrochem., 1938, 44, 98-102.

[30] Hargreaves, R., "*Copper-Zinc system*" J. Inst. Met. , 1939, 64, 115.

[31] Hultgren R., Orr R. L., Anderson D. D., Kelley K. K., "*Selected Values of Thermodynamic Properties of Metals and Alloys and supplements"*, 1963, Wiley & Sons, New York

[32] H. Ipser, R. Krachler, K.L. Komarek, in: H. Brodowsky, H.-J. Schaller (Eds.), "*Thermochemistry of Alloys*", Springer, Kluwer Academic Publishers, Dordrecht, 1989, pp. 293–306.

[33] Keszei B., "*Chemical Thermodynamics*", 2012, Springer-Berlin

[34] Meschede D., "*Ghertsen Physic*", 2001, Springer-Lehrbuch

[35] Atkins,P., de Paula, J., "*Atkins' Physical Chemistry",* 2010, Oxford: Oxford University Press

[36] Kirschner H., "*Röntgenstrukturanalyse und Rietveldmethode*", 1994, Springer Fachmedien Wiesbaden

[37] Suryanarayana C., Norton M.G., "*X-ray Diffraction, a Practical Approach*", 1998, New York: Plenum Press.

[38] Woolfson M.M., "*An introduction to X-ray crystallography",* 1956, Cambridge: Cambridge University Press.Graef

[39] Graef M. McHenry M. E., "Structure of Materials- An Introduction to Crystallography, Diffraction, and Symmetry", 2007, Cambridge University Pree, New York

[40] Cullity B. D., "*Elements of X-ray Diffraction*", 1979, Addison-Weseley publishing Company Inc.

[41] Haugstad G., "*Atomic Force Microscopy- Understanding Basic Modes and Advanced Applications*", 2012, John Wiley & Sons Inc.

[42] Eaton P., West P., "*Atomic Force Microscopy*", 2010, Oxford University Press Inc, New York

[43] http://www4.nau.edu/microanalysis/microprobe-sem/instrumentation.html

[44] http://www.gla.ac.uk/schools/ges/research/researchfacilities/isaac/services/scanningelectronmicroscopy/

[45] Goldstein J. I., Newbury D. E., Echlin P., Joy D. C., Lyman C. E., Lifshin E., Sawyer L. Michael J. R., "*Scanning Electron Microscopy and X-ray Microanalysis*", 2003, Kluwer Academic/Plenum Publishers, New York

[46] Williams D. B., "*Transmission Electron Microscopy*", 1997, Plenum Publishing Corporation, New York

[47] http://universe-review.ca/R11-13-microscopes.htm

[48] http://www.microscopy.ethz.ch/TEMED.htm

[49] Fultz B, Howe J., "*Transmission Electron Microscopy and Diffractometry of Materials*", 2008, Springer Verlag Berlin Heidelberg

[50] http://www.cosmicastronomy.com/cosmic.htm

[51] http://www.specinst.com/What_Is_A_CCD.html

[52] Spencer P. J., "*A brief history of CALPHAD*", 2007, Elsevier Ltd.

[53] Saunders N., Miodownik A. P., "*CALPHAD-Calculation of Phase Diagrams*", 1998, Elsevier Ltd.

[54] Lukas H. L., Suzana F. G., Sundman B., "*Computional Thermodynamics - The Calphad Method*", 2007, Cambridge University Press, New York

[55] Reichmann T.L., Ipser H., "*Thermochemical investigations in the system cadmium–gadolinium relevant for pyro metallurgical fuel reprocessing metal*", J. Allosy & Comp., 2014, 617, 292-301

[56] Dennis Ivarsson MPI Dresden, August 2014, unpublished results; http://www.cpfs.mpg.de/1457949/employee_page?c=2074370&employee_id=29234

Curriculum Vitae et Studiorum

Name:	Patrick Wibner
D.O.B.:	Jul.13th. 1989. Vienna
Citizenship:	Austria
Home address:	Breitenfurterstraße 571a, 1230 Wien

Education and Career

Plan to start at 12/2014	PhD studies at the Department of Inorganic Chemistry / Materials Chemistry. Vienna
2014	Master thesis at the Department of Inorganic Chemistry / Materials Chemistry. Vienna: Innovative Synthesis of the model catalyst PdZn/Al_2O_3
2008-2014	Master studies at the University of Vienna: Chemistry
2007-2008	basic community service
2003-2007	Upper Gymnasium St. Ursula in Vienna. Austria